5 Large-scale Circulations in the Tropical Atmosphere

Up until now we have treated the tropical atmosphere mostly as a one-dimensional entity, with each vertical column in a state of radiative-convective equilibrium. But the tropical atmosphere is in constant motion, and the modulation of clouds and precipitation, as well as transport of heat, moisture and momentum by large-scale circulations is an important aspect of the physics of the tropical atmosphere. Here, after a brief overview, we tackle the dynamics of large-scale tropical circulations.

5.1 Overview of large-scale tropical circulations

Compared to the highly variable weather of middle and high latitudes, tropical weather is relatively steady and mostly benign, with the stunning exception of tropical cyclones. The steadiness of tropical winds in particular is owing, in part, to the absence of appreciable baroclinic instability, the primary driver of synoptic scale variability at higher latitudes. In many regions within the tropics, trade winds blow from a nearly constant direction at almost constant speed, as discovered by 15th-17th century mariners, who established trade routes mostly between Europe, the Americas, and the Far East. They quickly discovered how to use the trade winds to optimize sea voyages and so doing recorded observations of wind and weather, enabling the British scientist Edmond Halley (1656-1742), who had predicted the return of the comet later named after him, to construct the first know weather map (Halley, 1686), reproduced here as Figure 5.1. This is an example of a composite map that is based on observations made at widely disparate times, in contrast to synoptic maps made using nearly simultaneous observations that only became possible toward the end of the 19th century.

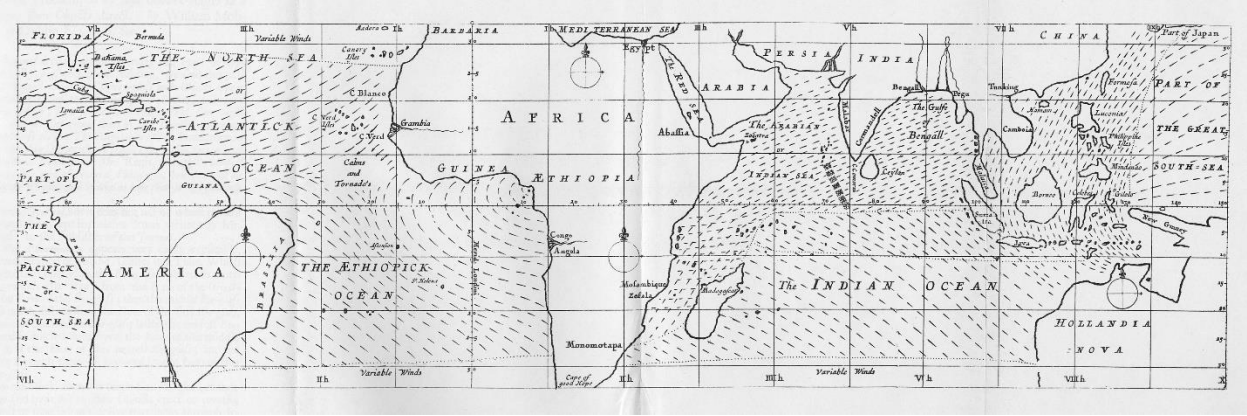

Figure 5.1: Edmond Halley's 1686 map of the trade winds, depicted as dashed lines.

Halley's paper contains detailed descriptions of tropical airflow, and his map clearly shows the northeasterly and southeasterly trades of the two hemispheres, converging along a near-equatorial discontinuity known today as the Intertropical Convergence Zone (ITZC). Comparison with monthly mean winds based on far more plentiful and recent data (Figure XXX) attests to the perspicacity of Halley's analysis.

Before reviewing modern analyses of tropical airflow and weather, we pause to consider the observational basis of such analyses.

5.1.1. Observations

Up through the early 20th century, observations of the atmosphere consisted mostly of measurements made at the surface by both professional and amateur observers, and by mariners, as recorded in ship's logs. Some inferences about conditions above the regional surface were made by recording weather on mountains and by observing the motion of clouds, supplemented by the odd manned balloon flight beginning in 1783. Late in the 19th century, observations using instrumented kites became routine in some regions, but these were limited by weather conditions and in any event could only extend a few kilometers above the surface. With the widespread advent of aviation in the 1930s, temperature and pressure could be measured at altitude, though flight level winds could only be inferred from the drift of aircraft between navigational fixes. Like kites, these observations were limited in altitude and by weather. Yet the discovery that winds on synoptic and larger scales were nearly geostrophic, particularly above the boundary layer, enabled early 20th century meteorologists to deduce winds aloft from temperature and pressure measurements.

Beginning around 1909, scientists began to experiment with balloon-borne measurements using instruments that had to be retrieved from the balloons after their descent. By the late 1920s, primitive radios were used to transmit weather data to surface receivers, obviating the need to recover the balloons, and by the early 1930s the "radiosonde" observations were reaching the lower stratosphere. In 1937 the U.S. Weather Bureau (later renamed the National Weather Service) established a network of radiosonde stations launching balloons at regular intervals, and this was expanded in the 1940s owing to the war-related demands for better upper-air observations. The 1940s also saw the development of radio-direction finding, replacing the manual tracking of sondes using theodolites, resulting in the radio-wind sonde, or "rawinsonde". Sonde networks were established throughout the world, and radio-direction finding was replaced by more advanced techniques, culminating in the GPS sondes in use today. Figure 5.2 shows the locations of sonde stations as of 2020.

Sondes provide measurements of wind, temperature, pressure, and relative humidity at very high vertical resolution, but they are snapshots and may not be very representative of regional conditions, particularly if they are sampling strong local features such as cumulus clouds or mountain waves. Sampling over oceanic regions and even some land regions, such as central Africa, is sparse. Yet, sondes themselves are relatively inexpensive, and automation has reduced the need for human labor, so they remain an economical means of sampling the atmosphere.

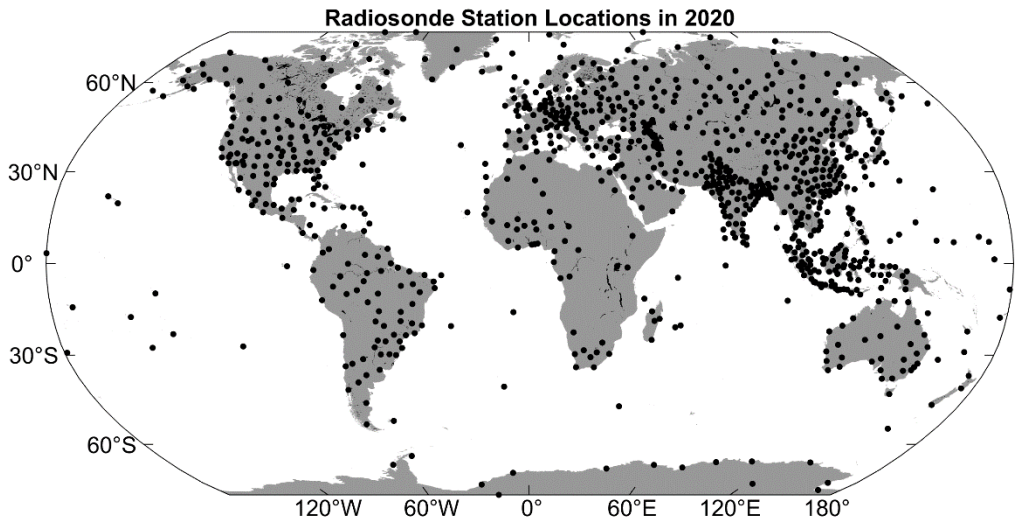

Figure 5.2: Locations of sonde stations in 2020. Sondes are generally launched twice per day, at 00 and 12 GMT.

Beginning in the 1960s, earth-orbiting satellites have been used as platforms for instruments designed to measure the atmosphere and oceans. Up though the late 1970s, almost all of these measurements were in the form of passive visible and infrared radiometric measurements – passive in the sense that the instruments were not transmitting signals but measuring reflected, scattered, and emitted radiation at various wavelengths. These passive measurements remain the backbone of space-based observations, allowing researcher and forecasters to detect and track features revealed by the visible, during the day, and infrared imagery at all hours. Because different greenhouse gases, clouds, and the surface itself emit and absorb radiation differently according to the wavelength of the radiation and temperature, multi-spectral infrared measurements contain information about the vertical structure of temperature, clouds, and greenhouse gases like water vapor, and information about surface temperature.

In 1978, NASA launched Seasat, which carried an active microwave scatterometer. This instrument sends pulses of radiation of wavelength comparable to wavelength of capillary waves on water surfaces. By measuring the amplitude of the backscattered radiation, an estimate of capillary wave amplitude can be made, and this is directly proportional to wind stress in the water surface. By comparing amplitudes of the same foot print seen from two or more angles during the spacecraft's orbit, one can estimate the orientation of the capillary waves and thus the direction of the surface stress vector. Unfortunately, radiation at this wavelength is heavily absorbed by precipitation, so surface stress cannot be accurately estimated in regions of heavy rain.

The era of sea surface altimetry commenced in 1992 with the launch of TOPEX/Poseidon, a joint U.S.-France venture to monitor sea level and seasonal variations in oceanic circulation. Radar altimeters measure the time between transmission of a pulse of radiation and the reception of that pulse after reflection from the surface. State-of-the-art altimeters measure the surface with an accuracy of 4-5 cm. Knowledge of the slope of the sea surface relative to the geoid allows one to calculate geostrophic velocities.

Beginning in 1995, a suite of low-earth-orbiting satellites has been deployed to measure transmissions from GPS satellites as they rise and set relative to the low-orbit platforms. In

essence, the low-orbit satellites measure the bending of the GPS signal transmitted through the atmosphere, which depends on the refractive index, a function of temperature, pressure, and water vapor, down to quite close to the surface. This “radio occultation” technique yields vertical profiles of temperature and water vapor, and the 24 GPS satellites together with the low-earth-orbiting satellites yield many soundings each day. Figure 5.3 shows the location of radio occultation soundings over a single 24-hour period.

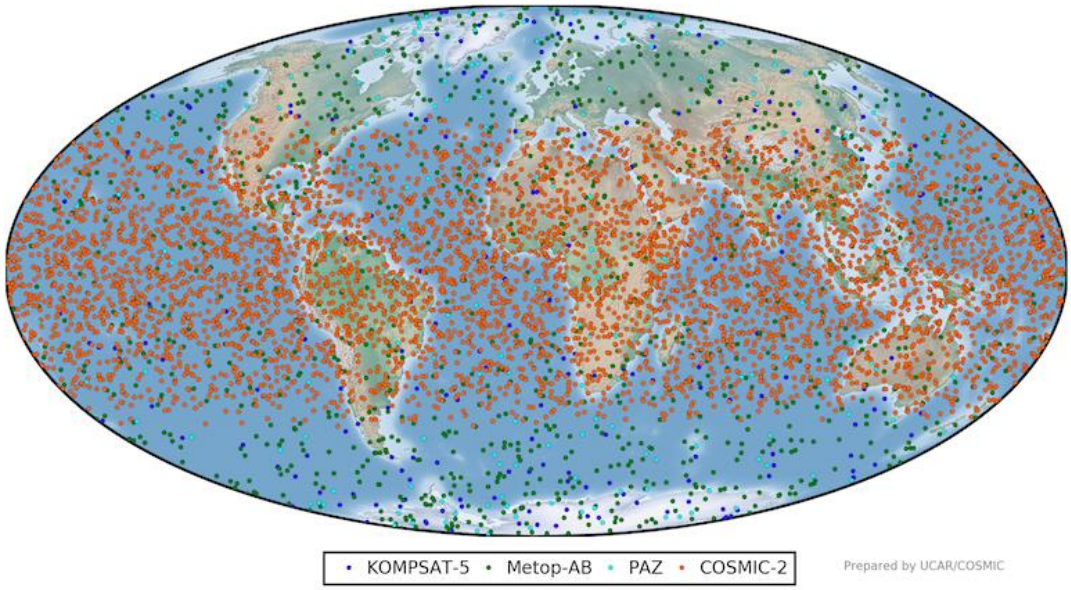

Figure 5.3: Location of radio occultation soundings over a 24-hour period. Note the especially dense coverage in the tropics.

From 1997 to 2015, NASA operated the Tropical Rainfall Measurement Mission (TRMM) research satellite to provide active radar measurements from space. The scanning radar transmitted pulsed microwave radiation downward and measured radiation backscattered from precipitation in the atmosphere. Some examples of TRMM measurements are provided in the next subsection.

Many commercial airlines as well as package delivery aircraft are equipped with sensors that measure temperature and humidity, and winds are deduced from the airspeed and GPS positions. This data is now routinely collected in real time and provides vertical profiles at airports and flight-level conditions around the world, focused in air traffic corridors.

On the ocean side, measurements of surface temperature and salinity have been made from ships for over a century, and in recent decades these have been augmented by space-borne passive radiometric measurements. Until fairly recently, properties of the subsurface ocean could only be deduced from expensive and laborious measurements made from ships. These have now been augmented by direct measurements using robotic sounders known as ARGO floats. The floats are mini-submarines, that descend from the surface to depths of 1-2 km, (in recent years a few can go as deep as 6 km), and then ascend back to the surface, making measurements of temperature and salinity along the way. These are then transmitted to satellites. The floats can be programmed to linger at a prescribed depth so that the ocean current velocity at that depth can be detected via the float’s net drift. Figure 5.4 shows the positions of ARGO floats on a particular day in January, 2021.

The ARGO floats, with the previously discussed sea surface altimetry, temperature, and salinity measured from satellite, augmenting traditional measurements from ships, constitute the basis of routine ocean measurement today.

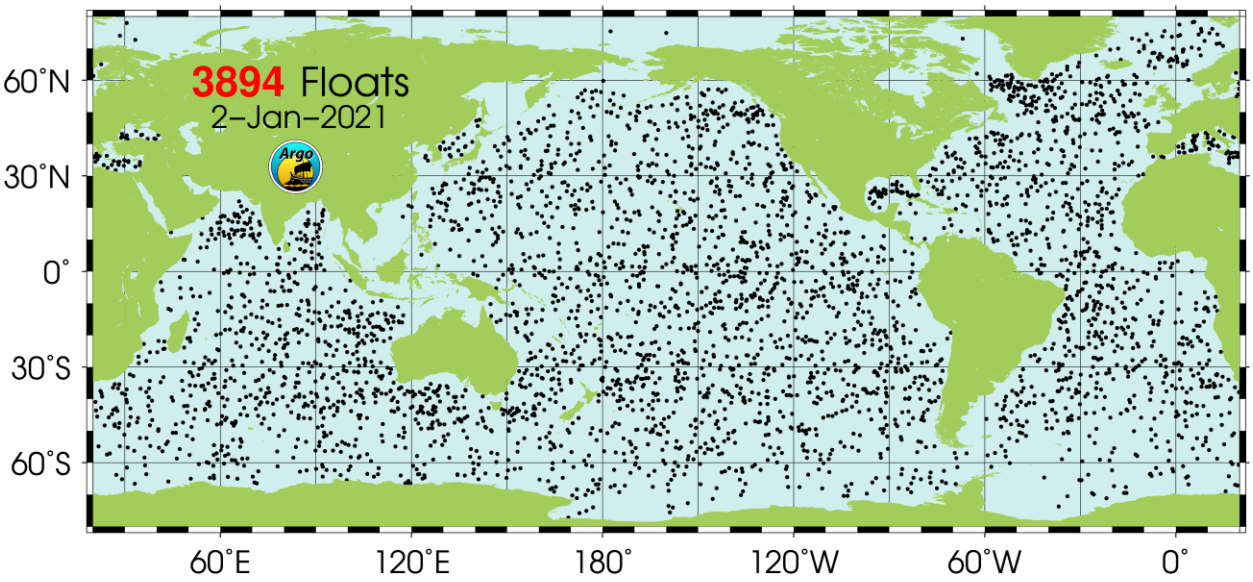

Figure 5.4: Locations of ARGO floats on Janaury 2nd, 2021.

5.1.2 Analysis techniques

The aforementioned measurements form the basis of contemporary state estimates of the atmosphere and oceans. Optimal state estimation is a large and challenging enterprise, given the great disparity in measurement type and the spatial and temporal heterogeneity of the data. These state estimates are used as the initial conditions for numerical weather forecasts and also as the basis of long-term climatologies.

The topic of optimal state estimation is rich, complex, and mathematically challenging and cannot be done justice in a few paragraphs. Broadly, the approach taken today is fundamentally Bayesian, with a prior state estimate given by a previous numerical forecast, updated using various kind of filters that account for measurement and sampling errors and errors in the model used to provide the prior state estimate. Different numerical weather prediction centers us different types of filters, and what constitutes an optimal filter (defined as that which leads to the best subsequent numerical predictions) is a subject of ongoing research. An important advantage of contemporary state estimation is its ability to deal with highly disparate types of data. For example, satellite-based radiances are directly assimilated into numerical weather prediction models, rather than first being inverted to estimate vertical temperature profiles. When new data sources arise, it is fairly straightforward to incorporate these into these data assimilation schemes. Much of the improvement in the quality of weather forecasts in recent decades can be attributed to the advent of high performance data assimilation schemes.

These data assimilation schemes can also be used to create optimal estimates of past states of the atmosphere and ocean; this enterprise is known as “reanalysis”. A good numerical weather

prediction model is used to assimilate past observations over time to create a sequence of atmospheric states, or “reanalyses”. More recently, the same strategy has been used to provide optimal state estimates of the ocean.

Most of these reanalyses, providing many variables on regular spherical grids, are freely and publicly available and are widely used in climate, atmospheric, and oceanic research. Their ready availability and ease of use has tempted many to regard them as representing the true state of the atmosphere and ocean, but it is important to recognize their limitations. For analyzing instantaneous states, the main limitation is the diversity of observation types and the often enormous spatial and temporal inhomogeneity of the observations. At every point in space and time, the reanalyses are influenced by model error as well as measurement and sampling errors. In locations and at times when measurements are sparse, the re-analyzed state may more represent the model physics than the real world.

Another, perhaps more serious problem arises when one tries to use reanalysis data to detect temporal trends in atmospheric or oceanic properties. The evolution over time of the sources of assimilated data introduce spurious trends in reanalyses. For example, it is well known that there are spurious jumps in reanalysis variables across the late 1970s owing to the introduction of satellite-based observations. One way around this particular problem is to assimilate only surface pressure and temperature observations, that have not evolved quite so radically, at least over the 20th and 21st centuries; this is the strategy used by NOAA’s 20th century reanalysis project (Compo et al., 2008). Such reanalyses have fewer problems with spurious trends but the instantaneous states are not well represented as in conventional reanalyses owing to the omission of upper-air data.

In what follows, we make heavy use of both direct satellite measurements and reanalysis data, and in interpreting these climatologies one should be aware of the limitations of both the measurements and the analysis techniques.

5.1.3 Large-scale climatology of the tropics

We begin where Edmond Halley left off, with a description of the large-scale, monthly mean surface airflow in the tropics. Figure 5.5 shows the monthly mean surface winds in January, April, July and October, compiled from reanalysis data on a 2.5-degree grid, from 1981 to 2010. Comparison with Halley’s map (Figure 5.1) attests to the quality of his 1686 analysis. Across the Pacific and Atlantic oceans, winds in the tropics are dominated by northeasterlies in the northern hemisphere and southeasterlies in the southern hemisphere. The lines of discontinuity in Halley’s analysis do not show up clearly in the monthly mean winds; we might speculate that Halley’s inference was based on the logs of individual ships which often did encounter abrupt wind shifts near that ITZC. But the position of such shifts would naturally be smoothed out in monthly mean data.

The tropical South Indian ocean is dominated by southeasterly trade winds at all time of the year, but the North Indian Ocean winds are strongly seasonal, with northeasterlies in the winter and strong southwesterlies in summer. This is a signature of the Asian monsoon, about which more in section 5.4. Elsewhere once can notice a gentle shifting of the trade winds towards the summer hemisphere and a strengthening of the winds in the winter hemisphere.

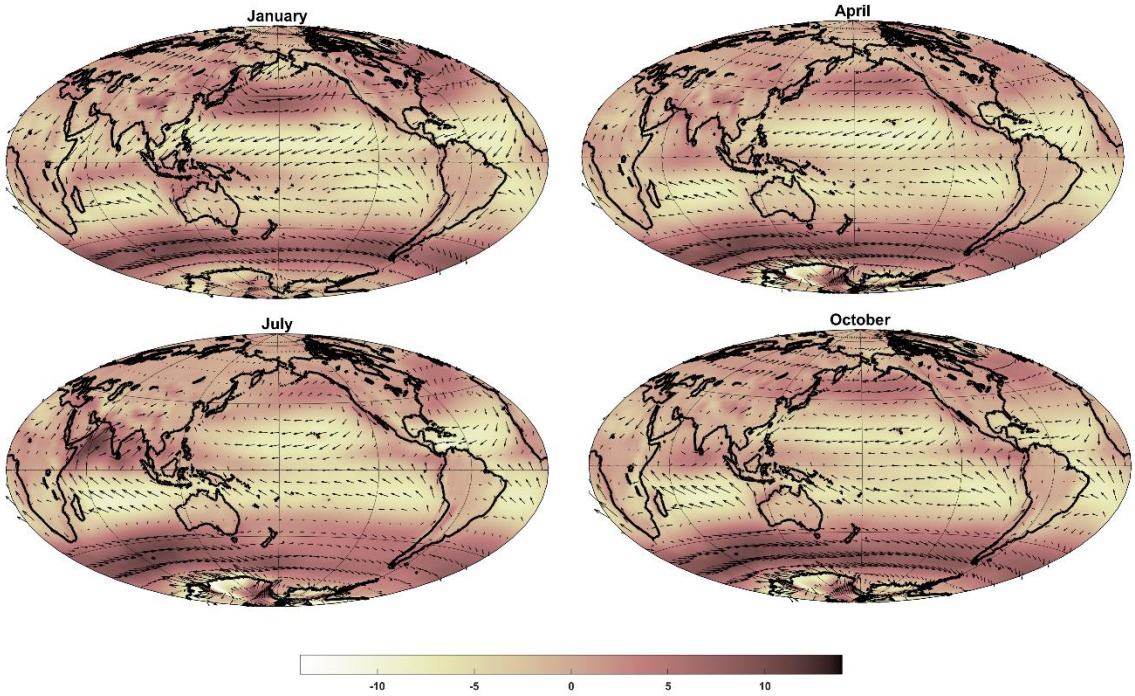

Figure 5.5: Monthly mean surface winds from NCAR/NCEP reanalyses averaged over the period 1979-2019. The shading indicates the wind speed (m/s) according to the scale at bottom, and the arrow directions and lengths correspond to the wind direction and speed, respectively.

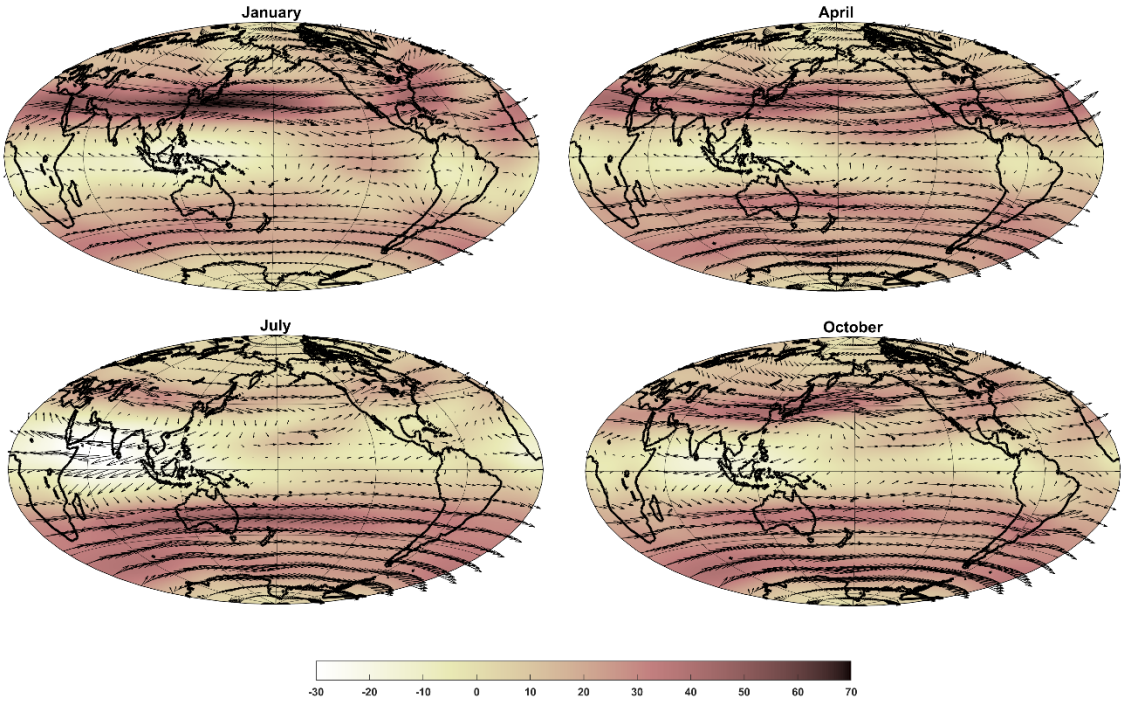

Figure 5.6: Monthly mean near-tropopause (150 hPa) winds from NCAR/NCEP reanalyses averaged over the period 1979-2019. The shading indicates the wind speed (m/s) according to the scale at bottom, and the arrow directions and lengths correspond to the wind direction and speed, respectively. Note that the wind scale differs from that in Figure 5.5.

Figure 5.6 shows monthly mean wind direction and speed at the 150 hPa level, which is near the pressure level of the tropopause in the tropics. The tropical region is bounded by strong westerly jets that extend from the subtropics well into middle latitudes. The jets are stronger and closer to the equator in winter. In the deep tropics, near-tropopause winds are generally light and from the east, but with some notable exceptions. In January, there is an extensive region of westerly wind in the eastern tropical Pacific, and this is bridged to the norther hemisphere subtropical and mid-latitude westerlies. This is important because it provides a conduit for nearly stationary Rossby waves to propagate into the tropics from higher latitudes in the northern hemisphere. This patch of westerlies retreats into the central subtropical North Pacific in July and migrates back toward the eastern equatorial Pacific during the boreal autumn.

Monthly mean virtual temperature at 600 hPa is displayed in Figure 5.7. Consistent with the weak temperature approximation (WTG), spatial as well as seasonal variations of virtual temperature are very small – generally less than 1 K – equatorward of 15 degrees. The most striking feature of these maps is the large positive virtual temperature anomaly over the Tibetan plateau in July.

Sea surface temperature varies spatially somewhat more than does 600 hPa virtual temperature equatorward of 15 degrees. The warmest water is in the Indo-Pacific “warm pool”, whose latitude oscillates gently with the seasons. By contrast, the eastern Atlantic and South Pacific are quite cool even though the 600 hPa virtual temperature is not appreciably cooler than at other longitudes. As we shall explore later in this chapter, the anomalously cool water in these regions is owing to ocean upwelling and lateral heat transport, augmented by reduced absorbed solar radiation owing to stratocumulus clouds in these regions.

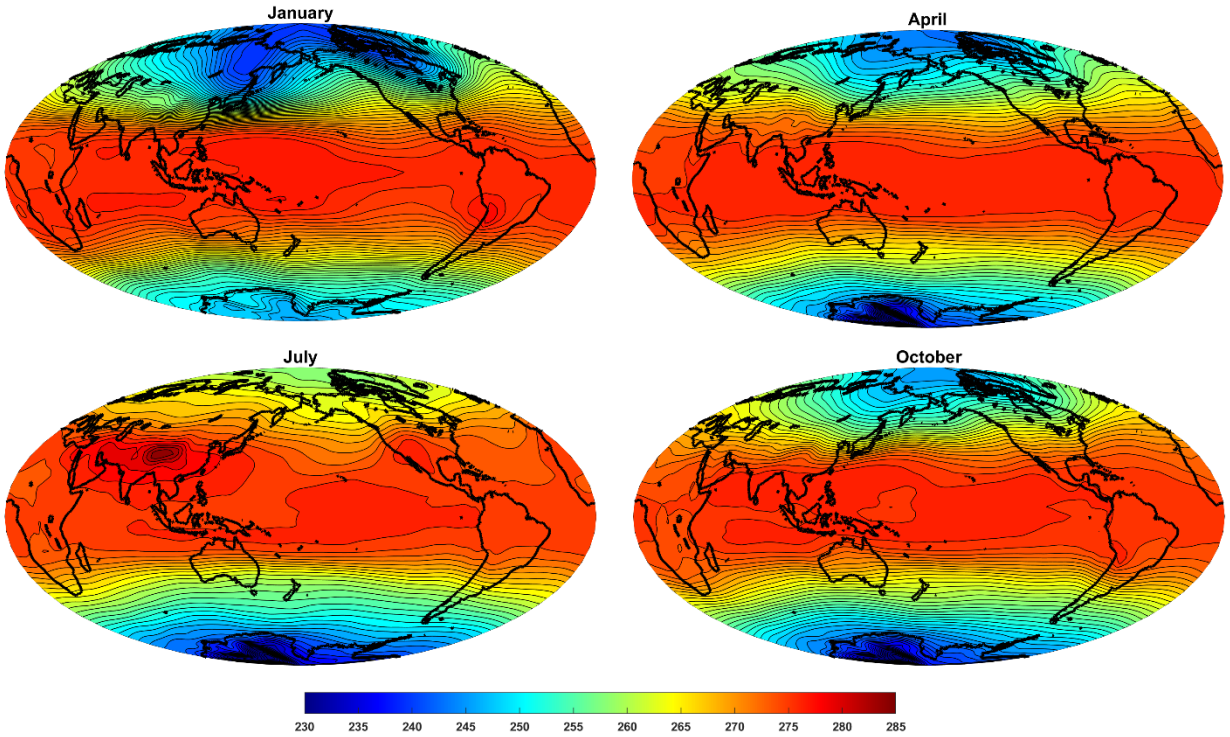

Figure 5.7: Monthly mean virtual temperature (K) at 600 hPa in January, April, July and October, constructed from NCAR/NCEP reanalysis data over the period 1949-2019. Contour interval is 1.25 K.

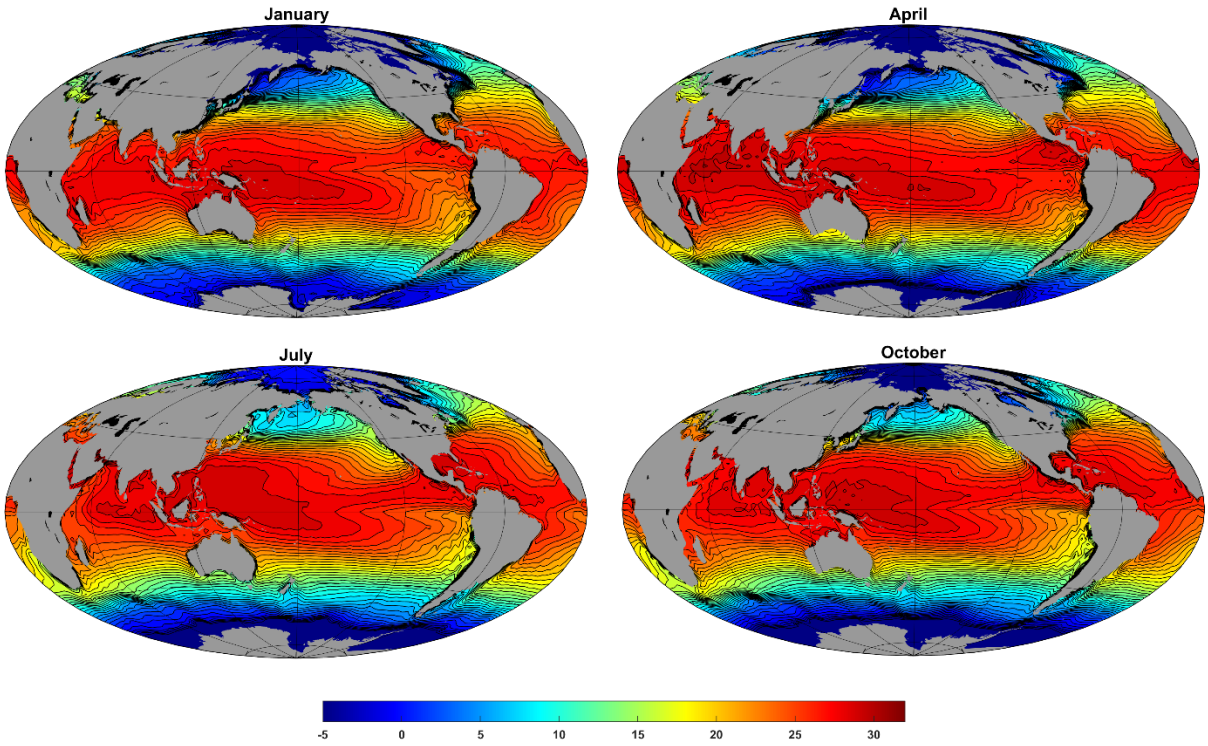

Figure 5.8: Monthly mean sea surface temperature (C) in January, April, July and October, constructed from NCAR/NCEP reanalysis data over the period 1949-2019. Contour interval is 0.84 C.

The distribution of monthly mean precipitation in January, April, July and October is shown in Figure 5.9, constructed mostly from satellite-derived precipitation measurements, particularly those made using the active radar onboard the TRMM satellite.

Focusing on the tropics, one of the first things one notices is the strong concentration of precipitation into an ITCZ that spans the Pacific and Atlantic oceans but becomes somewhat amorphous in the far western Pacific. This ITCZ nicely corresponds to where the trade winds converge (Figure 5.5). Another interesting feature is a wide band of enhanced precipitation extending southeastward from the far western equatorial Pacific. This is known as the “South Pacific Convergence Zone (SPCZ)”. The Asian monsoon is evident as a strong maximum of precipitation over the Western Ghat mountains of India, northern India, and the Bay of Bengal, coupled with a near absence of precipitation in those same regions in January. Less prominent monsoonal rainfall is also evident over extreme northern Australia and the Pacific coast of Mexico.

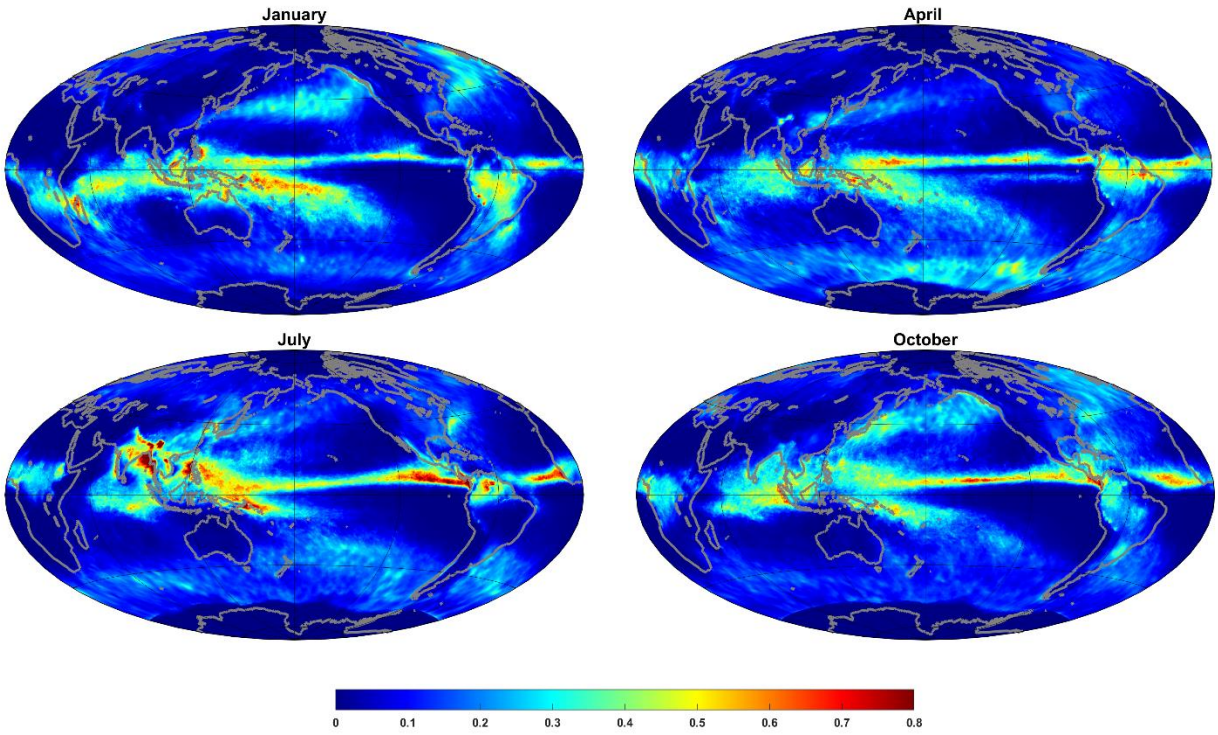

Figure 5.9: Monthly mean rainfall rate (mm/hr) in January, April, July, and October, from NASA's IMERG data based on a constellation of satellites augmented where possible with rain gauge data, 2002-2019. Measurements from the Tropical Rainfall Measurement Mission (TRMM) active precipitation radar are an important component of these synthesized data.

There are also prominent regions of heavy precipitation over equatorial Africa and South America that oscillate northward and southward with the seasons.

In general, the precipitation tends to follow the regions of highest sea surface temperature, but the relationship between SST and precipitation is far from one-to-one.

Also conspicuous are the large 'deserts' (regions of little or no precipitation) over the eastern subtropical oceans. The eastern Atlantic deserts extend well eastward over land in the northern hemisphere at all times of the year, and inland over southern Africa in southern hemisphere winter. The "maritime continent" of Indonesia is also a significant locus of heavy precipitation.

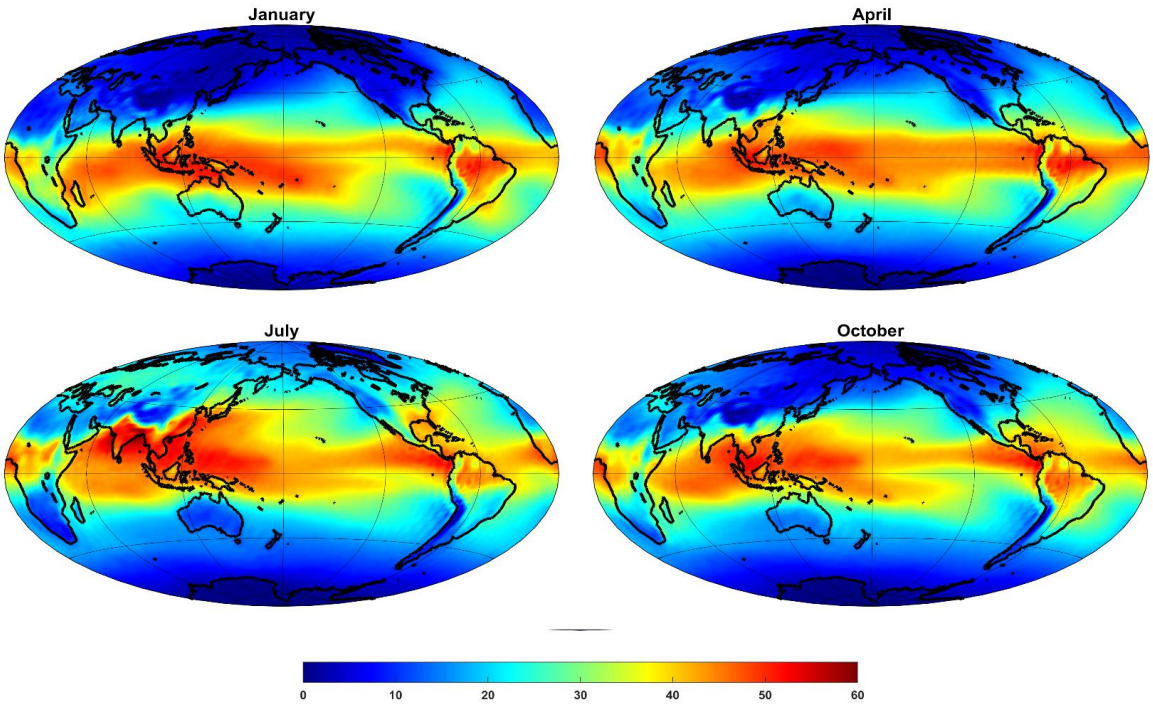

Figure 5.10: Mass-weighted, vertically integrated atmospheric water vapor content (kg m^{-2}) in January, April, July, and October, from NCAR/NCEP reanalyses, 1979-2019.

Most of the water vapor on our planet is within the tropics, as illustrated in Figure 5.10 which shows global monthly mean mass-weighted, vertically integrated water vapor averaged over three-month periods. Note that there is a reasonable correspondence between column water vapor and precipitation, but in many places rainfall is far more concentrated than is the water vapor. As noted in Chapter 3, section 3.3.3c, there is a strong, observed statistical relationship between column water vapor and precipitation in the tropics (Figure 3.32) but the reader is reminded that one should be cautious about inferring causality from this statistical relationship; indeed, one can reproduce the general character of this curve by varying the surface enthalpy flux in a simple single-column model with boundary layer quasi-equilibrium and the weak temperature gradient approximation. In this case, the 'causal' agent is the varying surface fluxes, with both column water vapor and precipitation varying in response. The nonlinearity of the precipitation-column water vapor response helps explain why the precipitation is more focused than column water vapor in the climatology displayed in Figure 5.9.

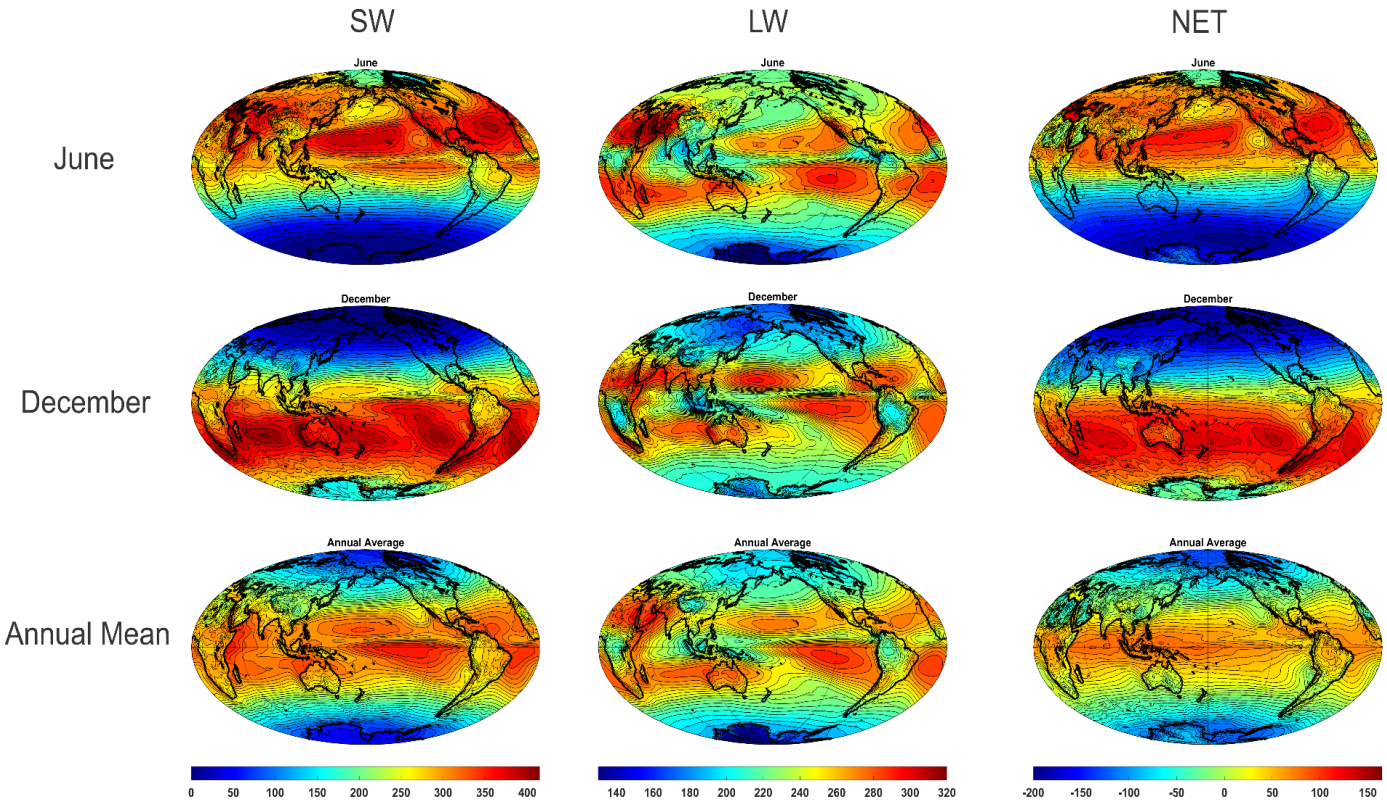

Figure 5.11: Top-of the-atmosphere (TOA) radiative fluxes (W m^{-2}): Net downward shortwave flux (left), net upward longwave flux (middle), and total net flux (right), for June (top), December (middle) and annual average (bottom). Data is from NASA's Clouds and the Earth's Radiant Energy System (CERES) program for the period 2001-2019.

Earth-orbiting and geostationary satellites have been measuring total outgoing longwave radiation, incoming solar radiation, and reflected solar radiation since the early 1980s, and much can be learned by examining these radiative fluxes. Figure 5.11 represented a compilation of total incoming solar radiation (incoming minus reflected shortwave) outgoing longwave radiation, and net incoming radiation (total incoming solar minus outgoing longwave). The total incoming solar radiation (left panels) reflects not just the latitudinal and seasonal distribution of top-of-the-atmosphere insolation, but albedo, which is mostly owing to clouds, and at high latitudes, snow, land ice, and sea ice. Once can clearly see, in the annual mean, the tropical maximum diminished by clouds in the ITCZ, over the tropical continents, and over cold ocean water in the subtropics just off the west coasts of continents.

The outgoing longwave radiation has peaks in broad subtropical belts where there are few high clouds and relatively small column water vapor. (These subtropical maxima are sometimes referred to as the planet's "radiator fins".) In the annual mean, there is some spatial correlation between outgoing and net incoming radiation in the tropics: where there are few clouds, there is little reflection of shortwave and longwave photos originate at higher temperatures lower in the atmosphere. But note that the seasonal variation of net incoming shortwave radiation greatly exceeds that of longwave radiation, accounting for most of the seasonal swing in net radiation. A strong north-south imbalance of net radiation occurs during the extreme seasons that is

compensated partially by inter-hemispheric transport and partially by energy storage in the atmosphere, cryosphere and oceans as they heat up and cool off.

One curiosity of the distribution of annual mean net incoming radiation (lower right panel of Figure 5.11) is that is somewhat more zonally symmetric than annual means of either the net shortwave or longwave radiative fluxes. This implies a degree of compensation between departures from the zonal means of shortwave and longwave fluxes. Indeed, detailed comparisons of clear sky and cloudy radiative fluxes shows that the large attendant anomalies of shortwave and longwave TOA radiation almost perfectly cancel. On the other hand, there clearly exists a net surplus of incoming radiation in the zonal, annual mean and this must be compensated by material fluxes of enthalpy way from the tropics by the atmosphere and/or oceans. The distribution of annual mean net radiative fluxes suggests that the annual mean enthalpy flux by the combined ocean-atmosphere system will also be approximately zonally symmetric.

Viewing monthly mean maps of various quantities, as we have been doing, can have the undesirable side effect of lulling one into thinking of the tropical atmosphere and having small variability on time scales of weeks or less. While day-to-day variability of winds, temperature, and pressures are indeed small compared to variability at higher latitudes, figures 5.12 and 5.13 remind us of this large sub-monthly variability in clouds and precipitation. While one can still identify long-term mean features such as the ITCZ, there is clearly much more going on. We will explore the nature of shorter-term variability in Chapter 6.

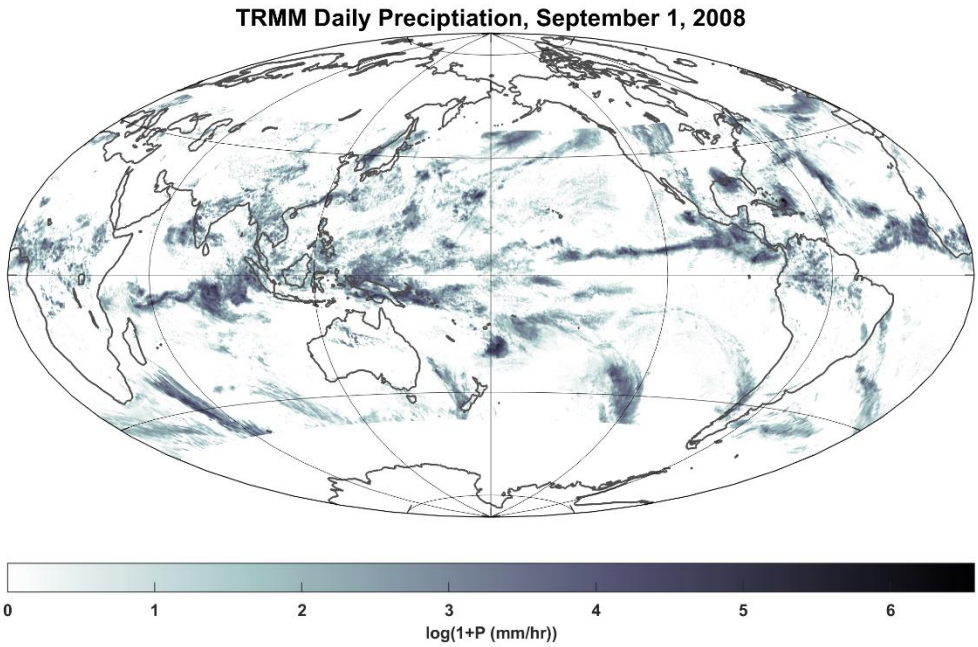

Figure 5.12: Distribution of daily precipitation measured by the NAS TRMM active precipitation radar on September 1, 2008, expressed as the natural logarithm of 1 + the precipitation rate in mm hr^{-1}.

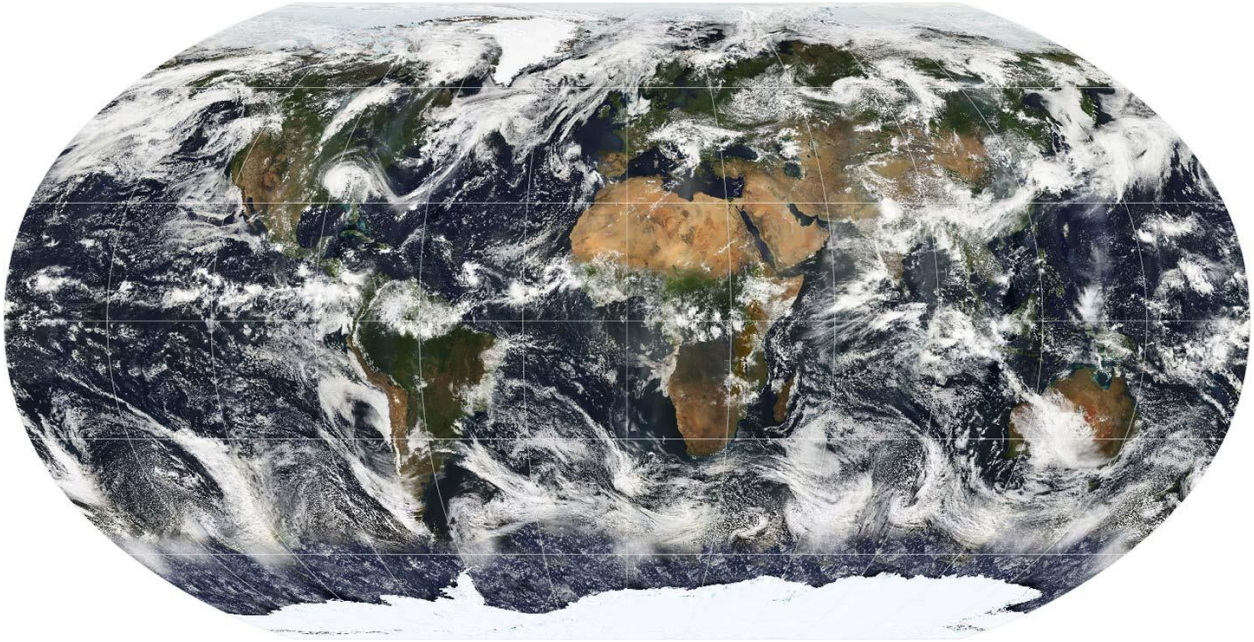

Figure 5.13: Global cloud cover on July 11th 2005 based largely on observations by the MODIS sensor on the NASA Terra satellite

5.1.4: Zonal mean, time-mean climatology

The near zonal symmetry of the annual mean net incoming radiation (Figure 5.11, lower right panel) implies that heat is exported by the atmosphere and oceans nearly symmetrically, though there is no requirement that transport in each medium is symmetric. Measurements show that the oceans and atmosphere export roughly equal amount of heat to higher latitudes, but here we focus on the zonally averaged atmospheric circulation. Figure 5.14 shows the mass streamfunction corresponding to the zonally averaged meridional flow. The streamfunction is defined so that the hydrostatic form of the mass continuity equation in pressure co-ordinates is satisfied:

$$\frac{1}{a\cos(\theta)}\frac{\partial}{\partial\theta}\left(v\cos(\theta)\right)+\frac{\partial\omega}{\partial p}=0, \tag{5.1}$$

where a is the radius of the earth, θ is latitude, p is pressure, v is the meridional wind component, and ω is the pressure velocity, dp/dt. We define a mass streamfunction, ψ, such that

$$\begin{aligned}\frac{\partial\psi}{\partial p}&=v\cos(\theta),\\ \frac{1}{a}\frac{\partial\psi}{\partial\theta}&=-\omega\cos(\theta).\end{aligned} \tag{5.2}$$

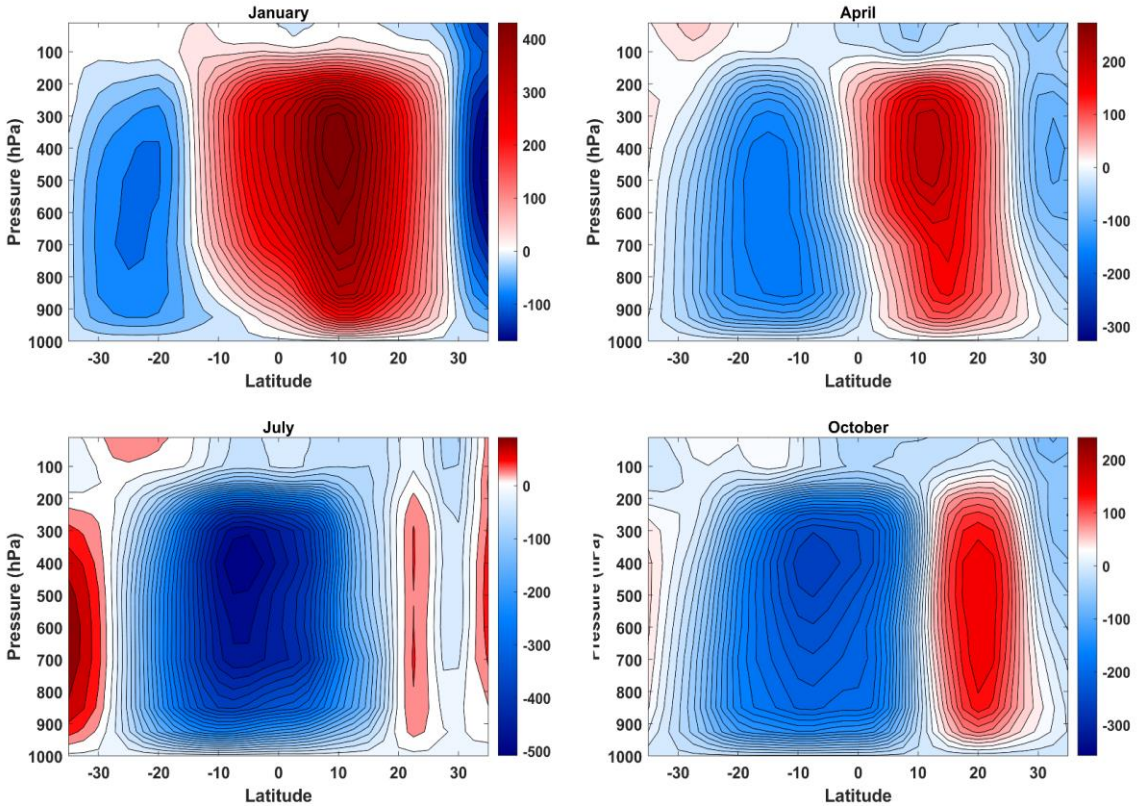

Figure 5.14: Zonal mean, monthly mean mass streamfunction (0.1 Kg m^{-1} s^{-1}) for January, April, July and October, calculated from NCAR/NCEP reanalysis data over the period 1979-2019. Circulation is clockwise around positive centers and counterclockwise around negative center. The contour interval in each plot is the same but the color scale differs for each plot, through it spans the same total interval.

Substitution of (5.2) into (5.1) verifies that mass continuity is satisfied. The mass flux per unit zonal length is the same between any two streamlines. Here we calculate the streamfunction by integrating in pressure the top part of 5.2 using meridional winds from NCAR/NCEP reanalyses, taking ψ to be zeros at 1000 hPa.

In January there is strong descent in the northern hemisphere between about 10 degrees and 40 degrees north latitude, and ascent between about 25 degrees south and 10 degrees north, associated with a strong clockwise circulation cell centered around 10 degrees north and 400 hPa. A far weaker counterclockwise cell is centered around 25 degrees south. In July, the strongest overturning cell is in the southern hemisphere, with ascent from about 5 degrees south to 22 degrees north, strong descent in the southern hemisphere 5 degrees south to about 35 degrees south, and a vanishingly weak clockwise cell in the northern hemisphere.

In the near-equinoctial months of April and October, the circulation cells are much weaker (note the different color scales) and somewhat more symmetric about the equator, although in October the ascent distinctly favors the northern hemisphere.

These overturning circulations are referred to as the “Hadley Circulation”, named after the British meteorologist George Hadley (1685-1768) who was the first to give a qualitatively correct account of their origin (Hadley, 1735). The individual overturning cells are likewise referred to as “Hadley cells”. As can be seen by comparing Figure 5.14 with the mid-tropospheric

distribution of virtual temperature (Figure 5.7), these cells are thermally direct, with less dense air rising and denser air sinking.

The generally poleward net transport of heat by the Hadley Circulation can be visualized by superimposing the mass streamfunction on the distribution of moist entropy (given by (2.69), omitting the last term and taking $T_0 = 250\ K$ and $p_0 = 1000\ hPa$), also calculated from reanalysis data. This superposition is shown in Figure 5.15.

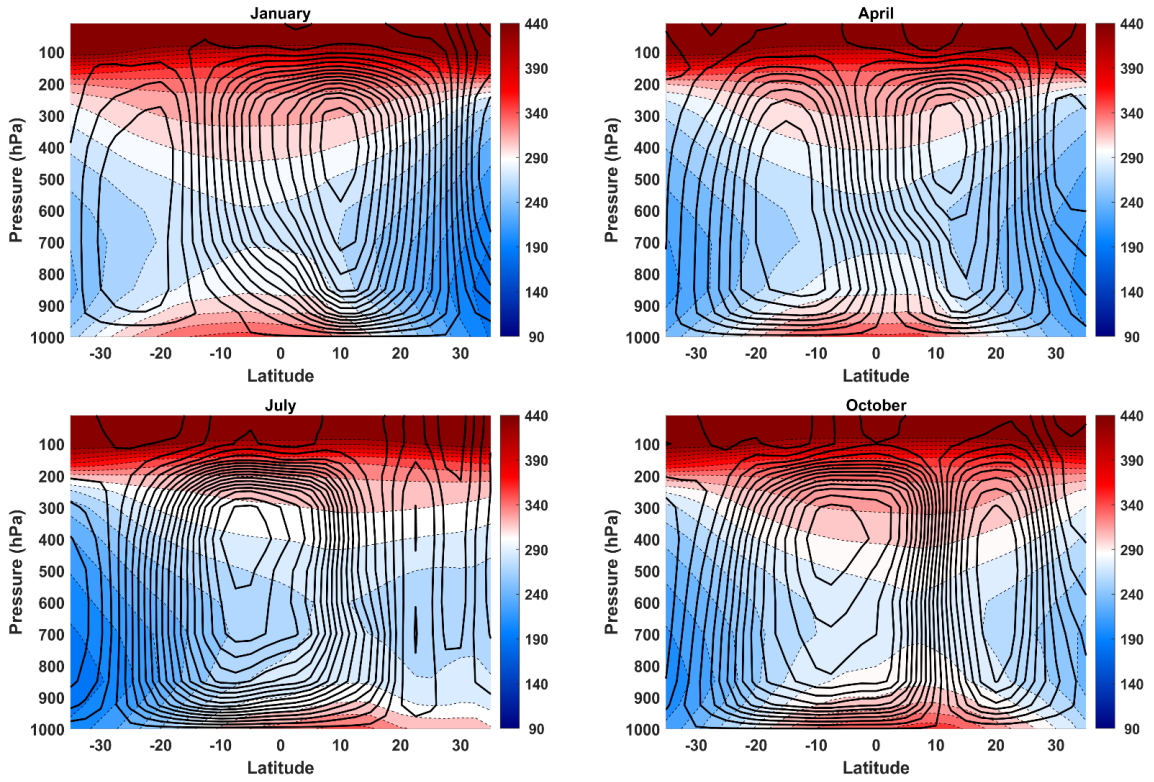

Figure 5.15: Zonal mean, monthly mean mass streamfunction (0.1 Kg m^{-1} s^{-1}) (black contours) superimposed on zonally averaged, monthly mean most entropy given by eq. (2.69), (shading), both from NCAR/NCEP reanalysis data, 1979-2019. Refer to Figure 5.14 for mass streamfunction scale and sign. The moist entropy is capped at 440 J Kg^{-1} K^{-1} to avoid having the plot dominated by large values in the stratosphere.

The vertically averaged, mass-weighted northward flux of entropy is given by the vertical average of the product of the moist entropy and the meridional wind in Figure 5.15. (Note that the meridional energy flux is more nearly given by the flux of moist static energy, not entropy, but the two are qualitatively similar.) It is clear from Figure 5.15 that this vertically averaged meridional entropy flux is generally away from the locus of maximum ascent since the entropy in the top branches of the cells is systematically greater than that in the bottom branches.

The monthly mean zonal wind is shown in Figure 5.16. At the surface, easterlies prevail throughout the tropics, except for a small region around 3-10 degrees north latitude in July. The latitudinal range of tropical easterlies shrinks with altitude, although easterlies prevail near the equatorial tropopause in all seasons. Subtropical jets near the tropopause are strongest in the winter hemisphere and fairly symmetric about the equator near the equinoxes.

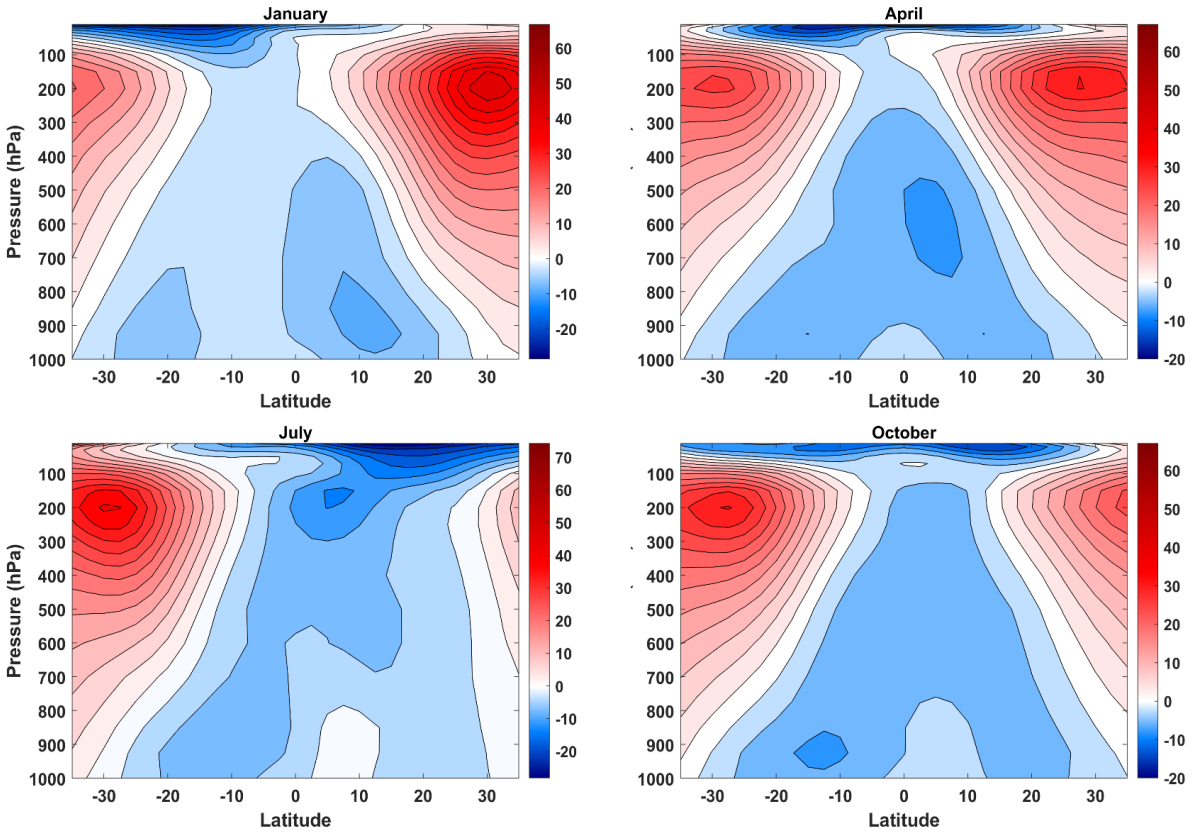

Figure 5.16: Zonal mean, monthly mean zonal wind for January, April, July and October compiled from NCAR/NCEP reanalysis data, 1979-2019.

Of some interest for the dynamics of the Hadley circulation, addressed in the next section, is a quasi-conserved quantity strongly related to the zonal wind: the absolute angular momentum per unit mass:

$$M = a\cos(\theta)\left[\Omega a\cos\ \theta\ + u\right], \tag{5.3}$$

where a and Ω are the mean radius and angular rotation rate of the earth, θ is latitude, and u is the zonal velocity. In 5.3) the local distance from the center of the earth has been approximated by the mean planetary radius (i.e. variations with altitude have been neglected along with the departures of the surface from a perfect sphere). The equations of motion on a sphere demonstrate that M is materially conserved in zonally invariant motion in the absence of frictional torque.

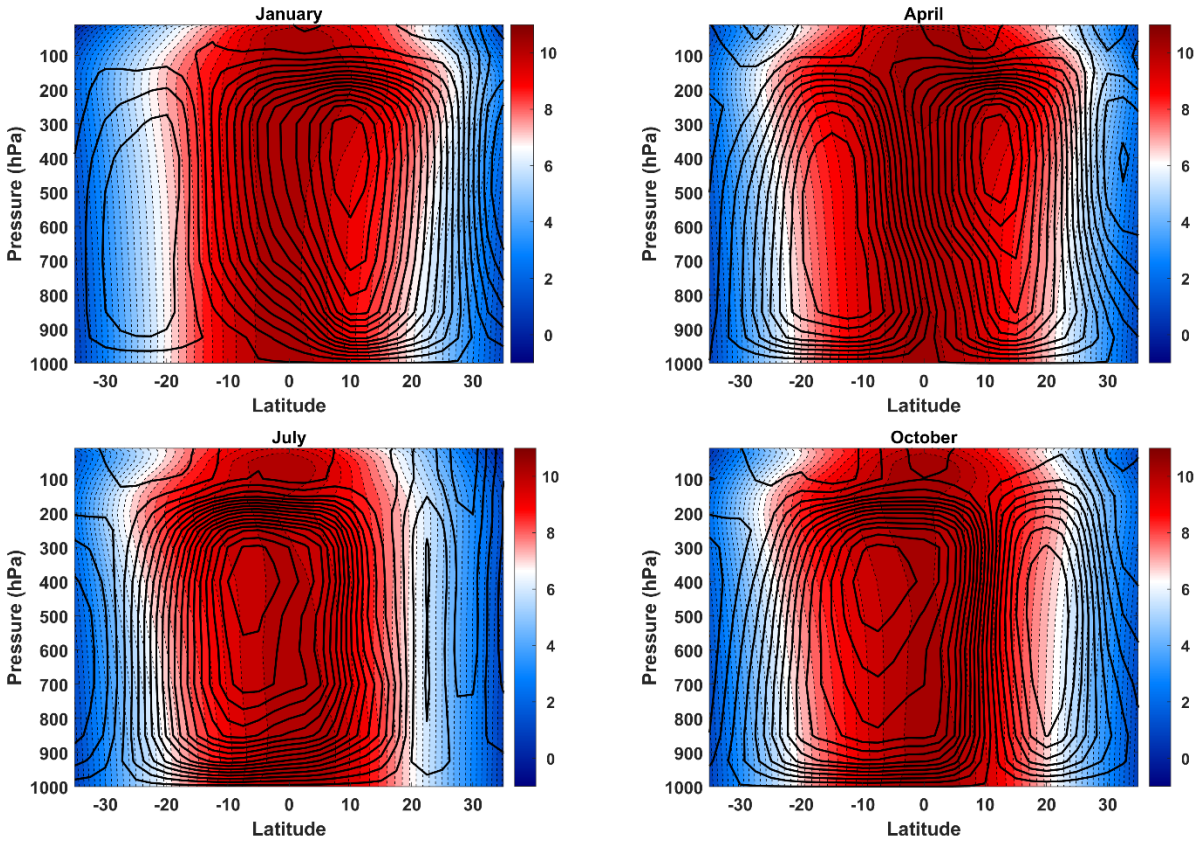

Figure 5.17: Zonal mean, monthly mean absolute angular momentum per unit mass (shading; in 10^8 m^2s^{-1}) and mass streamfunction (black curves) for January, April, July and October compiled from NCAR/NCEP reanalysis data, 1979-2019. Consult Figure 5.14 for mass streamfunction sign and magnitude.

Figure 5.17 shows the long-term mean of monthly values of absolute angular momentum with the mass streamfunction from Figure 5.14 superimposed. While the ascending and descending branches of the Hadley Circulation are more or less along curves of constant M, there is strong flow across M contours in the boundary layer and also in the return branches in the upper troposphere. The flow across M contours in the boundary layer mostly reflects the frictional torque surface drag exerts on the zonal boundary layer flow. Aloft, the cross-M flow partially reflects strong eddy fluxes of angular momentum out of the tropics, accomplished mostly by synoptic-scale eddies, and partially reflects the non-steadiness of the flow owing to seasonal variations (Boos and Emanuel, 2008). We will have more to say about the role of non-stationarity and eddy fluxes in the next section.

The Hadley Circulation is thermally direct, as can be seen in Figure 5.18 which shows the distribution of a temperature-like variable with the mass streamfunction imposed. The temperature variable is defined in terms of the saturation entropy, which is just the moist entropy of air saturated at a given pressure and temperature, and is given, following (2.69) by

$$s^* = \left(c_{pd} + r^* c_l\right)\ln\left(\frac{T}{T_0}\right) - R_d \ln\left(\frac{p_d}{p_0}\right) + \frac{L_v r^*}{T}, \tag{5.4}$$

where the symbols have their usual meanings (see Chapter 2) and r^* is the saturation mixing ratio. Because r^* is a function of temperature and pressure alone, s^* is a function of

temperature only on isobaric surfaces, so it measures buoyancy, but neglecting the direct effect of water on density. The shaded quantity in Figure 5.18 is actually the difference between s^* and it value at the same pressure at the latitude where the lowest level actual entropy (Figure 5.15) reaches its maximum value. Furthermore, we replace s^* by the actual entropy, s, at levels below 850 hPa. By design, this quantity vanishes at all altitudes at the latitude of maximum boundary layer entropy, and generally decreases away from this latitude, in the troposphere.

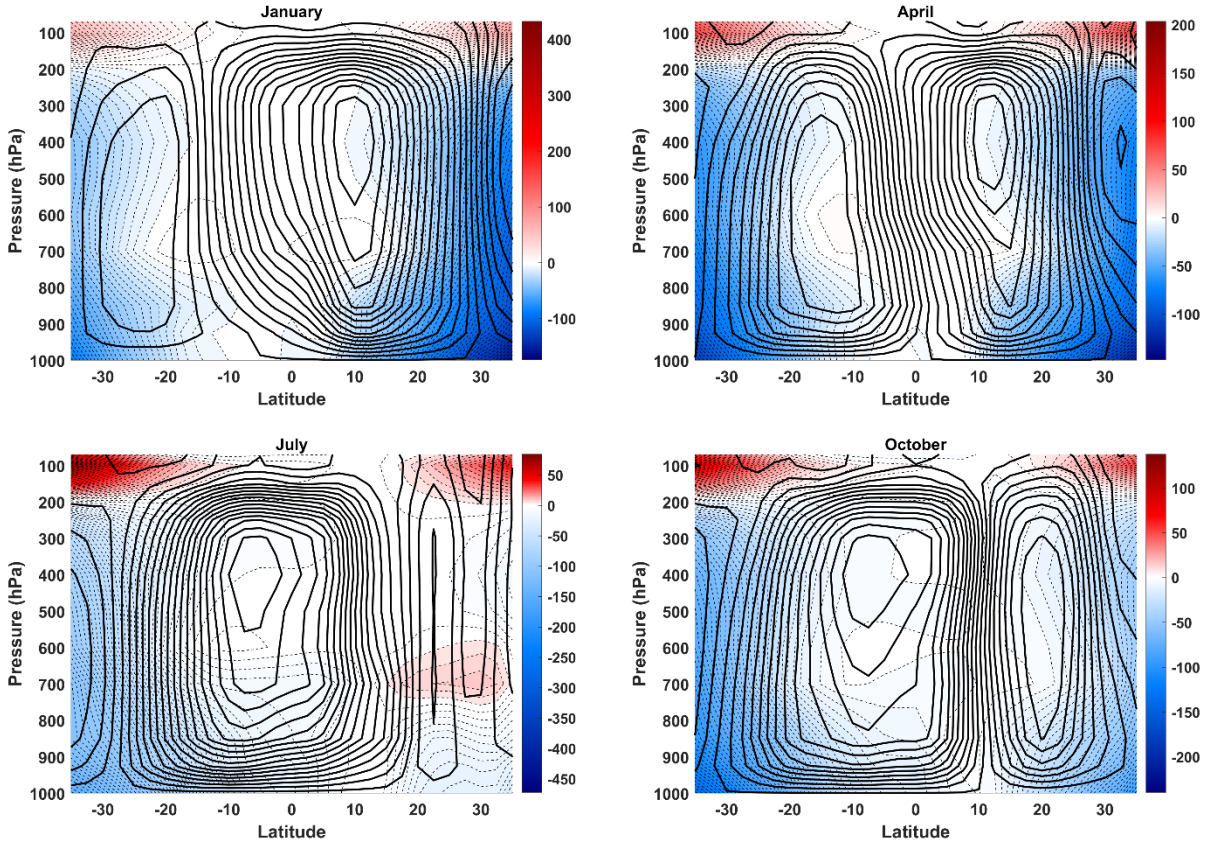

Figure 5.18: Zonal mean, monthly saturation entropy (shaded) and mass streamfunction (black curves) for January, April, July and October compiled from NCAR/NCEP reanalysis data, 1979-2019. The shaded variable is actually the difference between the actual saturation entropy and its value at the same pressure at the latitude at which the boundary layer entropy has its maximum value. (See text for more details, and consult Figure 5.14 for mass streamfunction sign and magnitude.)

As expected, this variable is nearly constant in the deep tropical troposphere, within the ascending branches of the Hadley Circulation. The descending branches are colder, demonstrating that the circulation is thermally direct, converting potential energy into kinetic energy. However, as we will discuss in the next section, this fact does not prove that the Hadley Circulation is driven by temperature gradients; indeed, the causal pathway for the Hadley flow is still a matter of debate among tropical researchers.

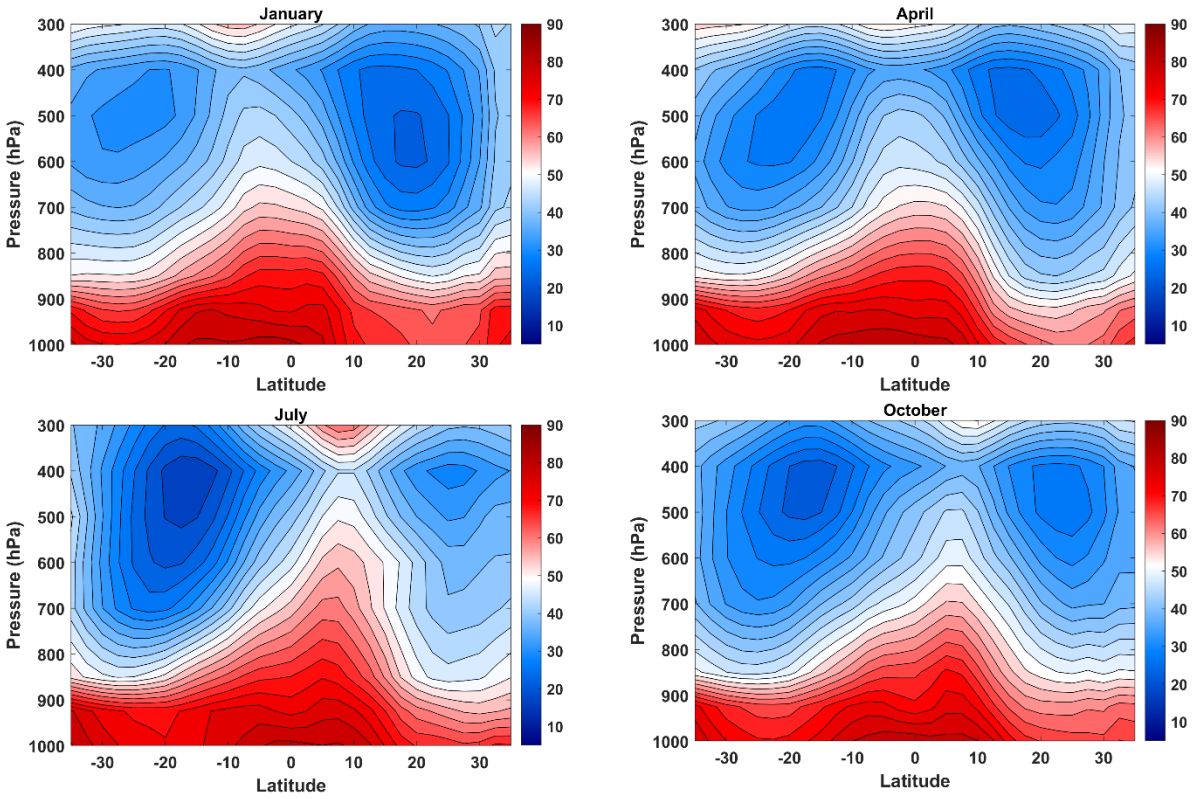

Figure 5.19: Zonal mean, monthly relative humidity (%) for January, April, July and October compiled from NCAR/NCEP reanalysis data, 1979-2019. Note that in contrast to the previous figures, 300 hPa marks the top of these diagrams as NCAR/NCEP reanalyses do not provide water vapor above this level.

Finally, Figure 5,19 shows the zonal mean, monthly mean relative humidity averaged over the same period (1979-2019). Relative humidity peaks in the near-equatorial boundary layer and decreases rapidly upward, reaching a minimum around the 400 hPa level. (This is consistent with single-column RCE calculations, as shown for example in Figure 3.20, and these simulations strongly suggest that relative humidity increases above 400 hPa and often reaches saturation at the tropopause.) The latitude of maximum humidity oscillates north and south with the seasons. Relative humidity has minima in the subtropics that are more extreme in the winter hemisphere.

Unlike temperature, which is dynamically constrained to vary slowly with time and space in the tropics, water vapor is a passive tracer in the vast majority of tropical air that is unsaturated, and typically varies at all time and space scales. Zonally and temporally averaging these distributions yields, as one would expect, the smooth distributions shown in Figure 5.19, but the reader should not be fooled into thinking that these are representative of typical water vapor distributions. Indeed, a snapshot of water vapor at 600 hPa (Figure 5.20) serves to remind us of the enormous space-time inhomogeneity of water vapor.

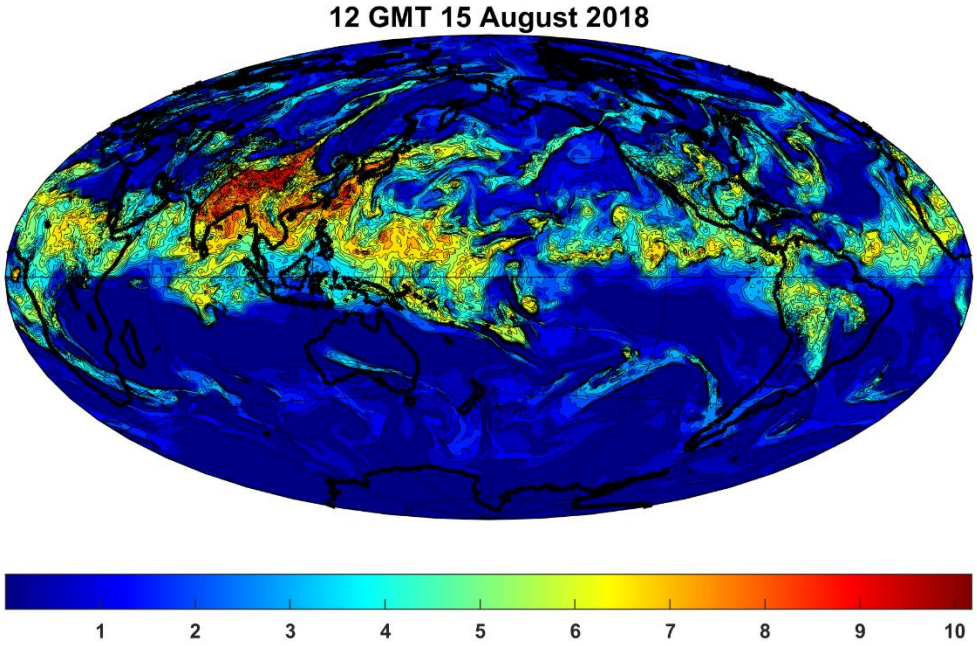

Figure 5.20: Specific humidity (g Kg^{-1}) at the 600 hPa level at 12 GMT on 15 August, 2018, from ERA-5 reanalysis data.

5.2 The Hadley Circulation

The relative zonal symmetry of the radiative imbalance, time-mean winds, temperature, and pressure in the tropical atmosphere suggests that, to first order, we might approximate the Hadley Circulation as a two-dimensional, steady overturning, symmetric about the equator, as though there were a perpetual equinox. We will start from this radical simplification and later introduce progressively more realistic physics.

To begin with, it is not at all obvious that there should be a thermally direct, Hadley-like circulation on a rotating planet with no seasons. To see the point, consider this counter-factual hypothesis: Each column of the tropical atmosphere is individually in an RCE state. Owing to diminishing insolation with attitude, the temperature of this state decreases poleward, giving rise to meridional pressure gradients. These pressure gradients are everywhere in geostrophic balance with a zonal wind. For energetic consistency, we demand that these pressure gradients and zonal winds vanish at the surface and that the interior of the atmosphere is inviscid, so that there is no dissipation of mechanical energy. The zonal wind blows along contours of entropy and angular momentum, so that these quantities are not advected and the RCE state is maintained.

If we assume geostrophic and hydrostatic balance, and that the vertical lapse rate is everywhere moist adiabatic, approximated here by constant s^* as given by (5.4), then we can derive an analytic solution for the zonal winds as a function of the meridional distribution of boundary layer moist entropy, s_b.

We begin with the expression of zonal geostrophic balance in pressure coordinates on a sphere:

$$\left(\frac{\partial \phi}{a \partial \theta}\right)_p = -2\Omega \sin\theta u - \frac{u^2}{a}\tan\theta, \tag{5.5}$$

where ϕ is the geopotential, u is the zonal wind, Ω is the angular velocity of the earth's rotation, a is the mean radius of the earth, and θ is latitude. Using the absolute angular momentum as defined by (5.3) in place of the zonal velocity, (5.5) can be written instead

$$\left(\frac{\partial \phi}{\partial \theta}\right)_p = -\sin\theta\left[\frac{M^2 - \Omega^2 a^4 \cos^4\theta}{a^2 \cos^3\theta}\right]. \tag{5.6}$$

The hydrostatic equation in pressure coordinates is

$$\frac{\partial \phi}{\partial p} = -\alpha, \tag{5.7}$$

where α is the specific volume. Using cross-differentiation to eliminate ϕ between (5.6) and (5.7) we can derive a thermal wind equation:

$$\frac{1}{a^2}\frac{\tan\theta}{\cos^2\theta}\frac{\partial M^2}{\partial p}=\left(\frac{\partial \alpha}{\partial \theta}\right)_p=\left(\frac{\partial \alpha}{\partial s*}\right)_p\left(\frac{ds*}{d\theta}\right), \tag{5.8}$$

since, to a reasonable approximation, α is just a function of $s*$ and p, and we recognize that in a steady, zonally symmetric flow, $s*$ is only a function of θ. We next turn to one of Maxwell's relations derived in Chapter 2 (see equation 2.74), neglecting the water vapor mixing ratio in comparison to unity"

$$\left(\frac{\partial \alpha}{\partial s*}\right)_p \cong \left(\frac{\partial T}{\partial p}\right)_{s*}. \tag{5.9}$$

Substituting this into (5.8) yields

$$\frac{1}{a^2}\frac{\tan\theta}{\cos^2\theta}\frac{\partial M^2}{\partial p}=\left(\frac{\partial T}{\partial p}\right)_{s*}\left(\frac{ds*}{d\theta}\right). \tag{5.10}$$

We can simplify the form of (5.10) by transforming the meridional coordinate. Defining

$$y \equiv \sec^2(\theta), \tag{5.11}$$

(5.10) becomes

$$\frac{\partial M^2}{\partial p}=2a^2\left(\frac{\partial T}{\partial p}\right)_{s*}\left(\frac{ds*}{dy}\right). \tag{5.12}$$

Because $s*$ does not vary with pressure along a moist adiabat, (5.12) can be directly integrated once in pressure. Applying the boundary condition $u=0 \quad M=\Omega a^2 y^{-1}$ at the surface, integrating (5.12) yields

$$M^2=\Omega^2 a^4 y^{-2}-2a^2\left(T_s-T\right)\left(\frac{ds*}{dy}\right), \tag{5.13}$$

where T_s is the surface temperature, which may be a function of latitude. We see here that *in a moist adiabatic, hydrostatic atmosphere, absolute temperature along a moist adiabat is the natural vertical coordinate*, rather than either altitude or pressure. We will make use of this finding throughout the rest of this book.

In terms of zonal velocity, (5.13) may be written

$$u^2+2\Omega a y^{-\frac{1}{2}}u+2y\left(T_s-T\right)\left(\frac{ds*}{dy}\right)=0. \tag{5.14}$$

Since $2\Omega a$ is about $930\ ms^{-1}$, the first term in (5.12) is considerably smaller in magnitude than the second term, and so we write to a good approximation

$$u \simeq -\frac{\left(T_s - T\right)}{\Omega a} y^{\frac{3}{2}} \left(\frac{ds*}{dy} \right). \tag{5.15}$$

because y does not change monotonically across the equator, it is helpful also to express (5.15) in terms of latitude, using the definition (5.11):

$$u \simeq -\frac{\left(T_s - T\right)}{2\Omega a \sin\theta} \frac{ds*}{d\theta}. \tag{5.16}$$

5.2.1. The equatorially symmetric Hadley Circulation

We first consider the case of a perpetual equinox, when the RCE temperature peaks at the equator (ignoring the ellipticity of the earth's orbit around the sun). In that case, $s*$ is symmetric about the equator, and so the last factor in (5.16) vanishes there, but then so does $\sin(\theta)$. For the solution to be viable, the gradient of $s*$ must approach zero more rapidly than $\sin(\theta)$ as one approaches the equator. It also follows that this solution fails for any distribution of $s*$ that is not symmetric about the equator close to the equator.

We see through (5.16) that this RCE-everywhere solution has zonal winds increasing with altitude (that is, with decreasing absolute temperature) in proportion to the magnitude of the $s*$ gradient, but because of the $\sin(\theta)$ term, the strongest zonal winds will be found equatorward of the latitude of the largest magnitude of the $s*$ gradient.

On a rotating aquaplanet (no topography) with an inviscid atmosphere above the boundary layer and perpetual equinox insolation, RCE at every latitude together with the solution of (5.14) constitutes a complete, nonlinear, steady solution of the governing equations in a moist adiabatic troposphere. There is no meridional or vertical velocity and thus no Hadley cells. So why do we find Hadley cells in nature?

The answer to this question is complex, but there is one contributing factor that is readily apparent. Returning to the expression (5.13) for the angular momentum, we first note that the last term on the right has its maximum magnitude at the tropopause, where we define the absolute temperature to be T_t. (Above the tropopause, the stratosphere is not moist adiabatic and not linked to the surface through deep convection.) And the larger the equatorward $s*$ gradient, the larger the magnitude of the absolute angular momentum at the tropopause. But M cannot be arbitrarily large. Since it is materially conserved in zonally symmetric flows, obeying a diffusion equation of the form

$$\frac{dM}{dt} = \nabla \bullet \nu \nabla M,$$

where ν is a diffusion coefficient, any interior extremum of M must eventually diffuse away. Thus, in a steady state, all extrema of M must occur on boundaries. This is known as Hide's theorem named after Raymond Hide (Hide, 1969). For this reason, in a steady, zonally symmetric flow, M is bounded above by its resting value at the equator, Ωa^2. That is, from (5.13) we require that

$$-\ T_s - T_t\ \frac{ds*}{dy} \le \frac{1}{2} a^2 \Omega^2 \left(1 - \frac{1}{y^2}\right), \tag{5.17}$$

Thus the geostrophically balanced RCE solution is only viable when (5.17) is satisfied. But what if the meridional gradients of RCE temperature ($s*$) are strong enough to violate 5.17? We can interpret this as the problem that there is not enough angular momentum in the system to allow for enough zonal wind (at the tropopause) to satisfy geostrophic balance. The pressure gradients there are too large, and thus air will have to accelerate meridionally down the pressure gradient (i.e. toward the poles). To satisfy mass continuity, there will have to be a return flow at the surface. This is one mechanism for creating a Hadley Circulation, as first demonstrated by Held and Hou (1980).

One way to avoid violating Hide's Theorem is to relax the assumption that the surface zonal wind is zero. But surface drag acting on a zonal wind will lead to an Ekman drift, establishing a circulation in the meridional-vertical direction. This circulation, by advecting heat and moisture, will upset the RCE state and this will in turn change the geostrophic zonal wind. Nevertheless, we will begin by calculating the state as though this feedback is absent and later consider its effect.

So we assume that the poleward branches of the Hadley circulation conserve angular momentum, and that the value of M at the tropopause is that of air at rest at the equator, Ωa^2. Next we integrate (5.12) *downward* from the tropopause to find the zonal wind throughout the troposphere. The result is

$$u = \frac{y^{\frac{3}{2}}}{2\Omega a}\left[\Omega^2 a^2\ \left(1 - y^{-2}\right)\ + 2\ T_s - T\ \frac{ds*}{dy}\right]. \tag{5.18}$$

Comparing this with the criterion for violating Hide's theorem, (5.17), we can express (5.18) as

$$u = \frac{y^{\frac{3}{2}}}{\Omega a}\left[\ T - T_t\ \frac{ds*}{dy} - \ T_s - T_t\ \left(\frac{ds*}{dy}\right)_c\right], \tag{5.19}$$

in which the last term is, from (5.17) the critical value of the meridional saturation entropy gradient that corresponds to constant angular momentum at the tropopause. At the tropopause, the first term in brackets vanishes and, since $ds*/dy$ is negative the zonal wind will be positive. The magnitude of the westerly wind decreases downward from the tropopause and at some absolute temperature changes sign provided the magnitude of $ds*/dy$ exceeds its critical value (which we have assumed in deciding to integrate (5.12) down from the tropopause). At the surface, the zonal geostrophic wind is easterly, given by

$$u_s = \frac{y^{\frac{3}{2}}}{\Omega a}\ T_s - T_t\ \left[\frac{ds*}{dy} - \left(\frac{ds*}{dy}\right)_c\right]. \tag{5.20}$$

This expression can tell us something about how close the actual meridional gradient of $s*$ is to its critical value versus its RCE value. to answer this question, we need to know what the

RCE gradient is. Unfortunately, it is not possible to calculate it since, as it turns out, the RCE near the equator produces a runaway greenhouse problem and there is no solution. But suppose, for the sake of argument, the RCE gradient at 15 degrees latitude were twice its critical value. Then, from (5.20) and using the critical gradient given by taking the equality in (5.17), the surface zonal wind would be about $-35\, ms^{-1}$, far in excess of what is observed. We can conclude from this that the observed s^* gradient about the time of the equinoxes (when the Hadley circulation is approximately symmetric around the equator) is much closer to its critical value than it is to its RCE value (assuming it could be computed). This also means than we cannot use (5.20) with the RCE gradient of s^* to estimate the surface zonal wind and then, using Ekman balance, the meridional wind in the boundary layer. So then, how can we go about estimating the Hadley Circulation?

One way of doing this was suggested by Held and Hou (1980): Represent the net column cooling and heating rates as linear functions of their departure from RCE, and use those rates to calculate the vertical velocity and then use mass continuity to calculate the meridional flow. In essence this uses the energy budget to calculate the circulation. We will here employ a variant of Held and Hou's method based on the boundary layer quasi-equilibrium framework we developed in Chapter 3 (see (3.59)-(3.66)). This framework was developed for WTG conditions but will work for steady flows provided that horizontal moist static energy advection in the boundary layer is accounted for in addition to surface enthalpy fluxes. The modified framework consists of expressions for the net vertical velocity:

$$\rho w_b = \frac{1}{1-\epsilon_p}\left[\frac{\epsilon_p\left(F_h + adv\right)}{h_b - h_m} - \frac{\dot{Q}_{cool}}{\mathbf{S}}\right], \tag{5.21}$$

convective updraft mass flux:

$$M_u = \frac{1}{1-\epsilon_p}\left[\frac{F_h + adv}{h_b - h_m} - \frac{\dot{Q}_{cool}}{\mathbf{S}}\right], \tag{5.22}$$

and mid-tropospheric moist static energy:

$$\frac{\partial h_m}{\partial t} = -\left\langle \mathbf{V}_h \bullet \nabla h \right\rangle - G w_b - \left\langle \alpha \dot{Q}_{cool} \right\rangle + \frac{g}{p_s - p_t} F_h. \tag{5.23}$$

Here the term adv is the vertically integrated horizontal advection of subcloud layer moist static energy, which in deep convecting regions is considered equal to the tropospheric saturation moist static energy h^* :

$$adv \equiv -\frac{\rho d v}{a}\frac{dh^*}{d\theta} = -\frac{\rho d v \overline{T}}{a}\sqrt{y^3 - y^2}\,\frac{ds^*}{dy}, \tag{5.24}$$

where v is the meridional velocity, d is the depth of the subcloud layer, and $\overline{T}$ is a representative temperature of the troposphere. We use (5.17) for the critical value of the meridional s^* gradient.

In regions where deep convection is absent, we set $M_u = 0$ and $\rho w_b = -\dot{Q}_{cool} / \mathbf{S}$, and we must solve a separate equation for the subcloud layer moist static energy, h_b . Here we will use these equations, with some simplifications, to estimate the vertical circulation and convective mass flux associated with a steady, equatorially symmetric Hadley circulation under the approximation that the saturation entropy distribution with latitude is near its critical value.

First, as we are considering steady circulations, we set the left side of (5.23) to zero. We also ignore vertically integrated horizontal advection of moist static energy and assume that the tropospheric mean of the radiative cooling rate, $\left\langle \alpha \dot{Q}_{cool} \right\rangle$, is equal to the radiative cooling rate just above the top of the boundary layer that appears in (5.21) and (5.22). Then in regions of deep convection, (5.23) becomes

$$\rho w_b = \frac{1}{G}\left[\frac{\rho g F_h}{p_s - p_t} - \dot{Q}_{cool} \right] \quad M_u > 0 \ . \tag{5.25}$$

The large scale vertical velocity is just the difference between the column enthalpy increase owing to surface fluxes, and its decrease by radiative cooling. Elsewhere, subsidence warming is assumed to balance radiative cooling:

$$\rho w_b = -\frac{\dot{Q}_{cool}}{\mathbf{S}}, \quad M_u = 0 \tag{5.26}$$

For this system we will take the surface enthalpy flux, F_h, to be a specified function of latitude. If there is no advection of heat in the ocean itself, and the ocean is in thermal equilibrium, then the turbulent heat flux from the sea must equal the next radiative flux into the sea. But because of the high moisture content of the tropical lower atmosphere, the net infrared flux into the ocean is small and so F_h is dominated by the solar flux, which we specify as a function of latitude here. As a proxy for the surface enthalpy flux, we will define an RCE radiative cooling rate as that which balances the surface enthalpy flux:

$$\dot{Q}_{RCE} \equiv \frac{\rho g F_h}{p_s - p_t}. \tag{5.27}$$

So we consider $\dot{Q}_{RCE}$ so be a specified function of latitude. With this notation, we can write (5.26) and (5.27) in the form

$$\rho w_b = \begin{cases} \dfrac{1}{G}\left[\dot{Q}_{RCE} - \dot{Q}_{cool} \right] & M_u > 0 \\ -\dfrac{\dot{Q}_{cool}}{\mathbf{S}} & M_u = 0 \end{cases} \tag{5.28}$$

The vertical motion in the convecting region is just the difference between the actual cooling rate and the RCE cooling rate, divided by the gross moist stability, G. We will approximate the actual radiative cooling rate as a function of the critical saturation entropy distribution given by

the equality in (5.17). Note that mass conservation demands that the integral of (5.28) over latitude vanishes:

$$\int_0^{\theta_{max}} \rho w_b \cos(\theta) d\theta = 0, \tag{5.29}$$

where θ_{max} is the poleward boundary of the Hadley Circulation.

Given the distributions of the actual and RCE radiative cooling rates, (5.29) can be used to determine the latitudinal extent of the Hadley circulation.

We also need to insure energetic consistency. For that to be the case, there must be no net TOA (shortwave plus longwave) radiation, and in our formulation, this would mean that

$$\int_0^{\theta_{max}} \left[\dot{Q}_{RCE} - \dot{Q}_{cool} \right] \cos(\theta) d\theta = 0. \tag{5.30}$$

Note that if G is constant, this relationship is automatically satisfied if there is deep convection everywhere, according to (5.28). But in nature that is not the case, and the condition (5.30) must be used to determine the boundary between large-scale ascent and descent.

Finally, in determining $\dot{Q}_{cool}$ from the assumed critical distribution of temperature, there is a free constant that comes from integrating (5.17). We can choose this constant so that the actual and RCE values of the radiative cooling are equal at the poleward boundary of the Hadley circulation. Thus if we assume that variations in $\dot{Q}_{cool}$ are proportional to variations in s^* and integrate (5.17) in y we have

$$\dot{Q}_{cool} = \dot{Q}_{c0} + \gamma \ 2 - y - 1/y \ , \tag{5.31}$$

where $\dot{Q}_{c0}$ is the actual cooling rate in the equator and γ is related to the proportionality between variations in radiative cooling and variations in s^*.

Once we specify the solar flux as a function of latitude, which yields $\dot{Q}_{RCE}$ in our framework, and given values of G and $\mathbf{S}$, we can solve (5.29) varying $\dot{Q}_{c0}$ and the latitude separating ascent from descent so as to satisfy mass and energy conservation as expressed by (5.29) and (5.30).

Note that to solve for the large-scale ascent in this system, we have not needed to calculate the convective updraft mass flux or the moist static energy deficit of the middle troposphere, $h_b - h_m$, but we have found it necessary to calculate the latitude separating deep convection from no deep convection. But once we have calculated the ascent together with the separation latitude and the constant $\dot{Q}_{c0}$, we can then use (5.21) and (5.22) to calculate the mass flux and moist static energy deficit in the ascent region. (By definition, the mass flux vanishes elsewhere, and we lose the ability of calculate the moist static energy deficit where deep convection is absent. Technically, if the tropopause is very cold, the moist static energy of the descent region would be nearly as low as the dry static energy in this zonally symmetric model, but in nature,

zonally asymmetric eddies transport some water into the descending branches of the Hadley circulation.)

Comparing (5.28) to (5.21) in regions where deep convection does not vanish yields an expression for the difference between the boundary layer and lower troposphere moist static energies:

$$h_b - h_m = \frac{G\epsilon_p \quad p_s - p_t}{\rho g} \frac{\dot{Q}_{RCE} + adv}{1-\epsilon_p \quad \dot{Q}_{RCE} + adv - \dot{Q}_{cool} \quad + \frac{G}{\mathbf{S}}\dot{Q}_{cool}} \tag{5.32}$$

By substituting (5.32) into (5.22), we get an expression for the convective updraft mass flux:

$$\epsilon_p G M_u = \dot{Q}_{RCE} + adv - \dot{Q}_{cool} + \frac{G}{\mathbf{S}}\dot{Q}_{cool}. \tag{5.33}$$

Figure 5.21 shows a particular solution of the system given by (5.28), and (5.31) - (5.33) satisfying the constraints (5.29) and (5.30). Here we have taken the RCE insolation $\dot{Q}_{RCE}$ to depend on $\cos^2 \theta$, $\gamma = 1$, $\epsilon_p = 0.6$, $\mathbf{S} = 5\, ms^{-2}$, and $G = 0.03\mathbf{S}$.

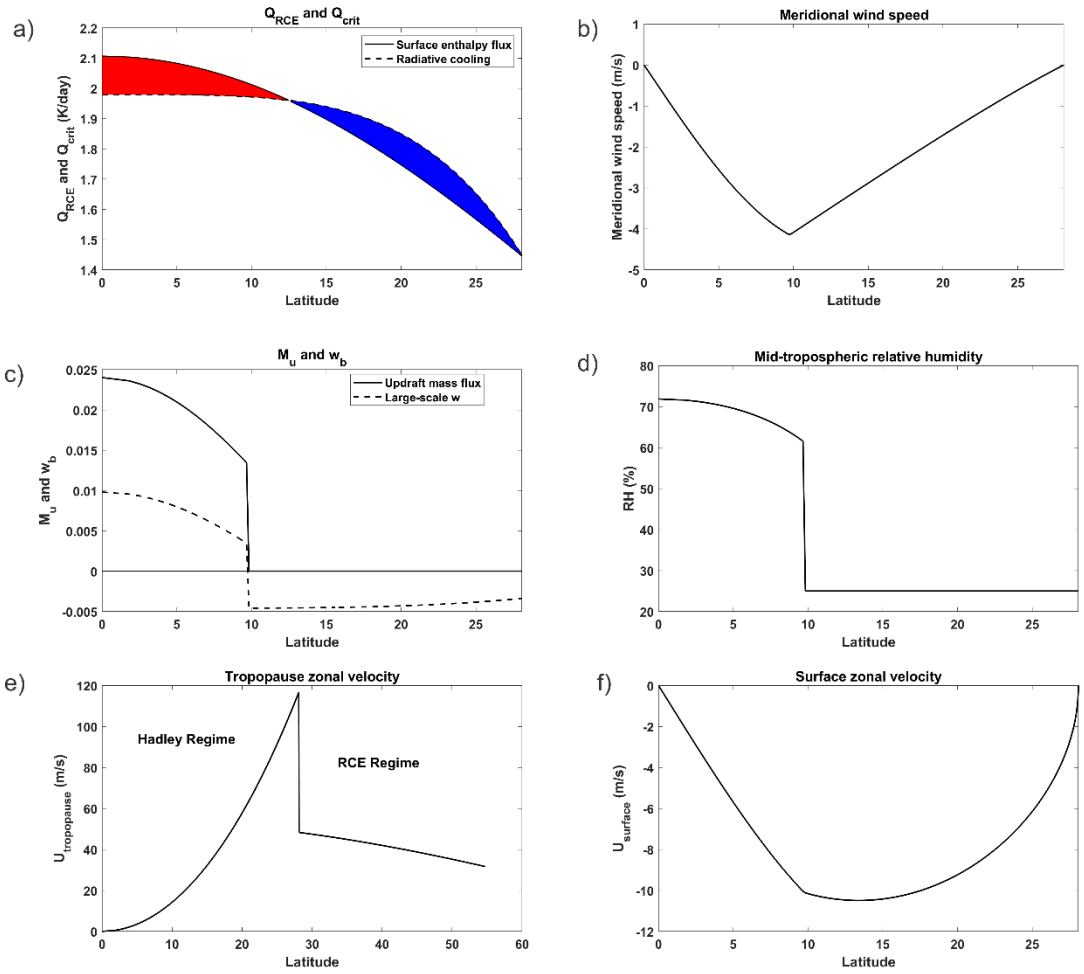

Figure 5.21: A solution for the zonally symmetric, equatorially symmetric Hadley circulation for prescribed surface enthalpy flux and radiative cooling rate proportional to the critical saturation entropy distribution. a: Surface enthalpy flux (solid) and radiative cooling (dashed); red shading indicates net heating and blue shading shows net cooling. b: Surface meridional velocity. c: Convective updraft mass flux (solid) and large-scale vertical velocity (dashed). d: Mid-tropospheric relative humidity deduced from difference between boundary layer and free troposphere moist static energies. The humidity has arbitrarily been set to 25% in the region free of deep convection. e: Zonal wind at the tropopause. Note expanded latitude scale. f: Surface zonal wind.

The ascent extends to about 9 degrees latitude, but the surface enthalpy flux exceeds the radiative cooling up to about 18 degrees. In this region, the surface fluxes are being used to increase the subcloud layer moist static energy in its journey toward the equator, rather than being used to heat the atmosphere. The meridional wind speed reaches it maximum magnitude at the edge of the region of ascent and has been calculated from the large-scale vertical velocity using mass continuity. The tropospheric relative humidity in the ascent zone has been estimated from the quantity $h_b - h_m$ given by (5.32) and set arbitrarily to 25% in the descending branch of the circulation.

While the solution shown here satisfies conservation of mass and thermodynamic energy, it does not satisfy conservation of angular momentum. As we have assumed that the actual horizontal temperature (saturation entropy) gradient is just critical – that is, having constant angular momentum along the tropopause – the poleward flow near the tropopause conserves

angular momentum, but the downflow must at some point cross angular momentum surfaces. Here it should be pointed out that the angular momentum surfaces cannot “bend over” to follow the flow downward in the subtropics. Were they to do so, the meridional gradient of angular momentum would be locally positive, which is highly unstable to small-scale inertial instability. Given this circumstance, how do Hadley circulations resolve this conundrum?

Figure 5.21e shows the zonal wind at the tropopause in this solution. Within the Hadley regime, by assumption, the temperature gradient is critical and the angular momentum is constant at its resting value at the equator. Poleward of the Hadley regime, the zonal wind is that which is consistent with the RCE temperature gradient. The zonal wind jumps cyclonically across the poleward edge of the Hadley circulation.

In nature, even a small viscosity would give rise to a flux of angular velocity across the jump in the zonal wind, transporting angular momentum from the Hadley circulation to the RCE state on its poleward flanks. This would give rise to surface easterlies in the Hadley regime and westerlies in the RCE state; note that the surface frictional sink of angular momentum at high latitudes would necessarily balance its surface frictional source in the Hadley regime.

In fact, we can estimate the flux of angular momentum to higher latitudes by “reverse engineering” the Ekman flow in the Hadley regime. In the steady state, the advection of angular momentum by the equatorward flow near the surface must balance the source of angular momentum owing to surface stress arising from a zonal wind:

$$\int_0^d \rho v \frac{\partial M}{a \partial \theta} dz = -a \cos(\theta) \tau_x, \tag{5.34}$$

where τ_x is the zonal surface stress and the integral is over the depth of the friction layer. If we assume a neutrally stratified boundary layer, then the surface stress can be well approximated by a simple aerodynamic drag formula:

$$\tau_x = \rho C_D |\mathbf{V}| u \tag{5.35}$$

where C_D is a nondimensional drag coefficient and $|\mathbf{V}|$ is the magnitude of the surface wind. If we further assume that the magnitude of the surface wind is dominated by its zonal component,

that the latter is negative (easterlies), that density does not vary much over the depth of the boundary layer, and that the angular momentum near the surface is dominated by its planetary component, then (5.34) and (5.35) can be solved for the surface zonal wind:

$$u = -\sqrt{\frac{2\Omega d}{C_D} |v| \sqrt{1 - 1/y}}, \tag{5.36}$$

with the meridional wind v given by mass continuity applied to the large-scale vertical velocity given by (5.28). This estimate of the surface zonal wind is shown in Figure 5.21f.

The required leakage of angular momentum across the poleward boundary of the Hadley circulation causes westerly winds to develop at the surface the RCE regime. The surface frictional torque exerted by these westerlies must, in equilibrium, balance the torque of the

opposite sign in the Hadley regime. From the Ekman relation (5.34), this would be associated with poleward winds near the surface, giving rise to a thermally indirect circulation known as a Ferrel Cell, after the American meteorologist William Ferrel, who in 1856 published an essay theorizing their existence. Portions of Ferrel Cells can be discerned near the edges of the panels in Figure 5.14. Ferrel Cells are thermally indirect… they are refrigerators driven mechanically by the angular momentum flux from the Hadley zones.

While zonally symmetric models (e.g. that of Held and Hou, 1980) indeed produce Hadley circulations that strongly resemble the solution shown in Figure 5.21, in reality the flux of angular momentum from the Hadley cell to middle latitudes is provided by strongly three-dimensional baroclinic eddies. The flux can be visualized by noting from quasi-geostrophic theory that the acceleration of the zonal mean zonal wind can be related to the zonal mean of the meridional eddy flux of the quasi-geostrophic form of potential vorticity. But here we instead look at the distribution of Ertel's potential vorticity, which is materially conserved in the absence of friction and heating:

$$PV = \alpha \; 2\Omega \sin(\theta)\mathbf{k} + \nabla \times \mathbf{V} \bullet \nabla s_d, \tag{5.37}$$

where α is the specific volume, $\mathbf{k}$ is the unit vector in the vertical, $\mathbf{V}$ is the three-dimensional vector velocity, and s_d is the entropy of dry air, usually represented by the potential temperature. Figure 5.22 shows a snapshot in time of the spatial distribution of potential temperature on a surface of constant PV that closely coincides with the tropopause. (This surface is usually referred to as the "dynamic tropopause".)

Extremely strong horizontal gradients of PV (or entropy on a PV surface) mark the instantaneous poleward boundary of the Hadley regime. The swirls at higher latitudes are Rossby waves associated with baroclinic instability. Chunks of high PV (or entropy on a PV surface) occasionally break off into the Hadley zone, an irreversible process known as "Rossby wave breaking", while low PV from the tropics is similarly ingested into middle and high latitudes. This wave breaking is the main agent of angular momentum flux from the tropics to higher latitudes. It is important to note that this process would occur even if the RCE temperature distribution in the tropics were subcritical and would force a Hadley-like circulation. This raises the question, still debated, about whether the actual Hadley cells are really driven by the violation of Hide's theorem or by the eddy angular momentum fluxes from the tropics to middle latitudes.

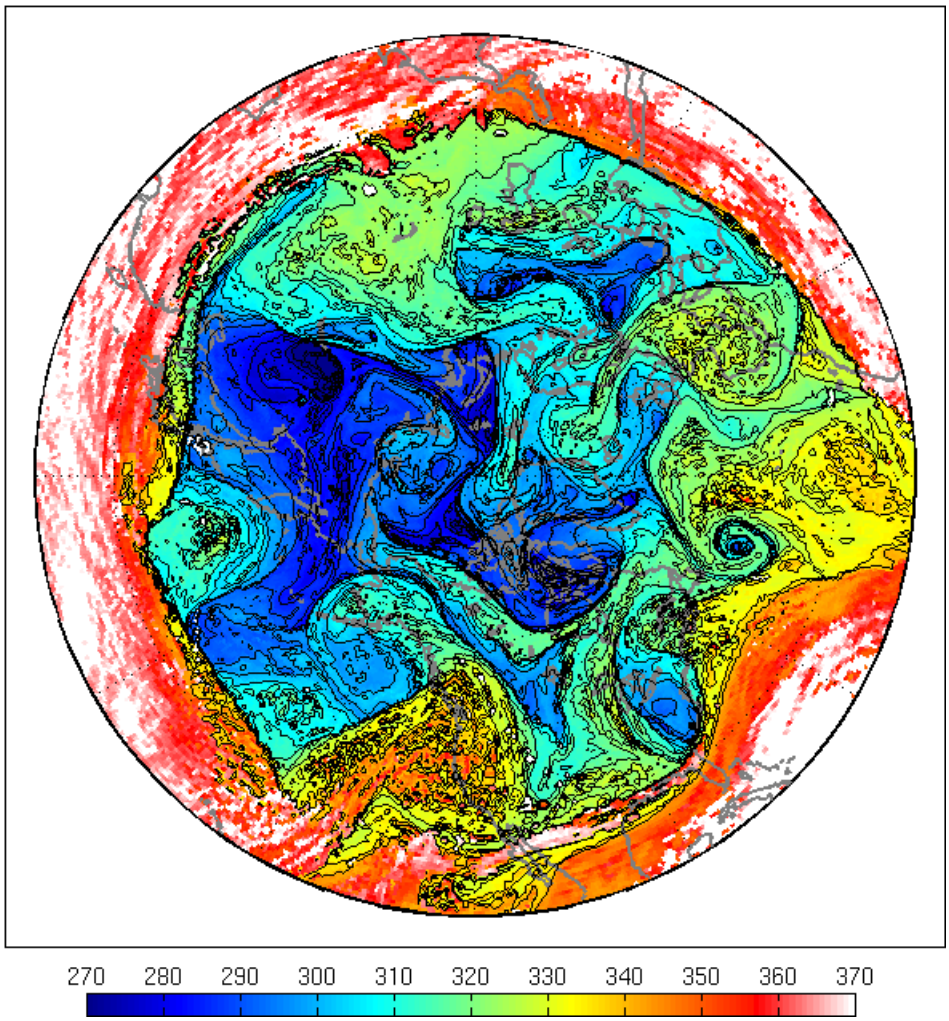

Figure 5.22: Distribution of potential temperature (K) on a surface of constant PV (the "dynamic tropopause') at 18 UTC on January 16th, 2021. The North Pole is at the center of the figure.

The divergence of the long-term average, zonal mean eddy flux of angular momentum is superimposed on the Hadley streamfunction in Figure 5.23. This is a direct measure of the sink of angular momentum by eddies and, in effect, shows the long-term zonal mean statistical effects of Rossby wave breaking. In all seasons, there are strong sinks of angular momentum in the poleward flow in the upper troposphere. As mentioned above, these sinks are necessary to close the angular momentum budget of the equatorially symmetric Hadley system. But, as described in the next section, they are not strictly necessary in the case of cross-equatorial circulations.

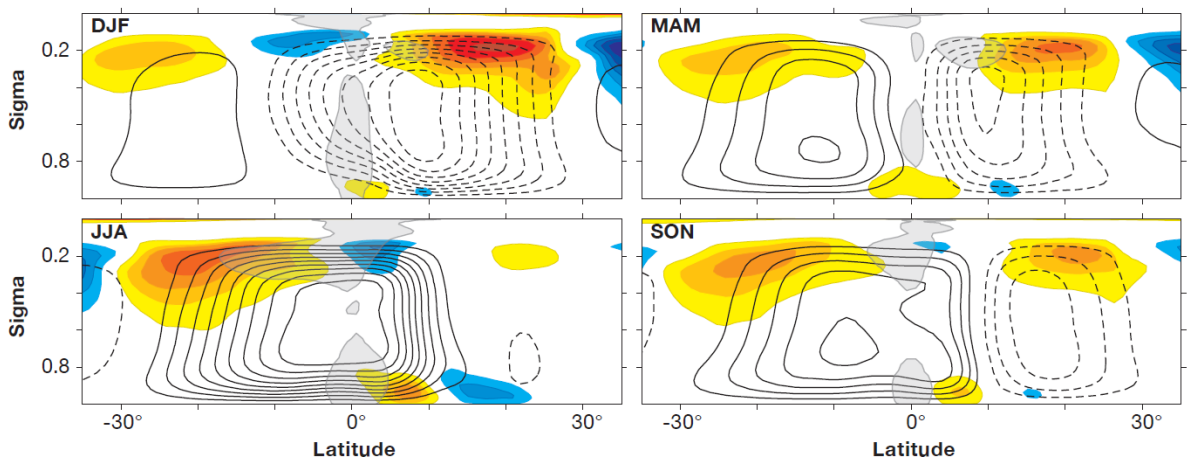

Figure 5.23: Zonal mean, seasonal mean divergence of the eddy flux of angular momentum (shading) and the mass streamfunction (black contours) for December-February, March-May, June-August, and September-November, based on European Center for Medium Range Forecasts reanalysis data average over 1980-2001. Dashed contours indicate clockwise circulation.

5.2.2. Equatorially asymmetric thermally direct circulations

When an RCE temperature gradient exists at the equator, as for example during solstices, a geostrophically balanced zonal wind is not possible and a circulation must ensue. If we continue to suppose that the circulation drives the actual temperature (saturation entropy) gradient back towards it critical value, then because of the symmetric of the thermal wind relation (5.12) and the y coordinate (5.11), it is clear that the gradient of s^* must vanish on the equator. RCE cannot be achieved there, and the gradient of actual subcloud layer moist entropy across the equator cannot match the zero gradient of s^*. Thus the subcloud layer must be convectively stable on the cold side of the equator.

For the sake of simplicity, let's continue to suppose that the RCE state is steady and zonally symmetric, but let the peak RCE temperature (s^*) peak off the equator. In what follows, we assume that the peak is in the northern hemisphere, but any solution work if the peak is instead in the southern hemisphere just by swapping the sign of the latitude and the meridional wind speed.

Poleward of the latitude of maximum s^*, which we will refer to as θ_m, the situation is much like the equatorially symmetric case. If the gradient of s^* exceeds a critical value, a thermally direct circulation must ensue; the only difference from the equatorially symmetric case is that the maximum value of the angular momentum at the tropopause is the resting value of M at θ_m, since the circulation cannot access high value of M equatorward of θ_m. We do not here take the trouble to derive such a solution but is a very straightforward extension of the development presented in section 5.2.1.

On the equatorward side of θ_m, the situation is quite different from the classical Hadley problem considered in the previous section. The RCE state will have a poleward gradient of s^*, with

easterly rather than westerly winds aloft. As long as M never decreases toward the equator, the RCE solution is viable; that is, we require that

$$\frac{dM_t^2}{dy} \leq 0, \tag{5.38}$$

where M_t is the angular momentum at the tropopause[1]. If we use (5.13) for M_t, then (5.38) can be written

$$1 + \frac{T_s - T_t}{\Omega^2 a^2} y^3 \frac{d^2 s^*}{dy^2} \geq 0. \tag{5.39}$$

(In deriving 5.39 we have neglected gradients in the difference between surface and tropopause temperature.) That is, the negative curvature of the distribution of s^* must not exceed a latitude-dependent critical value. If it does, a circulation in the vertical plane must ensue.

We could go about constructing the solution the same way we did in the equatorially symmetric case, but problems arise when angular momentum surfaces originating at the surface off the equator intersect the equator at altitude. For this reason, and to illustrate a different approach to the problem, we proceed with a slightly different method based on an alternative assumption about the vertical distribution of s^*.

Instead of assuming moist adiabatic lapse rates (constant s^*) in the vertical, we assume instead that s^* is constant along M surfaces. This is actually a more general statement of convective neutrality that includes the centrifugal as well as the gravitational contribution to buoyancy (Emanuel, 1994). Since in any case buoyancy gradients are weak, and since for simplicity we are here neglecting the contribution of water substance to density, it might be difficult to measure the difference between the two distributions in nature.

We begin by going back to the thermal wind equation (5.12). Since we are assuming that s^* is a function of M only we can write that equation as

$$\frac{\partial M^2}{\partial p} = 2a^2 \left(\frac{\partial T}{\partial p} \right)_{s^*} \left(\frac{ds^*}{dM^2} \right) \left(\frac{\partial M^2}{\partial y} \right). \tag{5.40}$$

By dividing through by $\partial M^2 / \partial y$, we find an equation for the slope, in the $y - T$ plane, of angular momentum (and therefore s^*) surfaces:

$$\left(\frac{\partial y}{\partial T} \right)_M = -\frac{\partial M^2 / \partial T}{\partial M^2 / \partial y} = -2a^2 \frac{ds^*}{dM}. \tag{5.41}$$

Since s^* is only a function of M, its derivative with respect to M is also constant on surfaces of constant M, and so the slope of M surfaces is constant…they are just straight lines in the $y - T$ plane. We can integrate 5.41 upward from the surface to arrive at

[1] Recall that the variable *y* here is the square of the secant of the latitude.

$$y = y_s + 2a^2 \ T_s - T \ \frac{ds*}{dM^2}, \tag{5.42}$$

where the subscript indicates the (latitude-dependent) value at the surface. By using the definition of y given by (5.11), we can express this in terms of latitude:

$$\cos^2(\theta) = \frac{\cos^2(\theta_s)}{1 + 2a^2 \cos^2(\theta_s) \ T_s - T \ ds*/dM^2}. \tag{5.43}$$

Now if we know the RCE distribution of $s*$ with latitude at the surface, and assume that the zonal wind is very small at the surface, we can easily calculate $ds*/dM^2$. As a particular example, suppose that

$$2a^2 \frac{ds*}{dM^2} = -\beta \left[\frac{\cos^2(\theta_s) - \cos^2(\theta_{sm})}{1 - \cos^2(\theta_{sm})} \right], \tag{5.44}$$

where β is a constant. This is a distribution in which $s*$ has its maximum value at latitude θ_{sm}. (The subscript *s* has been retained in (5.44) to remind us that this is along the surface.) Substitution of (5.44) in (5.43) would give us an explicit relationship for the shape of M and $s*$ in the latitude – temperature plane.

If all the M surfaces reach the tropopause before they reach the equator, the this "the radiative-"slantwise"-convective[2] regime (hereafter RSCE) is viable, at least in the summer hemisphere. (Note that this will not be the case if there is a gradient of $s*$ across the equator.) In the above example given by (5.44) this will be the case if β is small enough. But if the surfaces reach the equator before they reach the tropopause(which will happen here when β exceeds a critical value), then for continuity across the equator the M (and $s*$) surfaces must reconnect with their counterparts in the winter hemisphere, forming closes loops around a point at the surface and at the equator.

With the latitude of M surfaces given by (5.43) and using the definition of M, (5.3), we have

$$u = \frac{M - \Omega a^2 \cos^2(\theta)}{a \cos(\theta)} = \Omega a \frac{\left[\cos^2(\theta_s) - \cos^2(\theta) \right]}{\cos(\theta)}, \tag{5.45}$$

where once again we have assumed that $u = 0$ at the surface. Substituting (5.43) into this expression, and specifying the RCE distribution of $s*$ (for example, relation (5.44)) gives an explicit expression for the distribution of zonal wind in the latitude – temperature plane.

[2] In which moist convection is assumed to establish moist adiabatic lapse rates along angular momentum surfaces

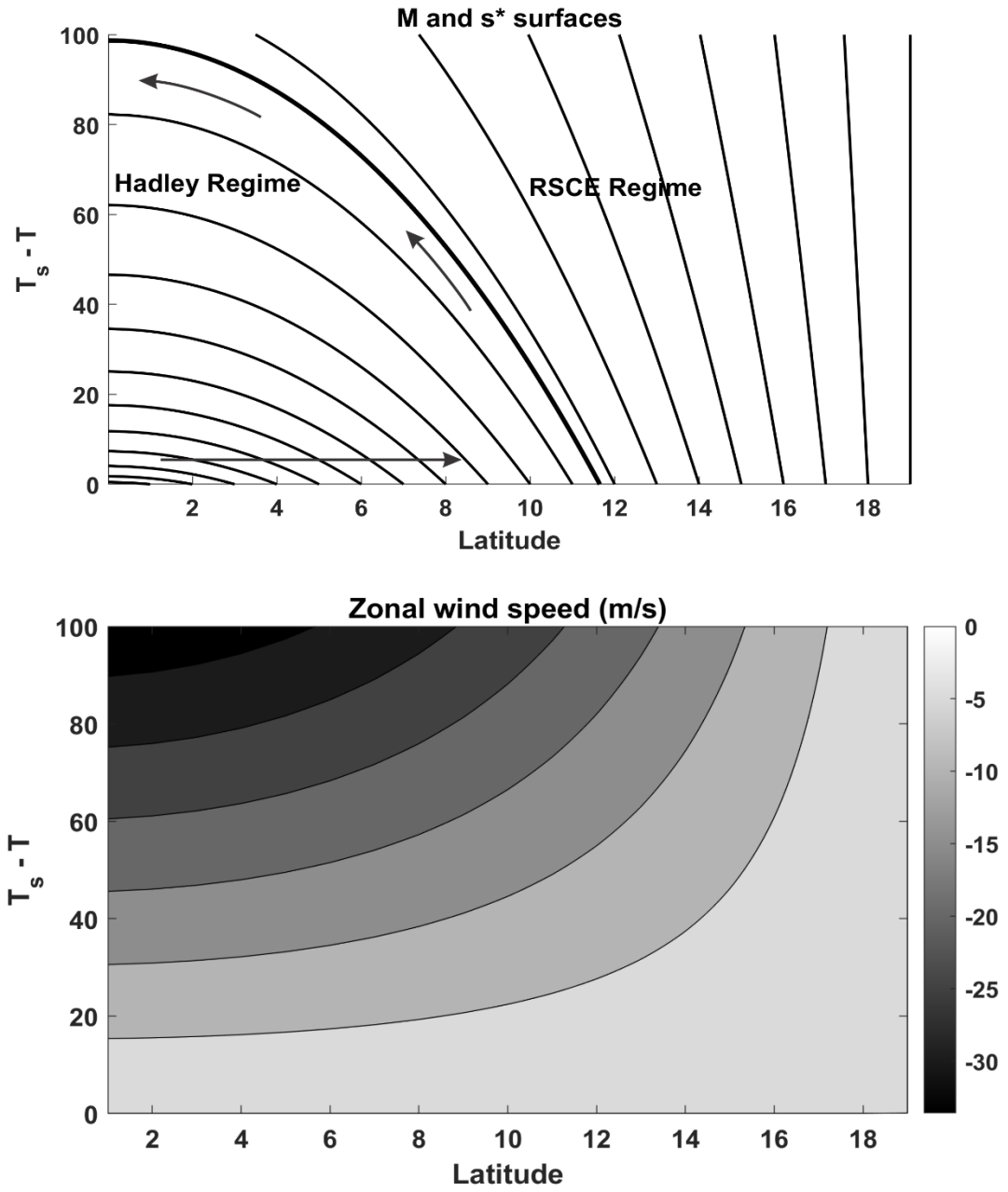

Figure 5.24: Top: Configuration of M and s surfaces as a function of latitude and the difference between the surface and local temperature (a proxy for altitude) as solutions for (5.43) – (5.45) with* $\beta = 0.0007$ *and* $\theta_{sm} = 19^{o}$. *The bold curve shows the transition between Hadley and RCE regimes. "RSCE" stands for "radiative-slantwise-convective equilibrium". Bottom: Zonal wind distribution.*

The configuration of M surfaces (which are also surfaces of constant s^*), given by (5.43) and the associated zonal wind (given by (5.45)) are shown in Figure 5.24 for the chosen distribution of s^* at the surface given by (5.44), and with $\beta = 0.0007$ and $\theta_{sm} = 19^o$. These parameter values give a supercritical distribution of s^*, so that some M surfaces intersect the equator before they reach the tropopause. Poleward of the bold curve in the top panel of Figure 5.24, the RSCE regime is viable, but equatorward of this curve the M (and s^*) surfaces intersect the equator. This leaves hanging the question of what happens on the cold side of the equator.

We have already seen that the thermal wind relation demands that the density (or s^*) distribution across the equator is locally symmetric and that, coupled with the fact that the RSCE temperature increases northward across the equator in our example, implies that the boundary layer moist entropy is too small for deep convection in the winter hemisphere. In the absence of deep convection, there must be mean subsidence to balance the radiative cooling of the atmosphere, and this implies a mass circulation with descent in the winter hemisphere and ascent in the summer hemisphere. Knowledge of the radiative cooling rate in the winter hemisphere is sufficient to calculate the mass streamfunction. In Figure 5.24 we indicate the mean ascent in the summer hemisphere. If we assume that the surface zonal winds are not very strong in the winter hemisphere, then the poleward extent of the Hadley regime in that hemisphere should match that of the summer hemisphere. Thus, above the subcloud layer, the winter hemisphere should be roughly mirror symmetric around the equator; the difference is that owing to the diminished radiative forcing in the winter hemisphere, its subcloud layer is relatively cool and stable to convection, so that the radiative cooling is everywhere balanced by subsidence.

While the assumption of relative weak surface winds requires M surfaces to re-enter the winter hemisphere boundary layer at roughly the mirror image latitude that they originate in the summer hemisphere, they may take a different path to get there. Moreover, the absence of deep convection in the winter hemisphere removes the constraint that M and s^* surfaces should be congruent. Together with the requirement that the winter hemisphere Hadley regime should blend smoothly into an RCE (or RSCE) regime in the winter hemisphere, and that the latter will be colder than its counterpart in the summer hemisphere, this suggests that the winter hemisphere temperature distribution will begin to depart from its mirror image in the northern hemisphere toward the poleward boundary of the Hadley regime.

Another consideration is that the circulation itself affects the RSCE solution of the summer hemisphere by advecting moist entropy poleward in that hemisphere. This effect was found to be quantitatively important by Privé and Plumb (2007a). The advection will reduce the boundary layer moist entropy (and therefore the free troposphere s^*) in the region of steep poleward gradients of the original RSCE solution, concentrating the gradients (and therefore the large-scale ascent) into a narrower band of latitude further poleward.

These effects are evident in aquaplanet simulations of solstitial Hadley circulations using full up primitive equations models in moist atmospheres. An example of such a simulation, using a zonally symmetric model (Pauluis, 2004), is shown in Figure 5.25.

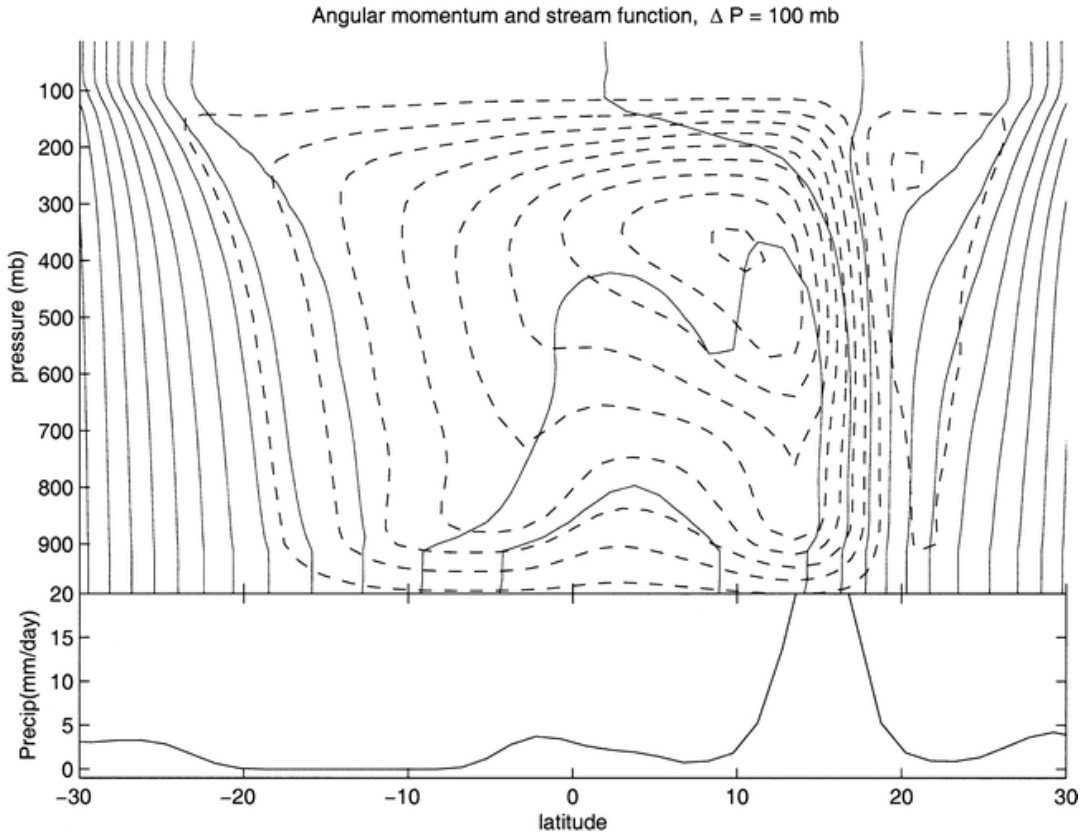

Figure 5.25: Streamfunction (dashed) and absolute angular momentum (solid) contours from a zonally-symmetric simulations of northern hemisphere summer conditions using an aquaplanet model. Precipitation is shown in the bottom panel.

There are several notable features of this simulation. First, the circulation above the boundary layer is approximately angular momentum conserving, as we assumed in our simple model and in contrast to the equatorially symmetric Hadley circulation. But, as seen in Figure 5.17, the real solstitial circulations are far from angular momentum-conserving, as indicated also by the large convergence of eddy angular momentum fluxes in the poleward branches of real circulations (Figure 5.23). Also, the ascent is indeed more concentrated than the descent, and the latter is mostly sloped the opposite way as it would be with a purely equatorially symmetric angular momentum distribution as in our simple model, consistent with the idea that the winter hemisphere temperature distribution should meld gracefully into the RSCE solution at higher latitudes.

But there is another feature of the solution in Figure 5.25 that we had not anticipated: the peculiar "jump" of the circulation across the equator, with low-level ascent in the near equatorial winter hemisphere (also evident in a minor maximum of precipitation there) and descent in the summer hemisphere. Why should that happen?

As first demonstrated by Pauluis (2004), the jump is nature's way around a dynamical conundrum, which can be seen through the lens of the meridional momentum equation. If we go back to (5.5) and relax the balance assumption, that we can write it as

$$\frac{v}{a}\frac{\partial v}{\partial \theta}+\left(\frac{\partial \phi}{a\partial \theta}\right)_p - g\frac{\partial \tau_\theta}{\partial p} = -2\Omega \sin\theta u - \frac{u^2}{a}\tan\theta, \tag{5.46}$$

where τ_θ is the meridional stress and we have neglected the vertical advection of v. The third term on the left of (5.46) is the meridional acceleration owing to the vertical convergence of meridional stress; we have neglected the horizontal convergence of stress as is traditional in boundary layer theory. If we also neglect the last term in (5.46) compared to the penultimate term, eliminate ϕ between (5.46) and the hydrostatic equation (5.7), and use Maxwell's relation as before, we get

$$\frac{\partial}{\partial p}\frac{1}{2}\left(\frac{\partial v^2}{\partial \theta}\right)-\left(\frac{\partial T}{\partial p}\right)_{s^*}\frac{\partial s^*}{\partial \theta}-g\frac{\partial^2 \tau_\theta}{\partial p^2}=-2\Omega a\sin(\theta)\frac{\partial u}{\partial p} \tag{5.47}$$

Finally we integrate (5.47) across the depth of a mechanical boundary layer whose top is defined as the altitude at which τ_θ and its vertical derivative vanish. We also assume vanishing surface zonal wind as before. The result is

$$\frac{1}{2}\frac{\partial}{\partial \theta}\left[v_s^2-v_b^2\right]-\ T_s-T_b\ \frac{d\overline{s^*}}{d\theta}-ga\frac{\partial \tau_\theta}{\partial p}=2\Omega a\sin(\theta)u_b, \tag{5.48}$$

where the subscript b denotes evaluation at the top of the boundary layer, and $\overline{s^*}$ is the vertically averaged value of boundary layer saturation entropy. Re-ordering the terms in (5.48) and using the aerodynamic flux formula for the surface stress gives

$$\frac{1}{2}\frac{\partial}{\partial \theta}\left[v_s^2-v_b^2\right]+\frac{ga\rho}{\Delta p}C_D\,|\mathbf{V}|\,v-\ T_s-T_b\ \frac{d\overline{s^*}}{d\theta}=2\Omega a\sin(\theta)u_b, \tag{5.49}$$

in which Δp is the pressure depth of the mechanical boundary layer.

Even though there can be no gradient of free tropospheric s^* across the equator, there can be a temperature gradient in the boundary layer if the cold-side boundary layer is decoupled from the free troposphere.

The first term in (5.49) is likely to be small at the equator owing to symmetry and relatively small wind shear across the boundary layer, while the last term in (5.49) vanishes at the equator. Thus, to a good approximation, on the equator

$$ga\rho C_D\,|\mathbf{V}|\,v=\Delta p\ \ T_s-T_b\ \ \frac{d\overline{s^*}}{d\theta}. \tag{5.50}$$

If the boundary layer temperature gradient is small, or the pressure depth of the boundary layer is small (or both), the meridional flow will be very small at the equator. Essentially, in the absence of Coriolis torques the is not enough meridional pressure gradient in the boundary layer to drive meridional flow against friction. For this reason, the flow turns upward on the cold side of the equator and flows, flows toward the summer hemisphere in an angular-momentum-conserving loop, descending back into the boundary layer where it can resume its poleward flow across M surfaces thanks to torque acting on surface westerlies.

Secondary maxima in precipitation on the opposite side of the equator from the main ITZC can be observed in the precipitation fields displayed in Figure 5.9, for example in the South Indian Ocean in July and in the eastern tropical South Pacific in April.

Finally, given the boundary layer meridional flow, the surface zonal wind can be diagnosed from the Ekman layer relations given by (5.34) and (5.35). This will yield easterlies in the winter hemisphere and westerlies in the summer hemisphere Hadley regimes, with very weak zonal winds near the equator.

5.2.3 The time-dependent Hadley Circulation

In Chapter 3 we showed that the time scale over which single columns with coupled slab oceans relax to their RCE state is of order 1-2 years, obviously not short compared to a seasonal cycle. For this reason, we cannot expect the Hadley circulation ever to be in an equilibrium state in the real world. There are several consequences of not being in equilibrium. First, storage of heat in the oceans becomes important, and the wind-dependence of turbulent heat fluxes from the ocean becomes a significant factor in determining the moist entropy of the boundary layer and thus the free tropospheric temperature. Also, storage of angular momentum in the atmosphere can be significant compared to advection, so flow across M surfaces does not necessarily indicate non-conservation.

Some essential features of the seasonal variation of the Hadley circulation were examined by Boos and Emanuel (2008) using a zonally symmetric moist GCM with interactive radiation and parameterized moist convection. They specified a sea surface temperature distribution in latitude that was constant everywhere except between 10^o and 40^o north latitude, where the distribution was given by

$$T_s = T_0 + \Delta T \cos^2\left(\frac{\pi}{2}\frac{\theta-\theta_0}{\Delta\theta}\right)\cos\left(\frac{2\pi t}{\tau}\right), \tag{5.51}$$

where T_0 is the constant background temperature, ΔT is the amplitude of the anomaly, θ_0 is 25^o, and $\Delta\theta$ is 15^o. The anomaly oscillates over a year, with $\tau = 365\,days$. (Note that there is no counterpart anomaly in the southern hemisphere.) The results for a simulation with $\Delta T = 3\,K$ are summarized in Figure 5.26. This is a phase diagram depicting the meridional mass flux in the boundary layer (ordinate) against the time-varying amplitude of the imposed sea surface temperature anomaly (abscissa), with the phase moving clockwise around the closed curves. The light gray curve is for a simulation in which the surface enthalpy flux is independent of wind speed while the solid black curve is for identical conditions but with the full wind-dependence of the surface fluxes included.

If the system were moving through a sequence of steady states, the phase diagram would be a single fixed curve rather than a loop and the system would just migrate back and forth along the same curve. The “thickness” of the loop is a measure of how far out of equilibrium the system is.

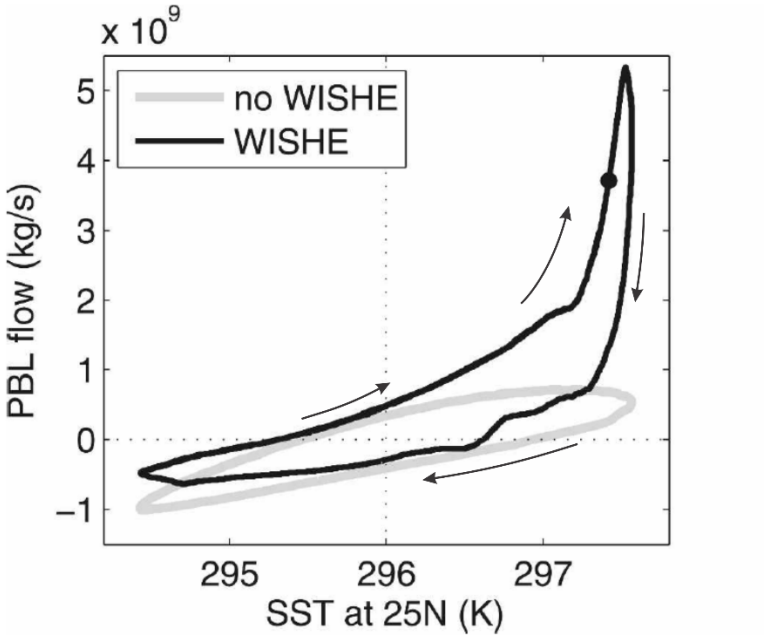

Figure 5.26: Phase diagram of meridional flow in the boundary layer (PBL flow) versus the time-varying amplitude of the imposed sea surface temperature anomaly, whose peak is at 25º N. The curved arrows denote increasing time, so the phase moves clockwise around the closed curves. The light gray curve is for a simulation in which the surface enthalpy flux is independent of wind speed while the solid black curve is for identical conditions but with the full wind-dependence of the surface fluxes included.

In springtime equinoctial conditions, the flow is toward the warming hemisphere while at the fall equinox the flow is in the opposite direction.

For the shape, latitude, and magnitude of the imposed sea surface temperature anomaly at its summer peak, the gradient of sea surface temperature, were it matched by the gradient of s^* in the free troposphere, would be in this case insufficient for angular momentum surfaces to "breakthrough" to the equator, and indeed the simulation with wind-independent surface enthalpy fluxes is weak. (Note, however, that the time dependence all by itself requires a meridional circulation to adjust the atmosphere toward the time-varying equilibrium state.) However, when the enthalpy fluxes are allowed to depend on wind, as they do in nature, a strong feedback ensues in which stronger poleward winds (and their zonal counterpart) give rise to stronger surface fluxes, which, together with meridional entropy advection in the boundary layer, steepen the boundary layer moist entropy gradient to the point of super-criticality, and a much stronger flow ensues. This feedback is often referred to as "WInd-dependent Surface Heat Exchange (WISHE)" feedback and will see that it plays an important role in many tropical weather systems.

While simulations like these with specified (though time-varying) sea surface temperature illustrate important processes such as WISHE, they do not satisfy the energy budget of the underlying ocean, implying very large and unrealistic heat fluxes within the ocean. The real system is strongly coupled, with the thermal inertia of the ocean mixed layer and lateral heat fluxes in the ocean playing important roles. Real Hadley circulations are coupled ocean-atmosphere phenomena.

You can further explore the nature of Hadley circulations, including thermodynamic coupling to a slab ocean, by running a zonally symmetric primitive equation model, using the package HadleyPak, available at this book's website. Here you may explore simulated Hadley circulations under a variety of conditions, including time-dependent and time-independent solar forcing, the effect of the interaction of radiation with clouds, coupling with a slab ocean, and other options. Figure 5.27 shows a time-latitude series of rainfall using an annual cycle of radiation and an ocean mixed layer depth of *25 m*. With this relatively small mixed layer depth, summertime precipitation extends all the way to about 30^{o} latitude, while a near-equatorial maximum can be found at most times of the year, owing to the previously discussed jumping across the equator. This gives a triple peak to the annually averaged rainfall.

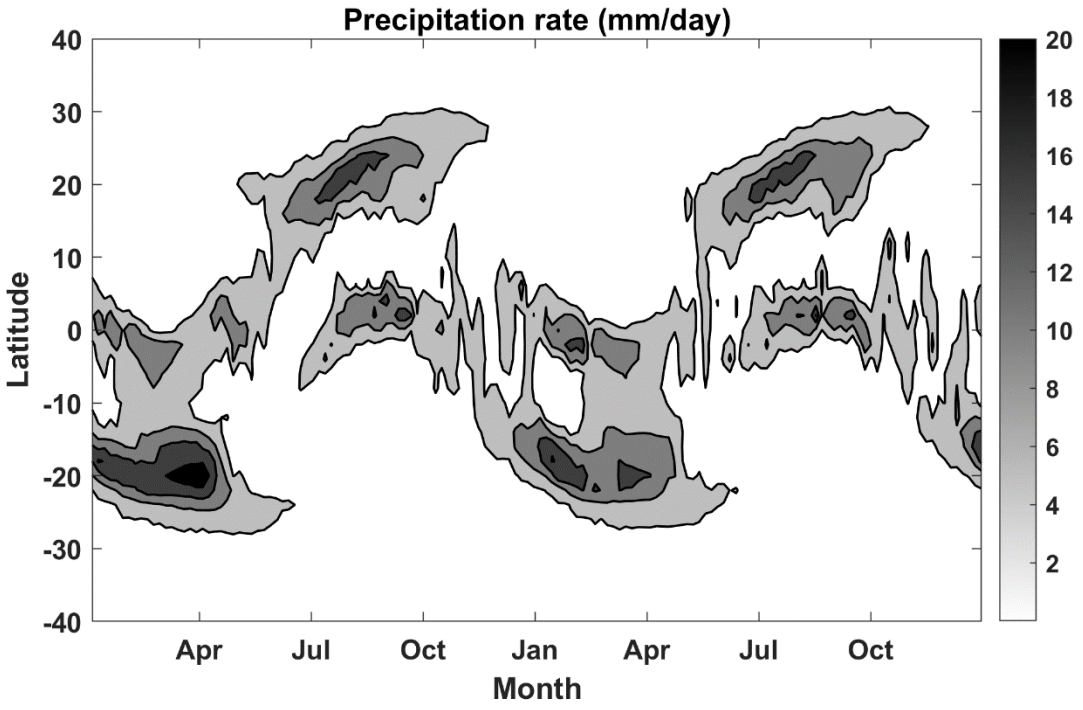

Figure 5.27: Precipitation as a function of latitude and time over two full annual cycles beginning on January 1, as output from a zonally symmetric primitive equation model coupled to a slab ocean of 25 m depth.

5.3 Monsoons

Monsoons are seasonally varying thermally direct circulations driven by land-sea contrasts, aided in some cases by the elevation of land surfaces. (In popular parlance, the term ‘monsoon’ often refers to the heavy rains associated with the summer monsoon.) They favor subtropical continents located adjacent to oceans; here the seasonal forcing is large but the Coriolis parameter is relatively small, favoring unbalanced circulations. Besides there inherent scientific interest, monsoons and their variability strongly influence the socioeconomics of the regions they affect.

Figure 5.28 shows an index of monsoon activity, defined as the difference between July and January monthly mean precipitation, shown only where magnitude of the difference exceeds *5 mm day^{-1}* and where the summer precipitation exceeds 55% of the sum of the summer and winter precipitation. In the northern hemisphere, strong monsoons are found in a region containing India, southeast Asia, and the Bay of Bengal, in sub-Saharan Africa and over the adjacent tropical North Atlantic, and in Mexico and the adjacent eastern North Pacific.

Monsoon conditions in the southern hemisphere are found in the Amazon basin, across northern Australia ad surrounding waters and across subtropical southern Africa, including Madagascar.

In the rest of this section we will focus on the Indian monsoon, as it is arguably the most studied of the monsoons, and many of the dynamical aspects of the Indian monsoon carry over to other monsoon systems.

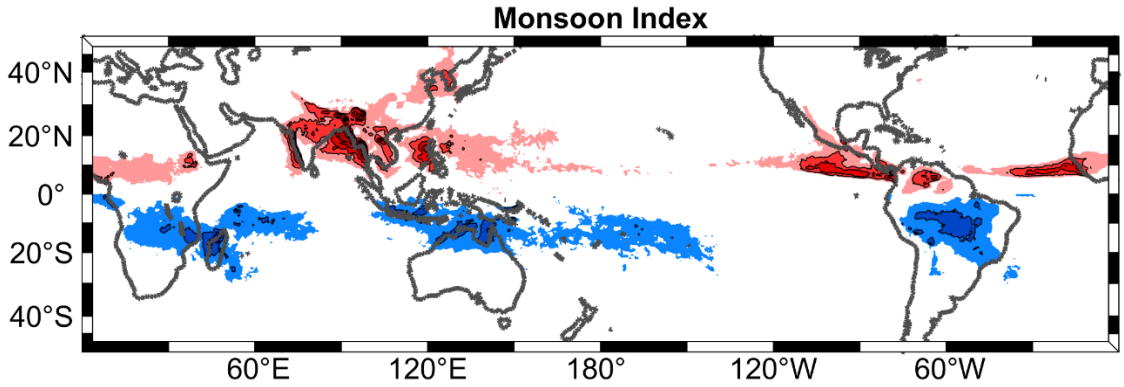

Figure 5.28: July minus January precipitation (shading) from NASA’s IMERG data based on a constellation of satellites augmented where possible with rain gauge data, 2002-2019. The quantity is plotted only where the absolute value of the difference exceeds 5 mm day^{-1} and where the summer precipitation exceeds 55% of the summer+winter precipitation.

Monthly mean rainfall over the Indian subcontinent is shown in Figure 5.29 for January and July. Clearly, almost all of India’s rain occurs during the summer monsoon, with dry conditions prevailing in the winter. During the summer monsoon, rainfall is concentrated along the western slopes of the western Ghat Mountatins that run along India’s west coast, reflecting the forced upslope flow in the strong southwesterly winds that prevail in the summer monsoon (Figure 5.30; see also Figure 5.5 for a larger scale map if surface winds). Note also the pronounced rain shadow in the lee of the Ghats.

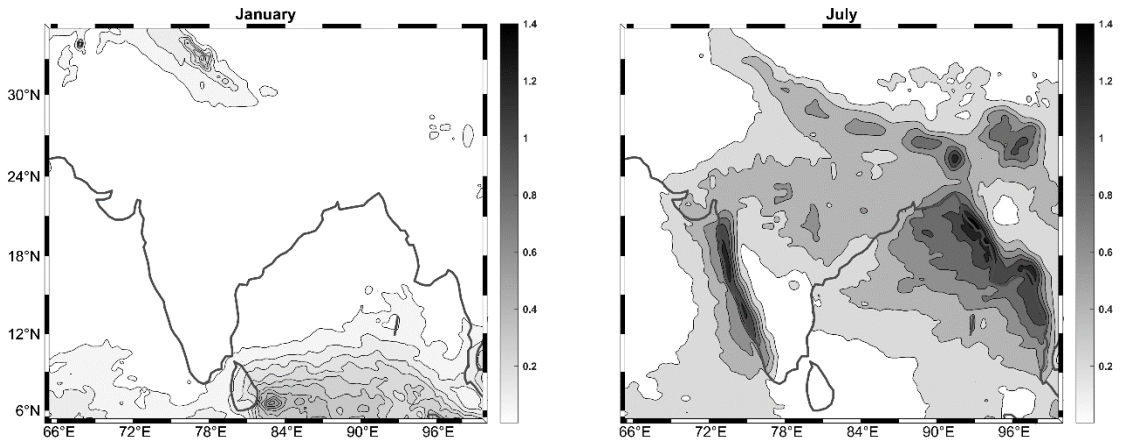

Figure 5.29: Monthly mean rainfall rate (mm/hr) in January (left) and July (right) from NASA's IMERG data based on a constellation of satellites augmented where possible with rain gauge data, 2002-2019.

Summer monsoon rainfall increases eastward across the Bay of Bengal reaching a maximum along the western coast of Myanmar. This reflects increasing boundary layer moist entropy as the strong southwesterly winds cross the Bay. Another rainfall maximum is found along the foothills of the Himalaya, forced by upslope flow.

Surface winds also dramatically differ between winter and summer (Figure 5.30), with offshore flow in January and remarkably strong southwesterly onshore flow in July. Note also the strong apparent convergence of the flow in western India and coastal Myanmar.

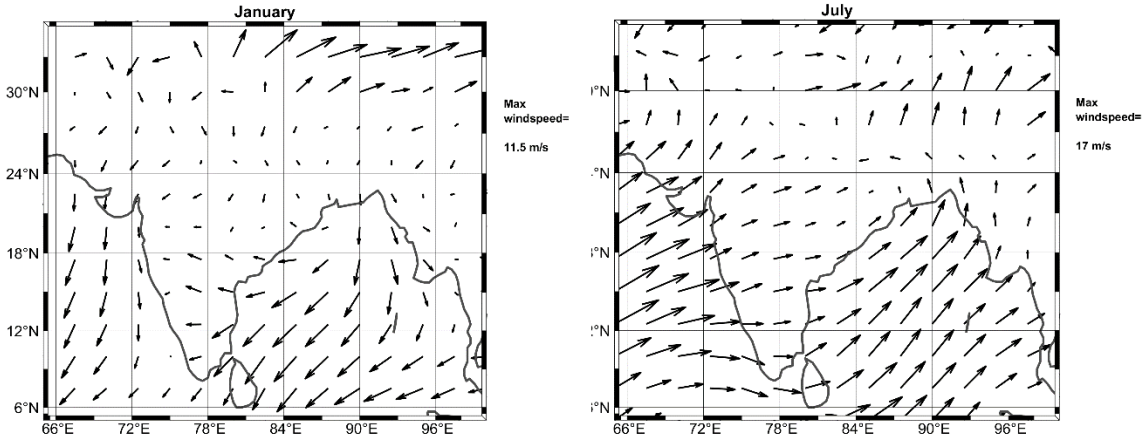

Figure 5.30: 1000 hPa winds from NCAR/NCEP reanalyses averaged over 1979-2019 in January (left) and July (right).

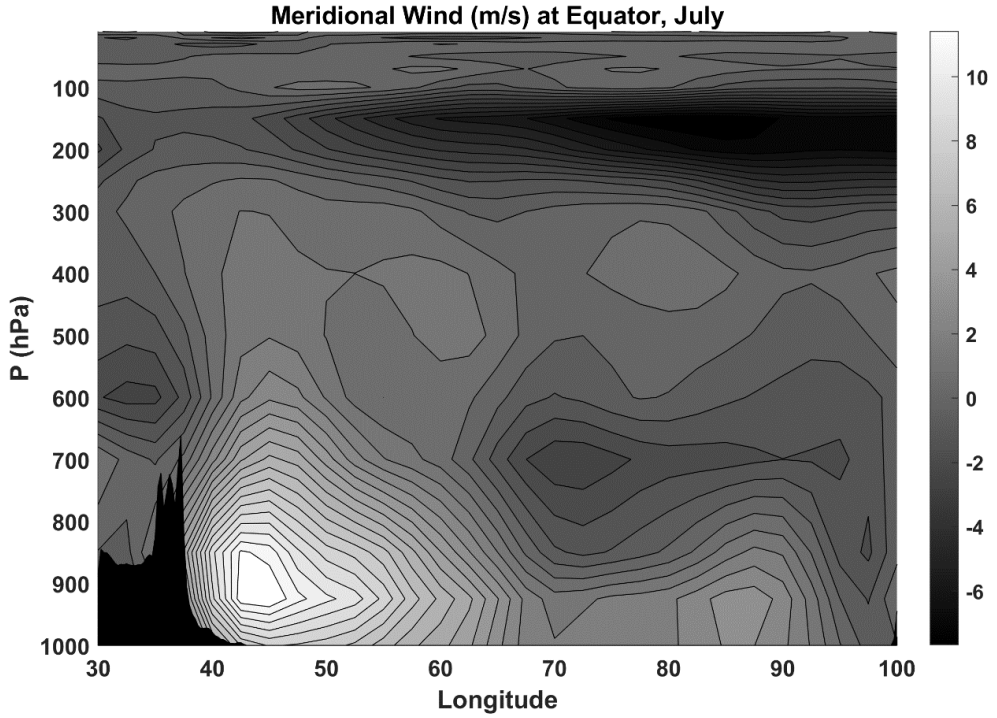

Figure 5.31: Cross-section of meridional wind across the equatorial Indian Ocean in July, from NCAR/NCEP reanalysis data, 1979-2019. The topography of equatorial Somalia and Kenya is shown at lower left.

As can be seen in Figure 5.5, the Indian summer monsoon circulation extends well into the southern hemisphere. The meridional flow is strongly concentrated into a low-level jet hugging the mountains of Somalia and Kenya. This is often referred to as the Somali Jet or the Findlater Jet (Findlater, 1969) and apparently results from the same western boundary current intensification physics as are responsible for strong ocean currents such as the Gulf Stream and Kuroshio Current (Anderson, 1976). North of the equator the strong surface flow parallel to the East African coastline drive powerful upwelling in the Arabian Sea, leading to a dramatic cooling of ocean waters in the western part of the Sea. This cooling has strong effects on marine biology and stabilizes the atmospheric boundary layer, with possible feedbacks in the monsoon circulation.

Figure 5.32 shows meridional cross-sections of flow in the latitude-pressure plane in January and July, averaged over longitudes 45W – 95W. Note that the flow vectors are not streamlines as the flow is not non-divergent in this plane. The January circulation resembles a simply cross-equatorial overturning with relatively cool, dry air sinking over the southern slopes of the Himalayas, flowing southward across the equator, and ascending near 10^{o}S. Note that the descending branch slopes down toward the south, conforming to the northward-leaning angular momentum surfaces (not shown) in the northern hemisphere.

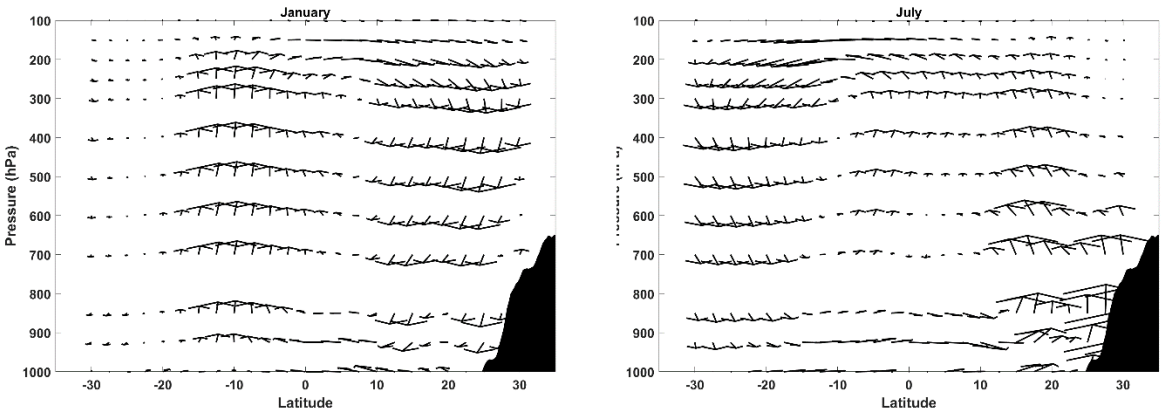

Figure 5.32: Cross-sections of circulation in January (left) and July (right), from 30°S to 30°N and averaged between 45°E and 95°E, from NCAER/NCEP reanalysis data, 1979-2019. The arrows are based on reanalysis meridional and pressure (omega) velocities. Topography shown at lower right.

The July circulation is somewhat more complex. There are three areas of ascent: Shallow ascent along the slopes of the Himalaya, deep ascent centered near 18°N and another area of deep ascent just south of the equator. Descent extends poleward of about 12°S. The circulation shares some features with model solutions sown in Figures 5.25 and 5.27, with the return branch jumping over the equator for reasons explained in section 5.2. The ascent south of the equator is associated with a secondary peak in precipitation, as shown in Figure 5.33, even more prominent than that in the zonally symmetric simulation in Figure 5.25; in fact, the secondary peak rainfall is fully 75% of the primary peak.

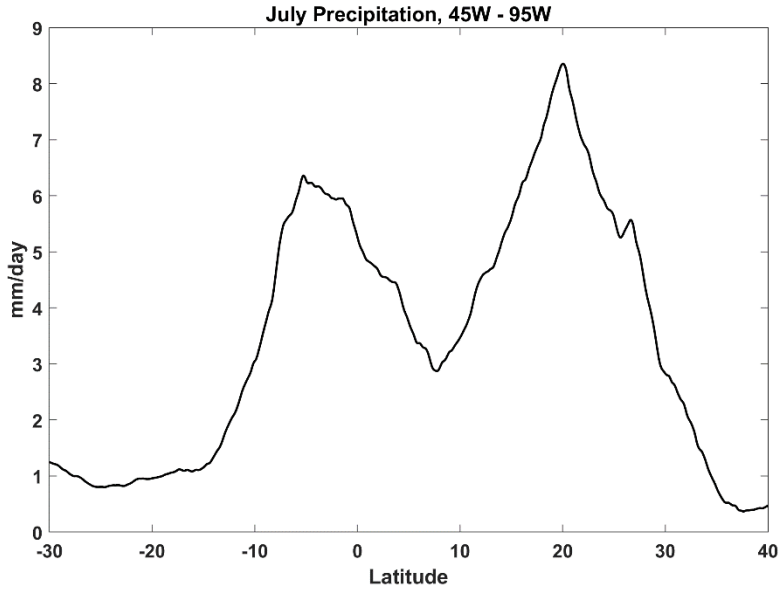

Figure 5.33: July average precipitation, zonally averaged from 45°W to 95°W using NASA's IMERG data based on a constellation of satellites augmented where possible with rain gauge data, 2002-2019.

5.3.1. Zonally symmetric theory and the effects of land

The Indian monsoon is hardly zonally symmetric, occupying about 100 degrees of longitude, but zonally symmetric theory is a useful starting point. In essence, the zonally symmetric problem is similar to the seasonally varying Hadley Circulation covered in the last section, but with one wrinkle: the surface north of some latitude is land rather than sea.

The introduction of a land surface changes the problem in some interesting ways. First, the effective heat capacity of land is much smaller than that of the ocean. On seasonal time scales, heat transfer to and from the ocean surface is transmitted by ocean turbulence through the mixed layer, but in the tropics, away from areas of deep water formation, little heat is exchanged with the deep ocean. This the heat capacity of the sea approximately corresponds to that of the mixed layer. Heat is diffused very slowly through most land surfaces, by contrast, although on season time scales one can see temperature variations down to a meter or so. In some cases, wet soil can diffuse heat much faster than when the same soil is dry, so the first rains of the monsoon can tap in to heat stored in the soil.

Focusing on the different heat capacity of land (in isolation from other effects), the theory for relaxation to RCE states developed in Chapter 3 predicts a relaxation time scale given by (3.48), as a function of the climate sensitivity of the system, the individual heat capacities of the ocean and atmosphere, temperature, and surface wind speed. For the typical values of these parameters given in Chapter 3, an ocean of depth 1 m yields an effective relaxation time scale of about 150 days, whereas one of 50 m depth has a time scale of around 750 days – 5 times longer. But note *that the RCE relaxation time scale over a surface with heat capacity characteristic of wet land is still not short compared to a year*. Thus one cannot assume that the system over land is close to an RCE state even neglecting horizontal heat transport.

Specific characteristics of the land surface, including albedo and moisture availability, will also have potentially strong effects on the RCE state over land, changing the net radiative forcing of the monsoon. All other things being equal, a dry land surface will have a drier RCE state, with less greenhouse effect of water vapor and clouds, but more surface solar radiation owing to fewer clouds. The subcloud layer will be deeper, with its dry adiabatic lapse rate yielding a higher surface temperature. The higher temperatures of the lower atmosphere coupled with lower temperatures aloft also changes the character of the monsoon forcing.

A comparison of RCE calculations with moist and dry surfaces is shown in Figure 5.34, using the single-column model discussed in Chapter 3 and available through the course website. In these calculations the dry surface is identical to the moist surface except that the surface evaporation rate from the aerodynamic flux formula is reduced by 80%. The panel on the left shows the two simulations with no clouds while the right panel compares two simulations with interactive clouds. Without clouds, the reduction of water vapor when the surface is dry cools the whole troposphere, although the surface temperature actually increases by 1 K and the lowest 50 hPa is almost as warms the moist surface case. With interactive clouds, the effect on atmospheric temperature of the reduction of water vapor is essentially cancelled by a large reduction in low clouds (not shown), so the column temperatures are nearly the same except in lower troposphere, where the dry-adiabatic layer is deeper, yielding a warmer profile.

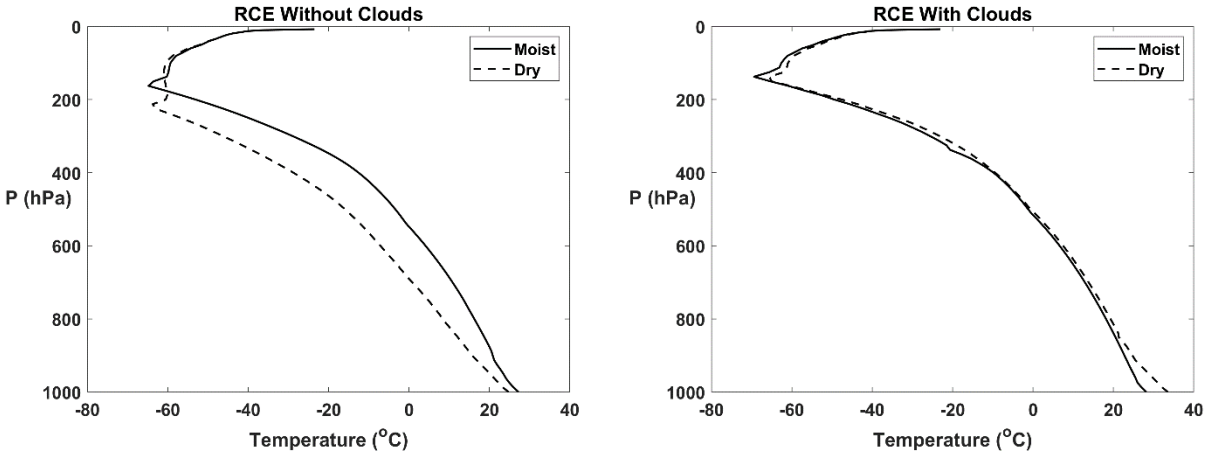

Figure 5.34: RCE calculations of the vertical temperature profile made with the single-column model with a slab ocean surface (solid) and a land surface (dashed) identical to the ocean except that the surface evaporation rate is reduced by 80%. Panel at left compares two simulations without clouds while right panel shows simulations with interactive clouds.

While this shows that interactive clouds can strongly affect the sensitivity of RCE states to surface water availability, the details of the calculations shown here are sensitive to many assumptions that have to be made about how clouds work in a single column, and so the details are likely to be wrong.

Generally, land surfaces have higher albedo than water, and this acts to diminish the RCE state temperature and thus the monsoon forcing. For example, it has long been recognized that Indian monsoon rainfall tends to be weaker in years with larger than normal snowfall in Eurasia (e.g. Blanford, 1884).

Another key element at work on land are mountains and plateaus. Mountain ranges can block the lateral advection of quantities like entropy and angular momentum, and elevated plateaus often have different RCE states owing in part to their elevation itself.

To understand this last point, consider what happens to RCE surface temperature as the altitude of the land surface increases. We will assume that this happens over a large enough area that the new RCE state would not be immediately obliterated by lateral advection from surrounding areas, but not so large that the surface pressure would fail to drop (as would be the case in the absurd limit of the whole surface of the globe expanding upward.)

First, consider the optically thin limit of an atmosphere with a very small infrared optical depth. In that case, reducing the surface pressure (i.e. elevating the land mass) would not result in any appreciable change in the infrared opacity of the atmosphere and the surface temperature would remain nearly unchanged. In this case, if we compare the RCE temperature over en elevated surface to the RCE temperature over an adjacent surface at sea level, the temperature over the elevated surface will be larger *at the same pressure level*. At the opposite extreme, in an atmosphere with very large infrared optical depth, reducing surface pressure (i.e. elevating the surface) will reduce the infrared optical depth simply because the mass of infrared absorbers above the surface is smaller. Thus elevating a surface in this case will result in a decrease in surface temperature. In general, if the conditions are not close to the limit of a runaway greenhouse, the decrease in surface temperature with elevation will not be so rapid as

along a moist adiabat, and it will continue to be the case that the temperature over the elevated surface will be greater than that over sea level, *at the same pressure*.

These inferences are confirmed by running RCE calculations over surfaces at various elevations, using the single-column model described in Chapter 3. For these simulations we hold the surface properties other than elevation constant. Figure 5.35 compares the RCE temperature profile over a water surface at 1000 hPa with on over a water surface at 600 hPa. At all pressure levels in the troposphere from 600 hPa up the temperature over the elevated surface is higher than that over sea level at the same pressure.

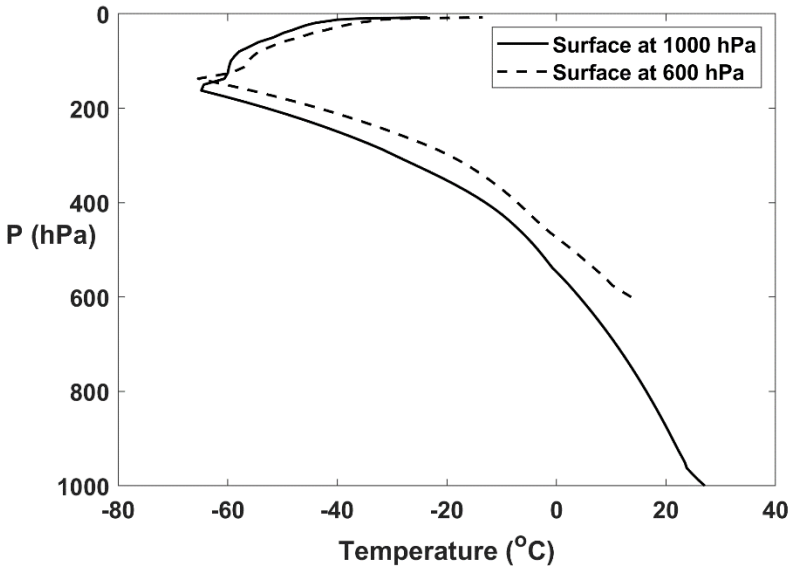

Figure 5.35: RCE temperature profiles over a water surface at 1000 hPa (solid) and at 600 hPa (dashed), calculated using the single-column model described in Chapter 3.

The Tibetan Plateau is a large area of terrain with mean surface pressures between 600 and 700 hPa, and although its albedo is somewhat higher than that of India and surrounding ocean, it is has nevertheless long been regarded as an important forcing of the Indian monsoon. The actual temperatures in the upper troposphere over the plateau are higher than elsewhere, giving rise to an extensive upper tropospheric anticyclone known as the *Tibetan High*. The July mean 200 hPa heights are shown in Figure 5.36. The highest heights are over the southern portion of the plateau, but they extend considerably southwestward of the highest topography. The westward extension of the anticyclone over the Middle East is a dynamical consequence of the forcing, as explained by Rodwell and Hoskins (2001).

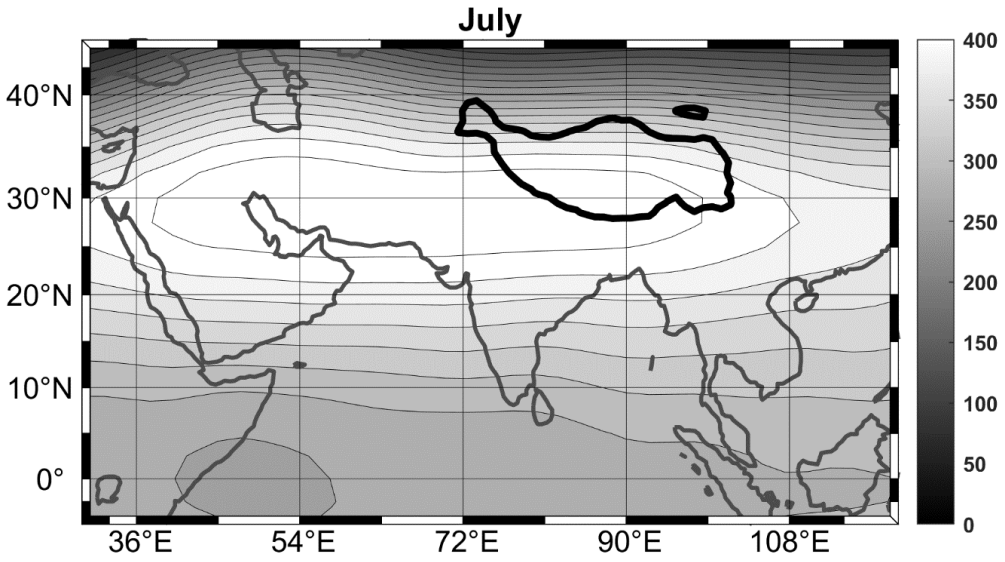

Figure 5.36: Mean 200 hPa height anomaly (m) in July, from NCAR/NCEP reanalysis data averaged over 1979-2019. The bold black curve is the 4000 m topographic contour.

The thermodynamic influence of the regional topography can be seen in the July mean fields of surface potential and equivalent potential temperature in Figure 5.37. The dry entropy (potential temperature) has a decided maximum over the plateau itself, while the moist entropy (equivalent potential temperature) has a broad maximum covering the northern Bay of Bengal, much of northern India and Bangladesh, the southern part of the Tibetan Plateau. Note also high moist entropy values in the far northern Arabian Sea.

To the extent we can regard surface entropy as a reflection of the thermodynamic forcing of the monsoon, it paints an interesting and complex picture. Referring back to Figure 5.33 and the right panel of Figure 5.32, we see that the strongest ascent and largest precipitation rates are around 20^{o}N, along the southern periphery of the largest values of surface moist entropy, from the right panel of Figure 5.37. But there is a decided but somewhat shallower secondary maximum of ascent at 30^{o}N, along the southern periphery of the region of highest surface dry entropy, as depicted in the left panel of Figure 5.37.

This is precisely what we would expect given that over the central Tibetan Plateau, the dry entropy is a maximum but the moist entropy is not, reflecting the combined effect of elevation and surface entropy and wetness. The dry summertime soils of the Plateau produce deep subcloud layers with dry adiabatic lapse rates in the daytime; this together with the surface elevation produce a maximum in potential temperature at low levels. But owing to the relatively high albedo, the surface moist entropy is not as large as that found further south over the lowlands and Bay of Bengal, thus the upper troposphere over the Plateau would be cooler if the column is convectively neutral. Thus, on the southern edge of the Plateau the low level meridional temperature gradient would be positive, but the upper tropospheric temperature gradient would be negative.

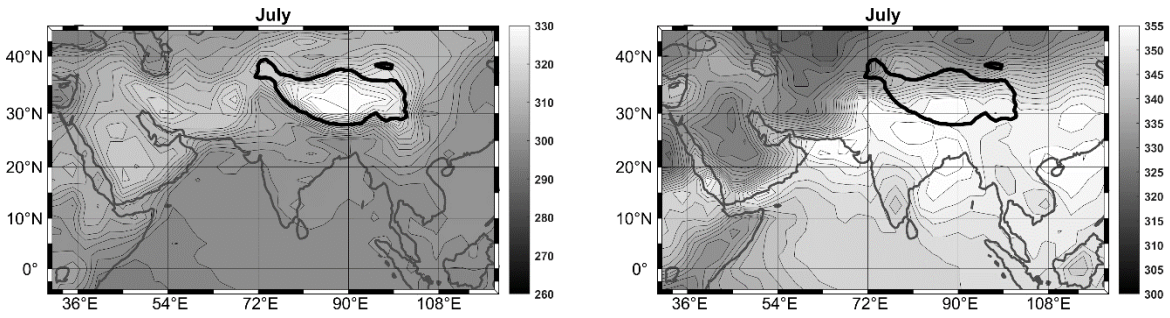

Figure 5.37: July mean surface potential temperature (left) and equivalent potential temperature (right) from NCAR/NCEP reanalyses, 1979-2019. The bold curve is the 4000 m topographic contour

Note from the right panel of Figure 5.32 that the monsoon circulation crosses the equator, even though the surface moist entropy gradient is very weak or non-existent at the equator (right panel of Figure 5.37). We also notice that our steady, zonally symmetric theoretical solution for radiative-slantwise-moist-convective equilibrium (RSCE) given by (5.43) does not require a gradient of the RSCE entropy across the equator, only a sufficiently large poleward gradient somewhere in the system, with "sufficiently large" being a function of latitude. To illustrate this, we modify the trial function of $ds*/dM^2$ given by (5.44) to have a maximum value well off the equator:

$$2a^2\frac{ds*}{dM^2} = -2\beta\left[\frac{\cos^2(\theta_s)-\cos^2(\theta_{sm})}{1-\cos^2(\theta_{sm})}\right]\left[\frac{\sin(\theta_s)}{\sin(\theta_{sm})}\right]^2 \tag{5.52}$$

This function is plotted in Figure 5.38 for a case in which the moist entropy peaks at 26° latitude. The moist entropy gradient vanishes on the equator and peaks around 25°N.

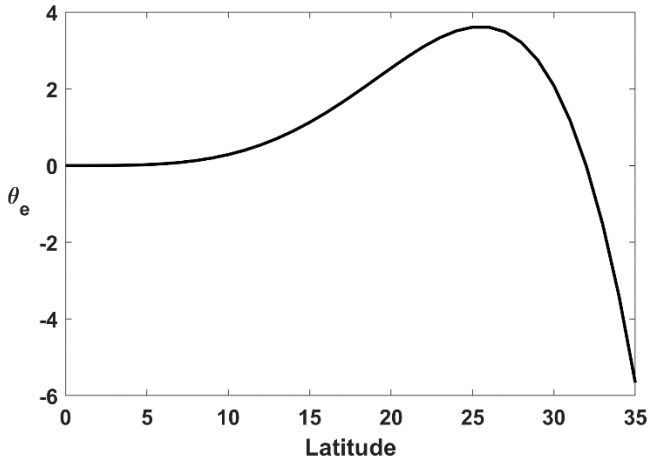

Figure 5.38: Equivalent potential temperature (K) relative to its equatorial value, as given by (5.52) with $\beta = 0.0015$ *and* $\theta_{sm} = 26^o$.

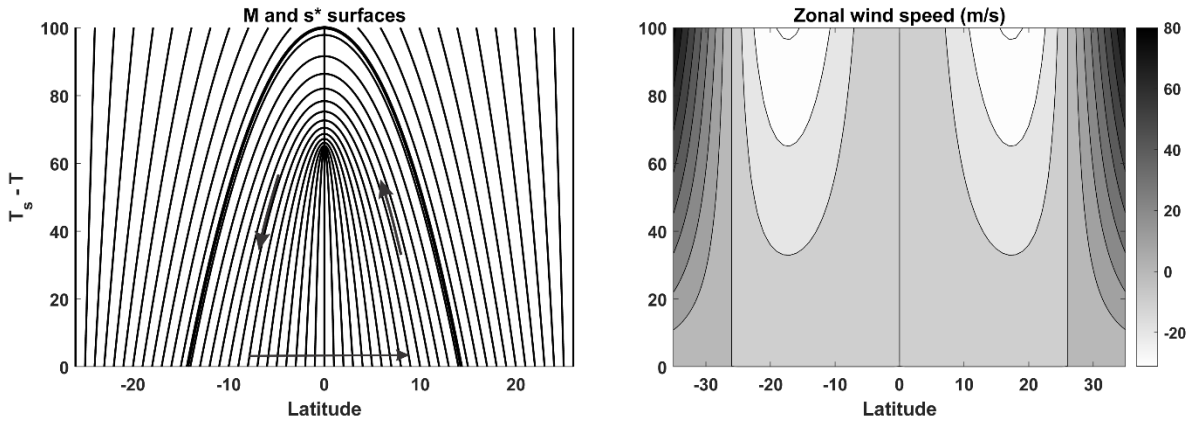

Figure 5.39: Left: Shape of $s*$ *and* M *surfaces in the solution to (5.43) with the distribution of moist entropy given by (5.52) with* $\beta = 0.0015$ *and* $\theta_{sm} = 26^{o}$ *. Bold line shows boundary of monsoon regime and arrows show sense of circulation. Right: The corresponding zonal wind speed (m/s). Note the different latitude scales of the two figures.*

As before, all of the moist entropy and angular momentum surfaces within the monsoon regime shown by the bold curve in the figure cross the equator, but the altitude at which they do so decreases toward a finite limit as their latitude of origin approaches the equator. Here again we expect ascent north of the equator and descent in the southern hemisphere, with the possibility of an angular momentum-conserving jump in the northward flow across the equator. Note that the strongest ascent will tend to coincide more nearly with the latitude of strongest poleward entropy gradient, not the latitude at which the entropy itself as a maximum. The zonal wind distribution shows easterlies everywhere above the surface equatorward of the latitude of maximum RSCE surface moist entropy, and westerlies poleward of that latitude.

The main feature of the RSCE solution is that angular-momentum-conserving cross-equatorial flow does not require an RSCE entropy gradient at the equator itself, and so thermal forcing by land-sea contrast well off the equator can cause a strong thermally direct response.

A more realistic simulation of an idealized, zonally symmetric monsoon can be made using HadleyPak, available at this book's website. This is a zonally symmetric primitive equation model using the same radiation and convection schemes as used in the single-column model made available at this book's website. For these simulations we used a latitudinal resolution of 2 degrees, spanning 40ºS to 40ºN and having land poleward of 20ºN. The ocean consists of a slab 35 m in depth and the land surface has a primitive soil moisture scheme that accounts for precipitation, evaporation, and runoff. The model does not include topography, however, and so cannot be used to explore the effects of elevated land.

Some fields produced by a simulation spanning two years are shown in Figure 5.40. The time-latitude display of precipitation in the left panel of the figure shows some interesting features. In contrast to the simulation shown in Figure 5.27, which only differed only in having an ocean surface throughout the domain, precipitation over the land begins just a few weeks after the spring equinox and migrates northward in response to solar forcing over land. Just offshore, the onset of monsoon precipitation is delayed by the downward motion associated directly with the land-sea low-level temperature contrast. This is essentially a seabreeze circulation with descent just offshore.

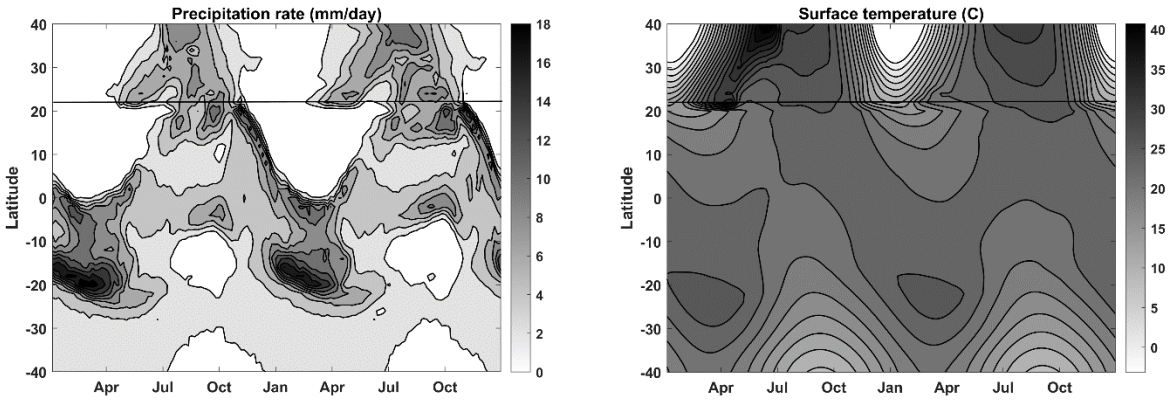

Figure 5.40: Time-latitude section of precipitation (left, in mm/day) and surface temperature (right, ^{o}C) for a simulation forced by seasonally varying TOA insolation. The horizontal line marks the boundary between land to the north and sea to the south.

But in September, as the monsoon recedes, landbreezes cause a local maximum in ascent and precipitation just offshore. In October, a narrow band of heavy rainfall forms just offshore and moves southward, reaching a southern extremity in late winter just south of the equator. A separate precipitation maximum occurs in the southern hemisphere summer in response to insolation forcing over the ocean.

The evolution over the two-year period of surface temperature is shown on the right side of Figure 5.40. The pattern is naturally dominated by the large annual cycle over land, particularly at high latitudes. Note that the temperature extreme over land occur about 1 month after the solstices, whereas over the ocean the lag is closer to 3 months.

Simulations such as these demonstrate the rich complexity of monsoon physics even before we have considered departures from zonal symmetry and other aspects of monsoon flows. In the next section we extend these results by relaxing the requirement of zonal symmetry.

5.3.2 The effects of zonal asymmetry

Zonally asymmetric thermally direct circulations differ in several fundamental ways from the zonally symmetric case we have been focused on. First, we need to generalize Hide's theorem to the case of three-dimensional flows, and second we have to consider zonal advection of entropy and vorticity.

In the zonally symmetric case, Hide's theorem forbids angular momentum from increasing toward the poles. This is equivalent to the statement that the absolute vorticity at the tropopause must never have the opposite sign as the Coriolis parameters. At a level at which the vertical velocity vanishes, it is not possible to change the sign of the absolute vorticity from its background value – the tilting term in the vorticity equation vanishes and no amount of stretching can flip the sign of the absolute vorticity. It is possible, though, to advect absolute vorticity across the equator, giving rise to absolute vorticity with the opposite sign of the Coriolis parameter. This configuration is, however, strongly unstable to inertial instability, whose effect will be to eliminate the wrong sign vorticity by mixing with adjacent regions.

Here, as in the zonally symmetric case, we seek an RCE solution that is also in dynamical equilibrium, and generalize Hide's Theorem to state that the solution must not have absolute vorticity of the opposite sign from the Coriolis parameter. A general solution that is in gradient balance is difficult to construct, but we can build an approximate one to the extent that geostrophic balance is a good approximation.

We begin with the vector form of the thermal wind equation derived by assuming geostrophic and hydrostatic balance:

$$\frac{\partial \mathbf{v}}{\partial p} = -\frac{1}{2\Omega \sin(\theta)} \mathbf{k} \times \boldsymbol{\nabla}_p \alpha, \tag{5.53}$$

where $\mathbf{v}$ is the horizontal velocity vector on isobaric surfaces and $\mathbf{k}$ is the unit vector in the vertical. Applying Maxwell's relation (5.9) and integrating (5.53) from the surface to the tropopause, assuming as before a moist adiabatic lapse rate in RCE, yields

$$\mathbf{v}_t = \frac{T_s - T_t}{2\Omega \sin(\theta)} \mathbf{k} \times \boldsymbol{\nabla}_p s^*, \tag{5.54}$$

where $\mathbf{v}_t$ is the horizontal velocity vector at the tropopause. The condition that the absolute vorticity at the tropopause have the same sign as the Coriolis parameter may be stated as

$$\sin(\theta)\ 2\Omega \sin(\theta) + \mathbf{k} \bullet \boldsymbol{\nabla} \times \mathbf{v}_t\ \geq 0. \tag{5.55}$$

Applying this to (5.54), and substituting the boundary layer moist entropy for s^* (that is, once again assuming convective neutrality) gives the condition for the dynamical viability of the geostrophically balanced RCE state:

$$\sin(\theta) \left[2\Omega \sin(\theta) + \frac{1}{2\Omega} \boldsymbol{\nabla} \bullet \left(\frac{T_s - T_t}{\sin(\theta)} \boldsymbol{\nabla} s_b \right) \right] \geq 0, \tag{5.56}$$

where s_b is the moist entropy of the boundary layer and we have used a vector identity. Here the divergence and gradient operators are those appropriate to spherical coordinates. If (5.56) is satisfied everywhere, then the geostrophically balanced RCE state may dynamically viable if the geostrophic assumption is well satisfied by the flow. Note from the thermal wind equation (5.54) that the geostrophic flow will not advect s^*, which would invalidate the steady-state assumption. On the other hand, the geostrophic flow may advect itself, depending on the shape of the s_b field, and if we revert to quasi-geostrophic dynamics, the advection of pseudo-potential vorticity may not vanish, invalidating the assumption of a steady state. (This would never be a problem, of course, in zonally symmetric configurations.)

It should be remarked, however, that potential vorticity (and its quasi-geostrophic counterpart) is not conserved in RCE states owing to the strong diabatic effects of radiation and convection. Thus if (5.56) is satisfied, the state may be approximately stationary if the advection of potential vorticity is weak compared to the diabatic tendencies to restore the potential vorticity value of the RCE state. But often the interaction of localized RCE temperature anomalies with background potential vorticity gradients causes significant transient behavior which may lead to

substantial remote effects. A case in point is the Tibetan High, which advects the background meridional gradient of potential vorticity, causing the anticyclone to stretch westward and then break of into blobs of negative potential vorticity anomaly, which move westward owing partially to the “beta drift’ effect and which cause large-scale subsidence to the west of Tibet (Rodwell and Hoskins, 2001). An example is provided in Figure 5.41. The downstream subsidence is thought to be an important contribution to the extreme dryness of the Middle East and Sahara Desert.

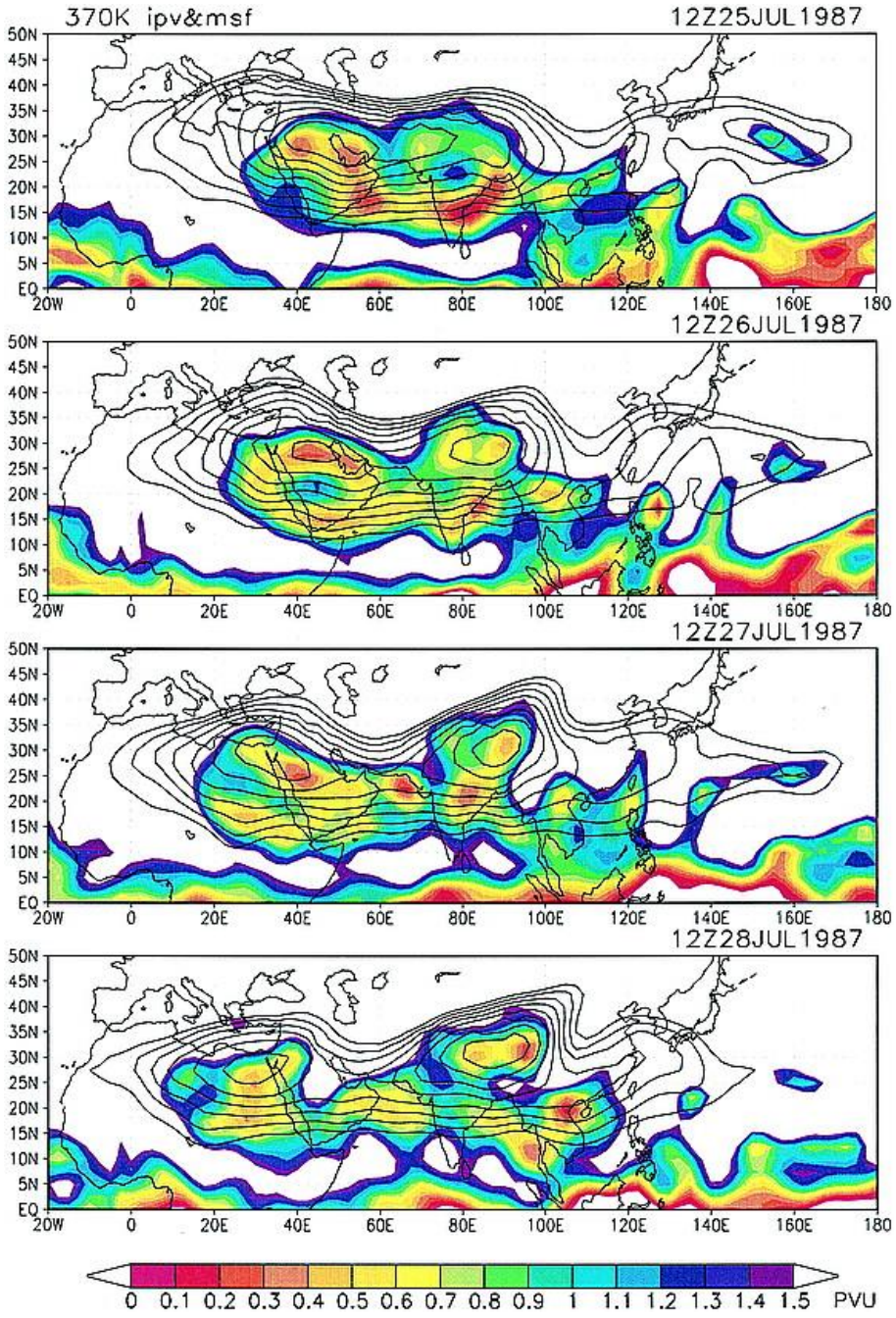

Figure 5.41: Time sequence of potential vorticity (shading) and Montgomery streamfunction (solid black contours) on the 370 K potential temperature surface at 24-hr intervals from July 25 to July 28, 1987.

If (5.56) is violated, a thermally direct circulation must result in any case. The second term in (5.56) is essentially a Laplacian operator, so if the negative curvature of the RCE boundary layer moist entropy distribution is sufficiently strong, a circulation must result. As with the Hadley circulation, a component of flow along isopleths of s_b must develop along with the component up the gradient of s_b to satisfy Ekman balance. In general, this will result in weak cyclone flow at low levels and, of course, a strong anticyclone aloft.

One consequence of the direct circulation itself is that is does modify the distribution of boundary layer entropy through advection, and if the surface energy budget is not balanced (as, for example, when there is appreciable seasonality) the wind itself modifies the surface fluxes through shear-driven turbulence, as represented by aerodynamic flux formulas.

In some cases, advection of low-entropy may shut off deep convection entirely and radically change the nature of the monsoon.

A nice illustration of this is provided by idealized simulations carried out by Privé and Plumb (2007b). They used a general circulation model with prescribed, zonally symmetric sea surface temperature and a land mass covering longitudes 0^o – 180^o and latitudes north of 16^o. Water availability over land was represented by a simple bucket scheme. They first performed a simulation in which the ocean temperature was uniformly warm at all latitudes. This produced a monsoon rainfall distribution (Figure 5.42) not unlike the summer rainfall of our zonally symmetric model (figure 5.40), with strong precipitation just inland of the coast and a weak maximum just south of the equator in association with the previously discussing “jump” of the northward flow over the equator. However, when they prescribed a latitudinal sea surface temperature gradient more typical of northern hemisphere summer, the continent became very dry (middle panel of Figure 5.42). Following earlier work of Chou et al. (2001), they showed that the dryness of the continent in this case is owing to the lateral advection of low moist entropy air from cooler ocean regions. The third panel shows the results of an experiment in which thin north-south walls were places along the eastern and western flanks of the continent, preventing intrusion of this low entropy maritime air. This has the effect of increasing precipitation, particularly over the eastern and southern portions of the continent.

Thus advection of moist entropy can have very significant effects on monsoons. Another very interesting case of this is the role that the Himalaya play in the Indian monsoon. Boos and Kuang (2010) used a full-physics general circulation model to explore what would happen to the Indian monsoon if the Tibetan Plateau and Himalaya Mountains were removed (i.e. their elevation set to zero), and it the Plateau was removed leaving the mountain range itself intact. The model used prescribed, time-varying sea surface temperatures over a 5-year period and the June-August fields were taken to represent the monsoon season. Some results are shown in Figure 5.43. Removing just the plateau has little effect on monsoon precipitation, even though the change in surface elevation (unaccompanied, in this experiment, by any other changes in land characteristics) has a large effect on the local RCE thermodynamic profile, while removing the Himalayas greatly reduced monsoon rainfall. The Himalayas are too narrow to have much effect in RCE, but are effective in blocking the flow of low entropy air from the north into the lowlands and ocean waters south of the mountains. When the mountains are removed, the flow of low entropy air essentially quenches the production of entropy by seasonal solar forcing and the monsoon is greatly reduced.

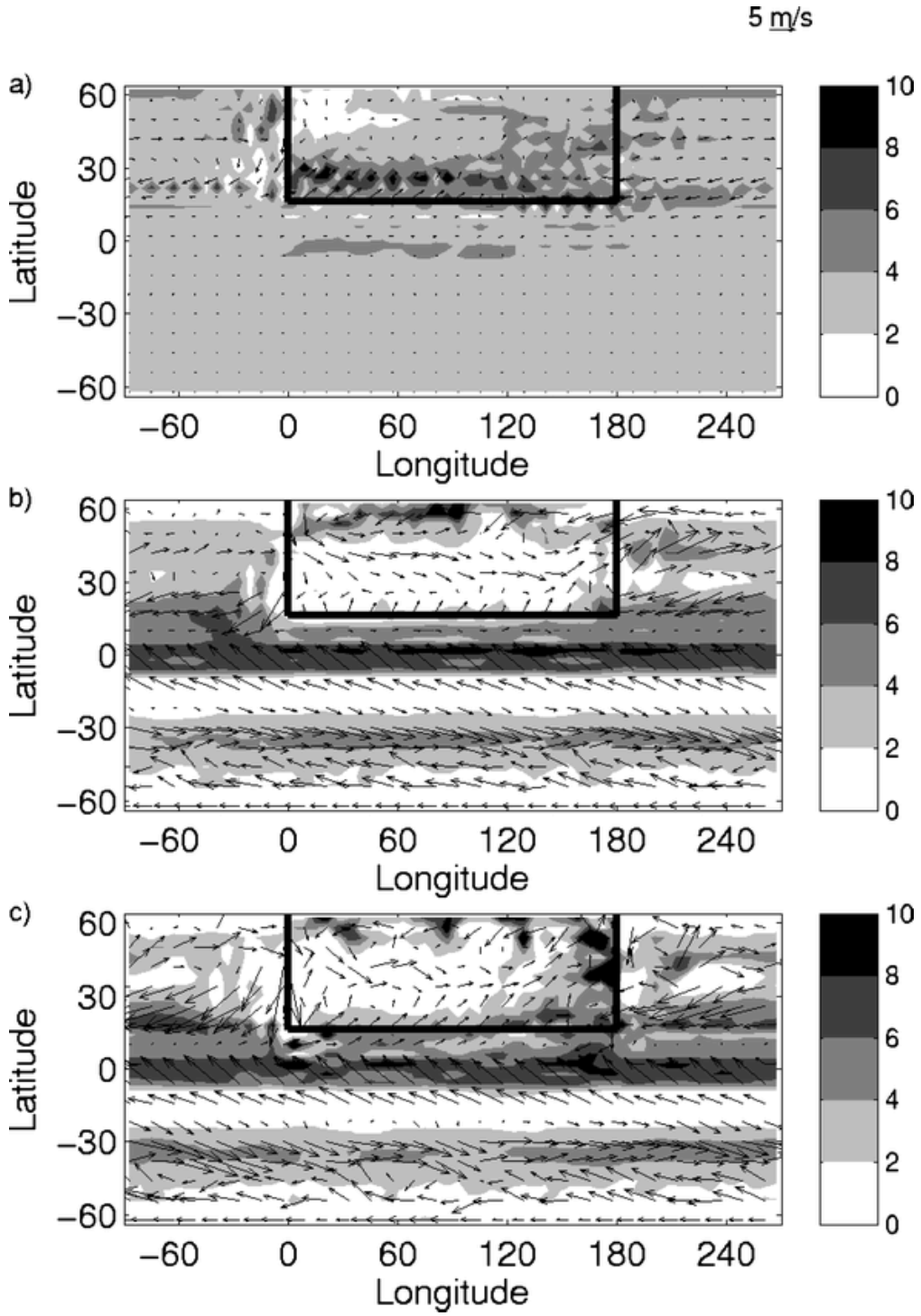

Figure 5.42: 1000-hPa winds (arrows, m s^{-1}) and precipitation (shading,mm day^{-1}) with zonally uniform sea surface temperature (SST) and land within the box depicted by the bold rectangle. (a) Case with uniform warm ocean; (b) case with summer-like SST; (c) case with summer-like SST and thin walls at eastern and western coastlines.

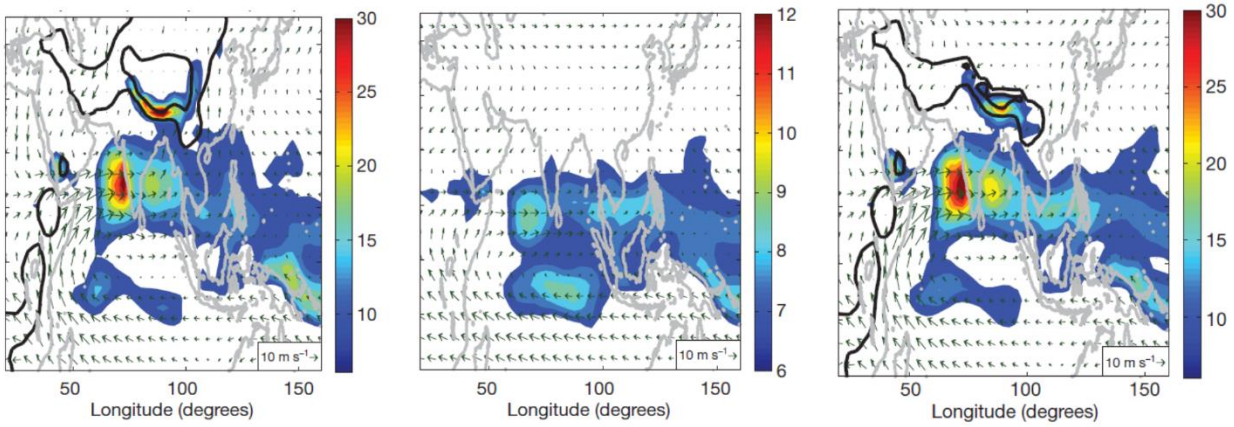

Figure 5.43: Precipitation (shading) and wind (arrows) from general circulation model experiments with prescribed, time-varying sea surface temperatures. Results are averaged over 5 years and over the months of June-August. Thick black contours surround surface pressures lower than 900 hPa and 700 hPa. Left: Control simulation; Middle: Tibetan Plateau and Himalayas removed; Right: Himalayas retained but Plateau removed.

5.3.3 Intraseasonal variability of the monsoon

The seasonal march of solar radiation might be expected, at first glance, to produce a comparably steady evolution of wind and rain accompanying the monsoon. But actual records of monsoon precipitation show very interesting, higher frequency modulation. Figure 5.44 displays rainfall over western India (13^{o}-21^{o} N, 71^{o}-78^{o} E) each day from May 1st through September 30th of 2011. The monsoon rains begin very abruptly around June 1st and are interrupted by breaks lasting 10-20 days. These “active-break” cycles are characteristic of monsoon precipitation and are also strongly correlated with monsoon circulation.

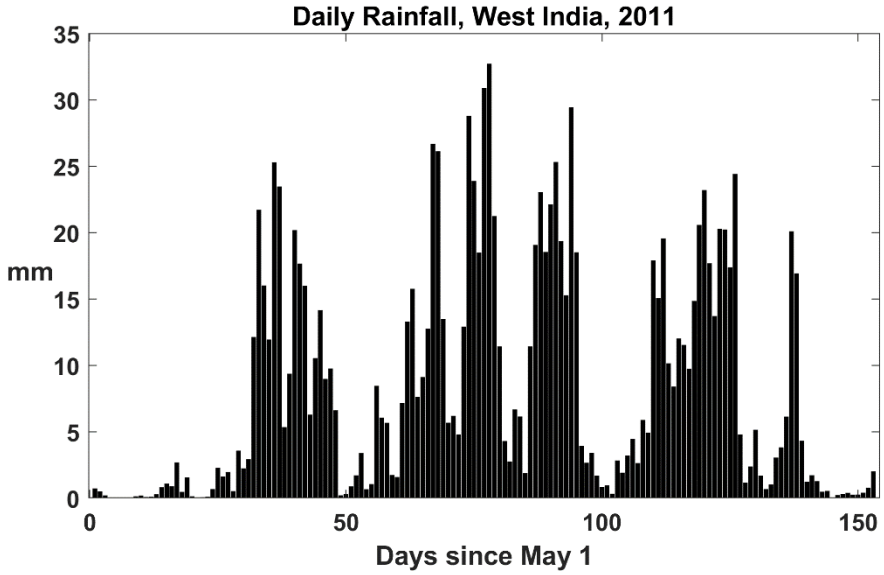

Figure 5.44: Daily rainfall (mm) over western India (13^{o}-21^{o} N, 71^{o}-78^{o} E) from May 1st through September 30th, 2011. Made using NASA’s IMERG data based on a constellation of satellites.

Figure 5.45 shows a smoothed version of the west India rainfall record together with a scaled record of the kinetic energy of the Somali Jet as measured by the square of the meridional wind at 925 hPa[3]. The correlation between the two records is highly statistically significant; this correlation has been recognized since the earliest quantitative analyses of the Indian monsoon (Findlater, 1969).

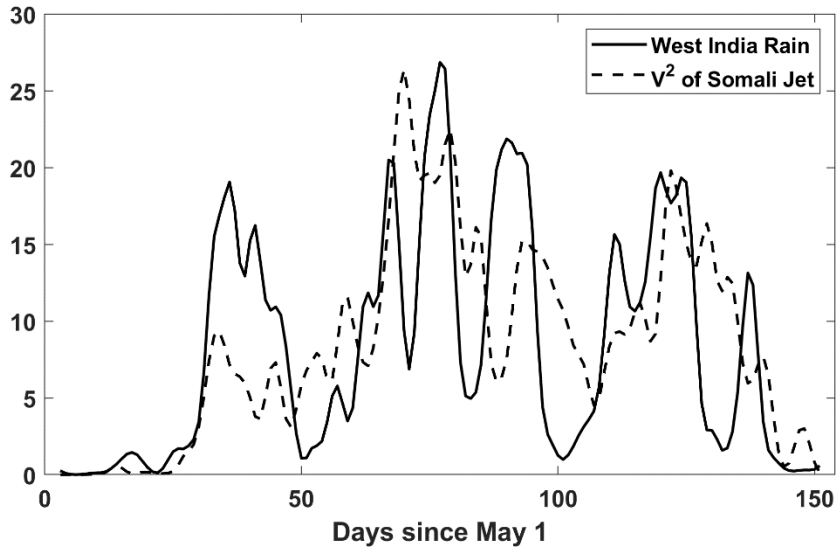

Figure 5.45: Daily precipitation (mm) as in Figure 5.44 (solid) and a measure[3] of the kinetic energy of the Somali Jet (dashed) during 2011. Both quantities have been smoothed with a 1-3-4-3-1 filter.

What is the source of this variability? Part of it may be owing to the effect of wind-induced surface heat exchange (WISHE; Boos and Emanuel, 2008). As late spring insolation heats up the north Indian Ocean, the light surface winds and associated small turbulent heat fluxes from the ocean are not sufficient to produce a positive boundary layer moist entropy gradient that is supercritical in the sense that angular momentum surfaces intersect the equator. As the critical gradient is approached, westerly surface winds begin to increase, increasing the enthalpy flux from the sea in a positive-feedback loop that rapidly leads to cross-equatorial flow. Boos and Emanuel (2008) also showed that WISHE drives the strongest positive meridional gradients of moist entropy close to the equator, which also drives the system to earlier supercriticality. Depending on the magnitude of the insolation forcing, the system may never achieve supercriticality in the absence of WISHE, as shown in Figure 5.26.

Some aspects of this behavior can be simulated using the zonally symmetric primitive equation model described earlier in this chapter (HadleyPak, available at this book's website). Figure 5.46 shows a time series of precipitation at 20o N from the simulation shown in Figure 5.40 and compares it to a second simulation identical to the first but in which the wind used to calculate the surface fluxes is fixed in time, eliminating the WISHE effect.

[3] Specifically, this function is $MAX\left[\ V-6\ ,0\right]^2$, where V is the daily average meridional wind in m/s, averaged between 7.5º S and 7.5º N, and 42º E and 53º W. Both records have been smoothed with a 1-3-4-3-1 filter.

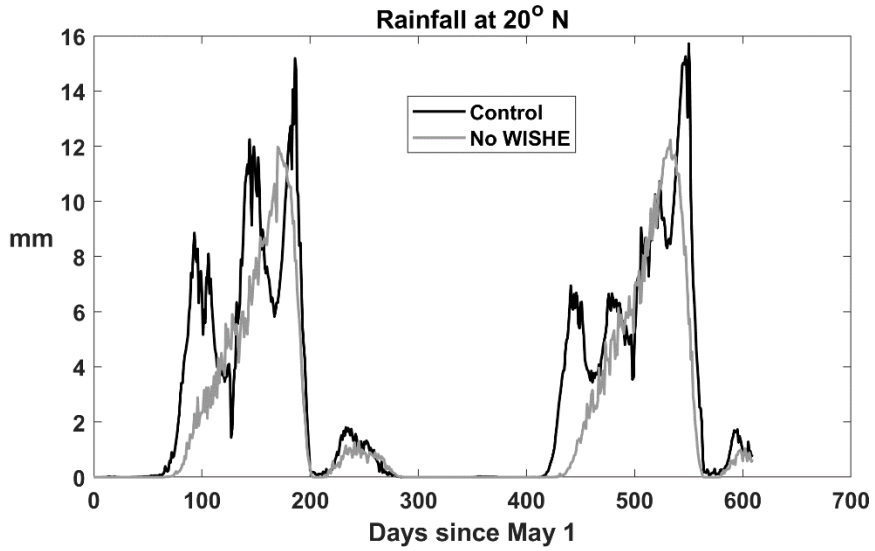

Figure 5.46: Time series of daily precipitation (mm) at 20° N from two simulations of the zonally symmetric primitive equation model used to create Figure 5.40. The control run (black) is that used in Figure 5.40 while a simulation with fixed wind speed in the turbulent surface fluxes is shown in gray. The time series begins on May 1 and extends until January 1 of the second year.

In the no-WISHE simulation, the precipitation at the coast gradually ramps up beginning in late July and reaches a peak at the end of October, collapsing abruptly around 1 November, presumably as the boundary layer moist entropy distribution becomes subcritical. The same behavior can be seen during the second monsoon season in the simulation.

Rainfall begins sooner (in mid-June by the second season) and increases far more rapidly in the control simulation in which WISHE is active. There is far more variability in monsoonal precipitation than in the no-WISHE simulation, but far less than in observations (Figure 5.44), though the frequency of variability is similar to that observed. Note also that the evolution of rainfall in the second monsoon season is, in its details, quite different from the first, suggesting that WISHE may introduce chaotic dynamics into the system, compromising the fundamental predictability limits of the onset and subsequent variability of the rainfall.

Other processes that might contribute to the transient behavior of the monsoon include land-atmosphere interactions, cloud-radiation processes, and three-dimensional effects such as the quasi-periodic shedding of anticyclones from the Tibetan High, as shown in Figure 5.41. Detailed understanding of the sudden onset of monsoon rains and active-break cycles in the monsoon circulation and rainfall awaits further research.

5.3.4 Monsoon depressions

Another very interesting transient affecting the Indian summer monsoon is the monsoon depression. These are cyclonic, warm core depressions that typically form over the Bay of Bengal and move northwestward over northern India, often traveling well inland before dissipating. Figure 5.47 shows sea level pressure and winds just above the surface in a particular monsoon depression.

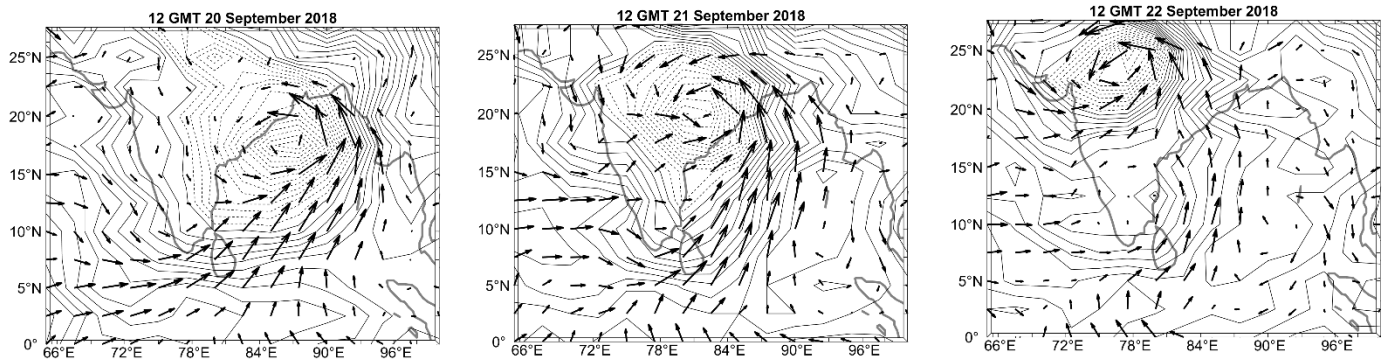

Figure 5.47: Sea level pressure (contours) and near-surface winds (arrows) associated with a monsoon depression moving from the far northern Bay of Bengal on 20 September 2018 (left) to northeastern India on 21 September (center) and continuing northwestward into north central India on September 22 (right). Sea level pressure contours are at 0.5 hPa intervals and are dashed for pressures less than 1007 hPa.

Closed cyclonic circulation developed over the northern Bay of Bengal and Bangladesh in the two days preceding September 20th, 2018 (left panel of Figure 5.47) and on the 20th the well-developed cyclone began moving inland, toward the northwest, only slowly losing intensity. A distinct cyclone is still quite evident on September 22nd (right panel of Figure 5.47).

These disturbances typically amplify while over the Bay of Bengal, reaching maximum intensity at the coastline, and then decaying inland. Although the amplitude of the pressure and wind perturbations are not shown in the figure, they are typically around 3-10 hPa and 10-15 ms^{-1}, respectively[4]. They usually last 4-6 days and 3-6 of them may develop in a typical summer (Hunt et al., 2016). They strongly modulate monsoon rainfall, with the heaviest rain usually found southwest of the depression center.

The average rate of genesis of sub-tropical-cyclone intensity surface low pressure centers is shown in Figure 5.48, based on reanalysis data for the period 1979-2003. Most of the low pressure systems develop in the northern Bay of Bengal and over northeastern India and Bangladesh, with a few developing over northeastern India and the far eastern Arabian Sea. The majority of the systems track northward or northwestward.

A nice overview of the structure of monsoon depressions is provided by Hunt et al. (2016), who composited various quantities with respect to the position of monsoon depression centers. Figure 5.49 shows a composite distribution of TRMM-derived precipitation with respect to the depression center, with each of the contributing precipitation fields rotated about the center with respect to the direction of propagation of the system. The composite maximum rainfall is a few hundred kilometers to the left of and slightly behind the storm with respect to its direction of movement, though lighter rain extends quite far to the right of, and ahead of the system.

The location of the maximum precipitation downshear of the vortex center is consistent with expectations based on quasi-balanced theory (Murthy and Boos, 2020). Basically, this theory

[4] The India Meteorology Department defines a monsoon depression as having peak winds between 8.5 ms^{-1} and 16.5 ms^{-1}. Weaker cyclonic disturbances are simply known as “lows” and stronger ones are classified as tropical cyclones.

can be understood in terms of the necessary balance in either the thermodynamic equation or the vorticity equation in a coordinate system in which the system is stationary.

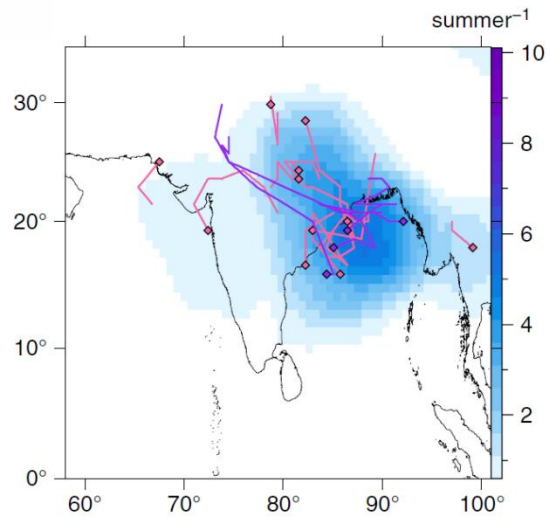

Figure 5.48: Shading shows the number of sub-tropical cyclone low pressures centers generated per summer within 500 km of each point, based in ERA-Interim reanalyses from 1979 to 2003. For the particular summer of 2003, genesis points are shown by filled diamonds while the lines show the tracks of monsoon lows (pink) and monsoon depressions (purple).

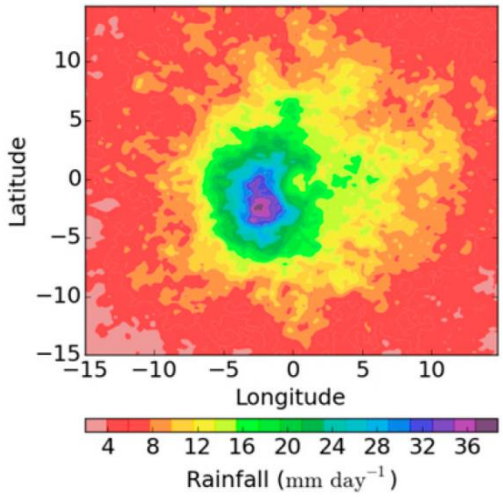

Figure 5.49: Composite precipitation (mm day^{-1}) from TRMM for 34 depressions during 1998–2013. The composite is performed with respect to the center, located arbitrarily at a latitude and longitude of 0, and rotated so that the direction of propagation is always toward the north in this diagram.

From the vorticity perspective, the advection of the positive vorticity of the system by the background flow must be balanced by the stretching term in the quasi-balanced form of the vorticity equation:

$$f\frac{\partial \omega}{\partial p} \cong \mathbf{V}\bullet\nabla\eta, \tag{5.57}$$

in which f is the Coriolis parameter, ω is the pressure velocity, $\mathbf{V}$ is the horizontal velocity vector, and η is the vertical component of the absolute vorticity. If we approximate $\mathbf{V}$ by the background flow, and η by the approximately circular vorticity anomaly of the disturbance, then in the moving reference frame of the storm, downshear from the vortex center, the right-hand side of (5.57) will be negative at upper levels, where the storm relative flow is downshear, and positive at low levels, where it is upshear. This would be consistent, through (5.57), with ascent at middle levels, downshear of the vortex center, and conversely, descent upshear of the center.

Besides this forcing of vertical velocity through quasi-balanced interaction with the background hear, the Ekman flow in the boundary layer will be convergent where the flow is cyclonic, contributing to the general ascent around the system. Cloud-radiation interactions may also contribute to general ascent.

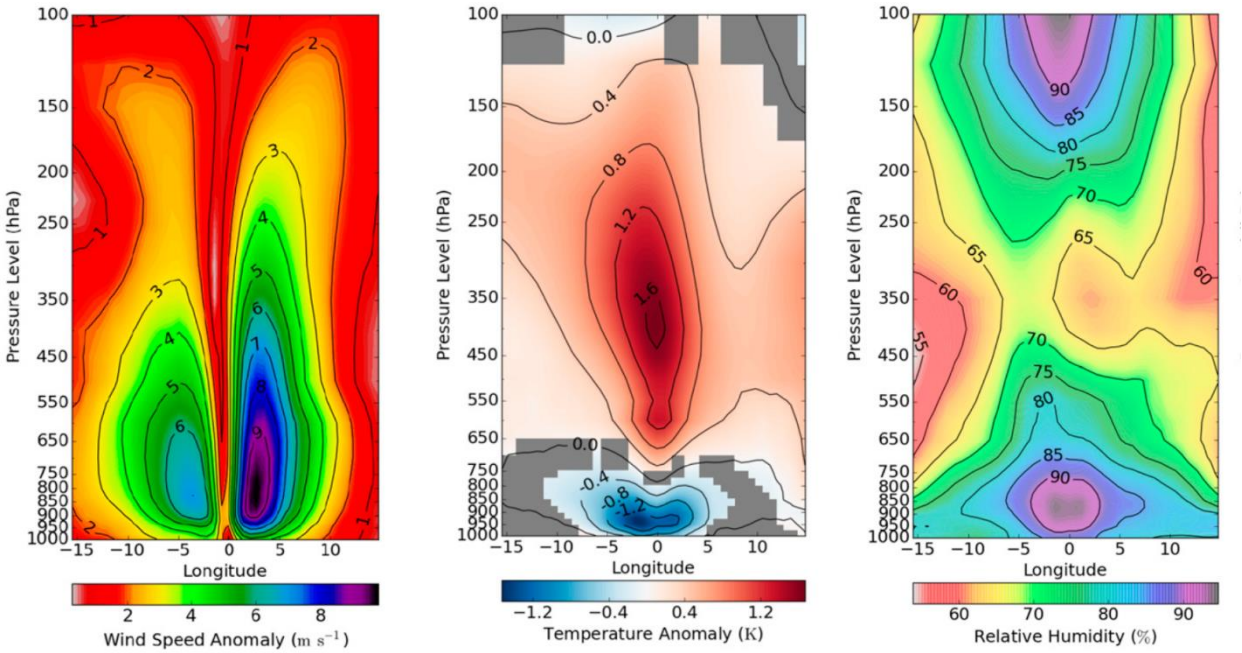

Figure 5.50: Composite cross-sections of tangential wind speed (ms^{-1}, left), temperature anomaly (K, center) and relative humidity (%, right) from ERA-Interim data, 1979-2014. The composite is made by rotating the fields into a reference frame having a common center and with the depression moving into the page. Shading grayed-out where anomaly does not significantly differ from the background at the 95% level.

Composite vertical cross-sections through monsoon depressions are shown in Figure 5.50. The cyclonic wind slopes outward with height, with a broad maximum between 950 and 650 hPa. The vortex is warm core through the whole troposphere above 700 hPa, but cold core in the lower troposphere. The temperature is depressed in the core below the 800 hPa level, but given the positive humidity anomaly that more or less coincides with the warm core, the virtual temperature depression is less. (A rough calculation gives a virtual temperature depression that is about half the temperature depression.) The whole core of the cyclone is anomalously humid, especially in the lowermost and upper most troposphere, and note that the mid-level anomaly is displaced to the left of center relative to the direction of motion, probably reflecting the upward motion inferred to exist on the downshear side of the vortex. (A vertical cross-section of vertical

motion, not shown here, also exhibits enhanced upward motion on the left side of the vortex with respect to its direction of movement.)

The dynamics of monsoon depression remain a subject of vigorous research. Although the structure and distribution of precipitation around monsoon depressions resembles that of nascent tropical cyclones (se Chapter 9), unlike the latter, monsoon depressions develop under conditions of moderate vertical wind shear and sometimes develop over land. Comparing climatological low-level flow (Figure 5.3) and upper tropospheric flow inferred geostrophically from the 200 hPa height field (Figure 5.36), the vertical shear vector points to the west-southwest over the Bay of Bengal and northern India in summer. This is also consistent, in a convectively adjusted environment, with the a generally northward gradient of boundary layer moist entropy (right-hand panel of Figure 5.37).

We first note that the climatological maximum of low-level moist static energy over the northern Bay of Bengal and northeast India (Figure 5.37). If we can assume that the broad region is convectively adjusted and that the Hide condition is locally violated, we would expect the climatological low-level flow to be cyclonic in this region, and indeed Figure 5.30 shows cyclonic shear and curvature over this region in summer. The high moist entropy and cyclonic low-level flow would be expected to favor deep convection. It is possible that cyclonic disturbances periodically form in this favorable environment from some combination of WISHE and cloud-radiation feedbacks, as is the case with tropical cyclones (Chapter 14), and once closed contours of vorticity develop, the cyclones migrate northwestward owing to some combination of ‘beta drift’ (Chapter 12) and Eady-like propagation along contours of the time-mean surface moist static energy. Indeed, in the example shown in Figure 5.47, cyclonic vorticity built up over the far northern Bay of Bengal and Bangladesh for several days before the disturbance began to migrate northwestward.

Most extant literature on the dynamics of monsoon depressions hypothesize that they result from dynamical instabilities of the sheared monsoonal flow in a moist convecting environment. Diaz and Boos (2021) approached the problem using a convection-permitting model with idealized, initially zonally uniform distributions of wind and moist static energy. The initial zonal wind has both easterly shear and, at low levels, cyclonic horizontal shear. The easterly vertical shear is associated with a northward-directed boundary layer moist entropy gradient (and associated temperature gradient aloft). They showed that this flow is unstable to disturbances that behave very much like observed monsoon depressions, and that the growth of such disturbances increases with both the horizontal shear and the magnitude of the boundary layer moist entropy gradient. The absence of either the moist entropy gradient or the absolute vorticity maximum associated with the background horizontal shear of the zonal wind prevents growth of the depressions. This study omitted feedbacks associated with surface fluxes and radiative interactions. It should be remarked that the basic state satisfies the Charney- Stern necessary conditions for quasi-balanced dynamical instability (Charney and Stern, 1962) in two ways: First, the horizontally sheared flow possess a maximum of absolute vorticity, allowing barotropic instability, and second, flow-relative eastward-propagating Rossby waves north of the base state vorticity maximum can interact with flow-relative westward propagating Eady edge waves on the surface moist entropy gradient; the Doppler shifting of these two kind of waves by the vertically sheared mean flow can potentially phase lock them, leading to unstable growth.

The challenge of understanding monsoon depressions is enhanced by the myriad possible mechanisms involving dynamical instabilities, moist convection, and feedbacks involving surface

fluxes and radiation. While it has been possible to simulate these depressions with both idealized and forecast-oriented models, a clear, widely accepted conceptual picture of their physics remains elusive.

5.4 The Walker Circulation

The “Walker Circulation” is an east-west overturning circulation spanning the troposphere and most of the near-equatorial Pacific region, with ascent and anomalously large rainfall in the far west and descent and dry conditions in the east. It was named, in 1969, by Jacob Bjerknes in honor of Gilbert Walker, a British applied mathematician who in 1904 became director-general of observatories in India where he conducted studies of the interannual variability of the monsoon. Figure 5.51 shows and east-west cross-section of the annual mean circulation along the equatorial Pacific, as well as the annual mean precipitation and distribution of sea surface temperature.

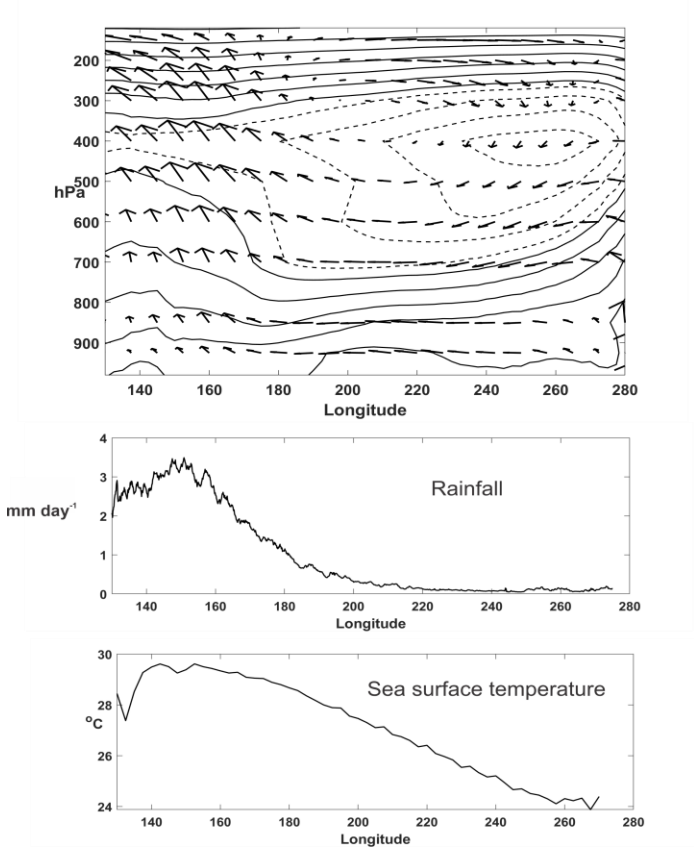

Figure 5.51: Top: Mean circulation (arrows) in the longitude-pressure plane, averaged from 7.5°S to 7.5°N and over each year from 1979-2019, using NCAR/NCEP reanalysis data. The contours show relative humidity (%) in increments of 7.5%, with values below 50% in dashed. Middle: Annual mean precipitation along the equator, from NASA’s IMERG data, 2002-2019. Bottom: Annual mean sea surface temperature on the equator, from NCAR/NCEP reanalyses, 1979-2019.

A key feature of the equatorial Pacific is the strong east-west sea surface temperature gradient… a change of about 5^{o}C across the basin. One finds somewhat concentrated, strong ascent in the western Pacific, and weaker descent east of about 140^{o}E. The heaviest rainfall is west of the dateline, and although both rainfall and sea surface temperature decrease eastward, one is not a simple function of the other.

The Walker circulation is properly understood as a coupled air-sea phenomenon. It would not exist on an aquaplanet (and indeed simulations with coupled global models run in aquaplanet configurations show no analogs) but owes its existence to the presence of continental boundaries at both ends of the basin. The basic physics can begin to be understood with the aid of Figure 5.52. Easterly winds drive ocean waters westward near the equator and also, through Ekman transport, drive upwelling of cold water. in the near-equatorial ocean, the wind stress is balanced by ocean pressure gradients related up an upward, eastward slope of the thermocline. Coastal upwelling off South America and Ekman-induced upwelling maintain cold surface temperatures in the east and a westward-directed surface temperature gradient. The resulting westward gradient in surface turbulent enthalpy fluxes to the atmosphere drives upward motion over the western equatorial Pacific, compensated in part by descent, balanced by radiative cooling, in the east.

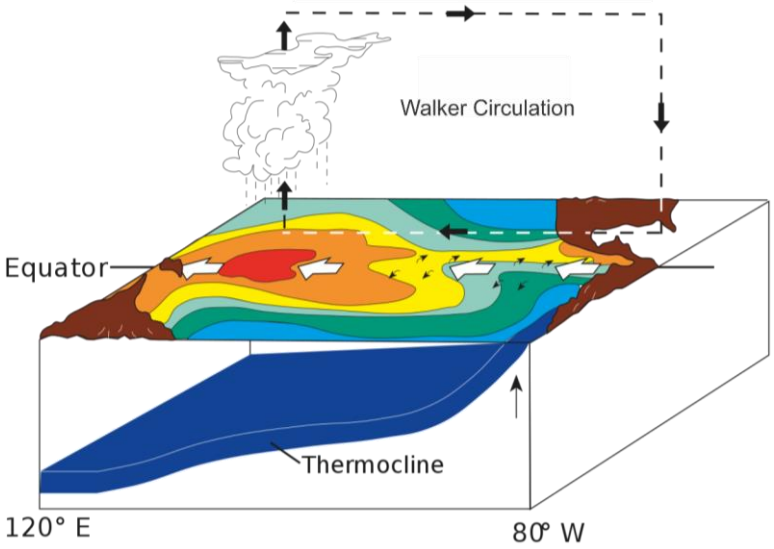

Figure 5.52: Schematic of the Walker circulation in the equatorial Pacific. Shading indicates sea surface temperature. Easterly winds near the equator drive warm water westward, with the surface wind stressed balanced by ocean pressure gradients associated with the upward eastward slope of the thermocline. The large surface heat fluxes on the western side of the basin drive upward motion, with descent in the east balanced by radiative cooling. Small black arrows represent divergence of the upper ocean flow as an Ekman response to westward directed surface wind stress.

Ocean transects along the equator (Figure 5.53) clearly show the warmer water in the west and the upward and eastward sloping thermocline of concentrated temperature gradients. Also note that the surface temperature is approximately a function of the thermocline depth. We can crudely approximate this distribution by dividing it into two fluid layers: An inert lower layer of water superimposed by a slightly less dense layer. The hydrostatic approximation allows us to treat these layers using the shallow water equation. For the upper layer, the zonal equation of motion on the equator itself is

$$\frac{du}{dt} = -g' \frac{\partial h}{\partial x} + \frac{\tau_x}{\rho h}, \tag{5.58}$$

where u is the zonal velocity, h is the depth of the upper layer, and τ_x is the zonal wind stress. Here g' is the reduced gravity:

$$g' \equiv g \frac{\Delta \rho}{\rho}, \tag{5.59}$$

where $\Delta \rho$ is the (slight) difference between the densities of the lower and upper layers. In a steady state, if we ignore the advection of zonal velocity, there is a direct relationship between the wind stress and the slope of the thermocline:

$$\frac{1}{2} g' \frac{\partial h^2}{\partial x} = \frac{\tau_x}{\rho}. \tag{5.60}$$

With surface easterlies producing a negative zonal wind stress, the thermocline shallows toward the east.

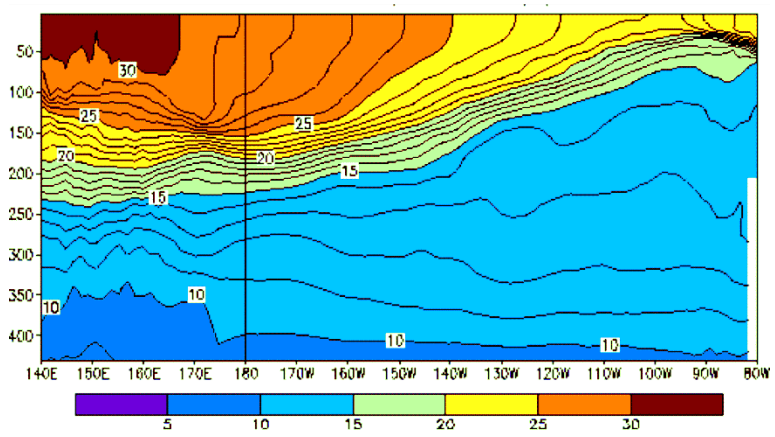

Figure 5.53: Cross-section of ocean temperature (°C) along the equator in December, 2001. Depth (m) shown at left.

5.4.1: Simple model of the coupled Walker Circulation

A first-order description of the coupled Walker circulation can be developed by coupling driving the simple relations for vertical motion and convection in the tropical atmosphere, developed in Chapter 3 with ocean surface fluxes dependent on surface wind speed and ocean temperature as determined from the ocean dynamics. Here we will just empirically relate sea surface

temperature to perturbations in the upper layer depth of the ocean using analyses such as shown in Figure 5.53, and the calculate the ocean depth perturbation from 5.60.

First we are going to assume that there is a convectively coupled region in the west, and a decoupled boundary layer in the east. We will look for steady-state solutions, and begin by re-writing the budget equation for vertically integrated moist static energy (3.64) for the steady case, and ignoring horizontal advection:

$$Gw_b = -\left\langle \alpha \dot{Q}_{cool} \right\rangle + \frac{g}{p_s - p_t} F_h, \tag{5.61}$$

where G is the gross moist stability, $\left\langle \alpha \dot{Q}_{cool} \right\rangle$ is the mass-weighted vertical average of the radiative cooling per unit mass, p_s and p_t are the surface and tropopause pressures, and F_h is the surface enthalpy flux, which we here represent using the aerodynamic flux formula for neutral stability:

$$F_h = \rho C_k |\mathbf{V}| \left(h_0^* - h^* \right), \tag{5.62}$$

where ρ is the surface air density, C_k is the nondimensional surface enthalpy flux coefficient, $|\mathbf{V}|$ is the surface wind speed, h_0^* is the saturation moist static energy of the sea surface, and h^* is the saturation moist static energy of the free troposphere, assumed to be constant vertically (moist adiabatic assumption) and horizontally (WTG). (We assume, according to convective neutrality, that the boundary layer moist static energy equals h^*). We define a scale height $H \equiv \left(p_s - p_t \right) / \rho g$, and for notational convenience, denote $\left\langle \alpha \dot{Q}_{cool} \right\rangle$ as just $\dot{Q}$. Then using these and (5.62) we can re-write (5.61) as

$$Gw_b = -\dot{Q} + H^{-1} C_k |\mathbf{V}| \left(h_0^* - h^* \right). \tag{5.63}$$

Next, to make the problem analytically tractable, we linearize the last term in (5.63) around a basic state that is everywhere in RCE (for which $w_b = 0$) and in which there is a background easterly wind of magnitude U_0:

$$Gw_b' = H^{-1} C_k \left[-u' \left(\overline{h_0^*} - h^* \right) + U_0 h_0^{*\prime} \right], \tag{5.64}$$

where the primes denote perturbations from the base state, and the overbar represents a base state value. We have assumed that $\dot{Q}$ is constant (and so ignore cloud and water vapor feedbacks in radiation) and also ignore the nonlinear correlation between perturbation ocean temperature and perturbation wind. We note that in the RCE state

$$C_k U_0 \left(\overline{h_0^*} - h^* \right) = \dot{Q} H$$

and for notational convenience use this in (5.64):

$$Gw_b' = \left[-u' \frac{\dot{Q}}{U_0} + H^{-1} C_k U_0 h_0^{*\prime} \right]. \tag{5.65}$$

This expression indicates that upward motion can arise from negative perturbation surface winds – which enhance the background easterlies and thus increase the surface enthalpy flux – or from positive ocean temperature perturbations, which likewise increase the surface flux.

Next we relate perturbations in ocean surface temperature T_s' to perturbations in ocean mixed layer depth by simply assuming a linear dependence, based on Figure 5.53:

$$T_s' = \left(\frac{\partial T_s}{\partial d} \right) d', \tag{5.66}$$

where d' is the perturbation mixed layer depth and we estimate the coefficient $\left(\frac{\partial T_s}{\partial d} \right)$ empirically. From the definition of moist static energy, and using the Clausius-Clapeyron equation, we derive

$$h_0^{*\prime} = \left(c_p + \frac{L_v^2 q_0^*}{R_v T_s^2} \right) T_s' = \left(c_p + \frac{L_v^2 q_0^*}{R_v T_s^2} \right) \left(\frac{\partial T_s}{\partial d} \right) d', \tag{5.67}$$

where we have made use of (5.66). Using (5.67), we can express vertical motion as a function of perturbations to the surface zonal wind and to the ocean mixed layer depth.

To close the system, we approximate the two-dimensional mass continuity equation along the equator as

$$\frac{\partial u'}{\partial x} = -2 \frac{w_b'}{H}, \tag{5.68}$$

and we linearize the ocean force balance equation (5.60) as

$$g' D \frac{\partial d'}{\partial x} = \frac{\tau_x}{\rho} = 2 C_D U_0 u', \tag{5.69}$$

where D is the mean mixed layer depth and C_D is the drag coefficient. The right side of (5.69) results from linearizing the aerodynamic drag formula about the mean easterly wind. Negative perturbations of the surface zonal wind (enhanced easterlies) give rise to shoaling mixed layer depth toward the east.

Equation (6.54) is valid in the deep convectively coupled region in the west, while (5.68) and (5.69) are valid everywhere. We first note that there are as many as three possible solutions. First the RCE solution, for which all the perturbation variables vanish, is a stationary state of the system. Without a time-dependent ocean, and possibly atmosphere, it is not clear whether this RCE state is stable. As we will see, for some combinations of parameters, this is the only viable solution. Second, we may have state in which there is deep convection everywhere, but stronger in the west and with a Walker-like circulation. Finally, as we envisioned in setting up

this simple model, the circulation may be strong enough to shut down deep convection in the eastern portion of the basin. We will begin by searching for this third solution.

In the eastern portion of the basin, where we assume a decoupled atmospheric boundary layer and no deep convection, there must be a balance between subsidence warming and radiative cooling. This is expressed by (3.66), which in the current notation can be written

$$w_b' = -\frac{\dot{Q}}{\mathbf{S}}, \tag{5.70}$$

where recall that $\mathbf{S}$ is the base state dry static stability. We can then use mass continuity (5.68) to derive the surface zonal wind. Integrating (5.68) using (5.70) and taking $u' = 0$ at $x = L$, where L is the value of x at the eastern boundary of the basin, we get

$$u' = -2\frac{\dot{Q}}{\mathbf{S}}\ L - x\ . \tag{5.71}$$

Then we can solve (5.69) for the perturbation ocean mixed layer depth, though in so doing we will acquire an integration constant. We will return to this later.

Before proceeding, we can simplify the notation a great deal by nondimensionalizing the dependent variables and the x coordinate. We choose the following normalizations:

$$\begin{aligned} x &\to ax \\ u' &\to U_0 u \\ w_b' &\to \frac{HU_0}{a} w \\ d' &\to \frac{C_D U_0^2 a}{g' D} d \end{aligned} \tag{5.72}$$

in which a is the radius of the Earth. With the substitutions, the equations for conservation of mass and ocean dynamic balance (5.68 and 5.69) can be written simply

$$\frac{\partial u}{\partial x} = -2w, \tag{5.73}$$

and

$$\frac{\partial d}{\partial x} = u. \tag{5.74}$$

In the convective region, the energy balance equation (5.65) (with the additional relations (5.66) and (5.67)) can be written

$$w = -\chi u + \Gamma d, \tag{5.75}$$

where the nondimensional constant parameters are given by

$$\chi \equiv \frac{a\dot{Q}}{GHU_0} \tag{5.76}$$

and

$$\Gamma \equiv \frac{2C_k C_D a^2 U_0^2 \left(c_p + \frac{L_v^2 q_0^*}{R_v T_s^2} \right) \left(\frac{\partial T_s}{\partial d} \right)}{g' G H^2 D}. \tag{5.77}$$

While 5.75 is valid in the deep convecting regime, in the decoupled regime the nondimensional equivalent of (5.70) is

$$w = -w_d \equiv \frac{-\dot{Q}a}{U_0 H \mathbf{S}}, \tag{5.78}$$

where we have introduced w_d for notational convenience.

First, in the deep convecting regime, we can find both the convective updraft mass flux and the difference between the boundary layer and free tropospheric moist static energy though the WTG relations (3.59) and (3.60). Eliminating the moist static energy difference between these two relations, and normalizing the convective updraft mass flux the same was we normalized w_b in (5.72), we have simply

$$M = \frac{w + w_d}{\epsilon_p}, \tag{5.79}$$

where recall that ϵ_p is the precipitation efficiency. For the deep convective solution to be viable, M must be non-negative. Given M or w we can derive the moist static energy deficit through either (3.59) or (3.60).

Thus our relatively simple system consists of (5.73) and (5.74), and either (5.75) if there is deep convection, or (5.78) if there is not.

Let's first look for solutions in the deep convecting regime. If we eliminate w and d in (5.73)-(5.75), the result is a second order equation for u:

$$\frac{1}{2}\frac{\partial^2 u}{\partial x^2} - \chi \frac{\partial u}{\partial x} + \Gamma u = 0. \tag{5.80}$$

The solution to this that satisfies the imposed boundary condition $u = 0$ at $x = 0$ is

$$u = -Ae^{\chi x} \sin\ cx\ , \tag{5.81}$$

where

$$c \equiv \sqrt{2\Gamma - \chi^2} \tag{5.82}$$

and A is an integration constant. Note that the argument of the square root in (5.82) may be negative for some values of the dimensional parameters, in which case we flip the sign of the argument and replace the sine function in (5.81) by a hyperbolic sine.

The corresponding solutions for w and d (when c is a real number) are

$$w = \frac{1}{2} A e^{\chi x} \left[\chi \sin\ cx\ + c \cos\ cx\ \right], \tag{5.83}$$

and using (5.75)

$$d = \frac{1}{2\Gamma} A e^{\chi x} \left[c \cos\ cx\ - \chi \sin\ cx\ \right]. \tag{5.84}$$

An interesting situation arises if c is large enough that $cL > \pi,$ where L is the nondimensional basin length. In that case, according to (5.81), u returns to zero somewhere west of the eastern basin boundary, and the deep convective regime may be viable everywhere. In that case, there is no way to determine the integration constant A in (5.81), except that it is bounded above by two separate conditions: First, the convective updraft mass flux M as given by (5.79) must never become negative, else the system becomes convectively decoupled in places, and second, we must insist that $u < 1$ everywhere, else the total zonal flow (background plus perturbation) would change sign, violating our linearization of the absolute wind speed in the aerodynamic flux formulae. Even if take a value of A small enough to prevent these violations, there is no guarantee that the solution is stable. We will return to this issue later in the chapter.

Now we turn to the case where there is assumed to be a deep convective regime in the west and an uncoupled regime in the east. In the second case, $w = -w_d$ and integration of the mass continuity equation, subject to $u = 0$ on $x = L$ yields the nondimensional equivalent of (5.71):

$$u = -2 w_d\ \ L - x \tag{5.85}$$

Using this, we can integrate (5.74) to find the perturbation mixed layer depth:

$$d = d_0 - w_d x\ \ 2L - x\ , \tag{5.86}$$

where d_0 is an integration constant.

We next need to match the solutions in the deep convecting and uncoupled regimes. We note that we have two integration constants, A and d_0, and also we need to determine the position, in $x,$ of the transition between the two regimes. Altogether, we require three additional stipulations to close the problem. Two of them are straightforward: mass continuity demands that we match the zonal velocity perturbations u at the regime transition, nor can we entertain an infinite acceleration in the ocean that would result from a discontinuity of d, so we must match the perturbation mixed layer depths across the transition. As a third condition, we require the conservation of overall mass of the ocean mixed layer…fluid can rearrange itself in x but the overall mass of the mixed layer should be conserved, so that

$$\int_0^L d \; dx \; = 0 \tag{5.87}$$

Figure 5.54 shows a solution of this system for a particular choice of χ, Γ, w_d and L. Deep convection is confined to roughly the western quarter of the basin, and the thermocline is deepest at the western boundary. The convectively decoupled region spans most of the domain, with easterly winds maximizing at the transition.

The dependence of the transition longitude on Γ with the other nondimensional parameters fixed at the values used in Figure 5.54 is shown in Figure 5.55. No viable solution exists for Γ less than about 40% of the control value used in Figure 5.54. From the definition of Γ given by (5.77), this implies that there will be no Walker circulation if, for example, the exchange coefficients are too small or the sensitivity of ocean surface temperature to the thermocline depth is too small; in that case the RCE state is the only viable steady solution. In our linearization, we assumed a background wind speed in the aerodynamic flux formulae for the surface drag and enthalpy flux. Had we kept the fully nonlinear wind speed in these flux formulae, we likely would have found two solutions: a resting state (for which $\Gamma = 0$ and χ is very large) and a Walker state, in which Γ and χ assume moderate values.

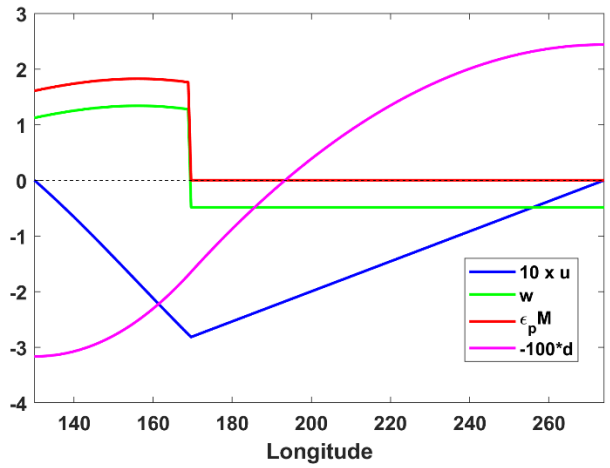

Figure 5:54: Solution of the simple Walker model for χ=2.4 , Γ=35, w_d=0.5, and L=0.4. The blue curve shows zonal velocity perturbation (multiplied by 10), the green curve shows large-scale vertical velocity, the red curve shows the product of the precipitation efficiency and the convective updraft mass flux, and the magenta curve shows the ocean mixed layer depth perturbation multiplied by 100. The mixed layer depth has been flipped so that negative values are positive perturbations to the depth. All graphed quantities are nondimensional. The western boundary is at 130° and the eastern boundary at 274°.

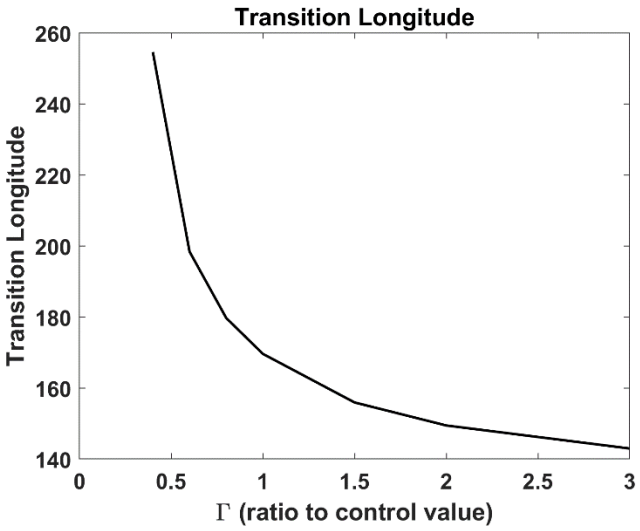

Figure 5.55: Transition longitude as a function of the ratio of Γ *to its control value as used in Figure 5.54. No solutions exist for* $\Gamma / \Gamma_c \lessapprox 0.4$*, where* $\Gamma_c = 2.4$*. The western boundary is at 130° and the eastern boundary at 274°.*

The reader can explore the parameter space of this simple model more thoroughly using the MATLAB script Walker.m available at the course website.

This simple model does not include potentially important feedbacks involving radiation. Qualitatively, we might expect the presence of high clouds and high column water vapor in the west to provide additional column heating there, while low clouds and a dry troposphere would lead to greater column cooling in the east; thus the radiative feedbacks might well enhance the Walker Circulation.

One final point here: We might ask whether we could have found solutions for a mean state with westerly winds. The answer is almost certainly no, because westerlies near the equator would drive an Ekman convergence there, making the ocean mixed layer deeper and preventing any upwelling that would cool the surface. There are two asymmetries at work here: Upwelling cools the surface, but downwelling does not warm it, and easterlies cause upwelling but westerlies cause downwelling. This second asymmetry is, of course, related to the direction of rotation of the Earth.

While formulating a simple view of the Walker Circulation is instructive, we have not addressed what happens off the equator or the important question of whether such a solution is stable and what kind of free oscillations are possible. We will address these issues in the next Chapter, as part of our review of ENSO.

References

Anderson, D. L. T., 1976: The low-level jet as a western boundary current. *Mon. Wea. Rev.*, **104,** 907-921, doi:10.1175/1520-0493(1976)104<0907:Tlljaa>2.0.Co;2.

Blanford, H. F., 1884: II. On the connexion of the Himalaya snowfall with dry winds and seasons of drought in India. *Proceedings of the Royal Society of London*, **37,** 3-22, doi:10.1098/rspl.1884.0003.

Boos, W. R., and K. A. Emanuel, 2008: Wind–evaporation feedback and abrupt seasonal transitions of weak, axisymmetric Hadley circulations. *J. Atmos. Sci.*, **65,** 2194-2214, doi:10.1175/2007jas2608.1.

Boos, W. R., and Z. Kuang, 2010: Dominant control of the South Asian monsoon by orographic insulation versus plateau heating. *Nature*, **463,** 218-222, doi:10.1038/nature08707.

Charney, J. G., and M. E. Stern, 1962: On the stability of internal baroclinic jets in a rotating atmosphere. *J. Atmos. Sci.*, **19,** 159-172, doi:10.1175/1520-0469(1962)019<0159:otsoib>2.0.co;2.

Chou, C., J. D. Neelin, and H. Su, 2001: Ocean-atmosphere-land feedbacks in an idealized monsoon. *Quart. J. Roy. Meteor. Soc.*, **127,** 1869-1891, doi:https://doi.org/10.1002/qj.49712757602.

Compo, G. P., J. S. Whitaker, and P. D. Sardeshmukh, 2008: The 20th century reanalysis project. *Third WCRP International Conference on Reanalysis*.

Diaz, M., and W. R. Boos, 2021: Evolution of idealized vortices in monsoon-like shears: Application to monsoon depressions. *J. Atmos. Sci.*, doi:10.1175/jas-d-20-0286.1.

Emanuel, K. A., 1994: *Atmospheric convection.* Oxford Univ. Press, New York, 580 pp.

Findlater, J., 1969: A major low-level air current near the Indian ocean during the northern summer. *Quart. J. Roy. Meteor. Soc.*, **95,** 362-380, doi:https://doi.org/10.1002/qj.49709540409.

Hadley, G., 1735: Concerning the cause of the general trade winds. *Phil. Trans.;*, **29,** 58-62.

Halley, E., 1686: An historical account of the trade winds, and monsoons, observable in the seas between and near the tropicks, with an attempt to assign the phisical cause of the said winds. *Philosophical Transactions of the Royal Society of London. Series A, Containing Papers of a Mathematical or Physical Character*, **16,** 153-168.

Held, I. M., and A. Y. Hou, 1980: Nonlinear axially symmetric circulations in a nearly inviscid atmosphere. *J. Atmos.. Sci.*, **37,** 515-533.

Hide, R., 1969: Dynamics of the atmospheres of the major planets with an appendix on the viscous boundary layer at the rigid bounding surface of an electrically-conducting rotating fluid in the presence of a magnetic field. *Journal of Atmospheric Sciences*, **26,** 841-853, doi:10.1175/1520-0469(1969)026<0841:Dotaot>2.0.Co;2.

Hunt, K. M. R., A. G. Turner, P. M. Inness, D. E. Parker, and R. C. Levine, 2016: On the structure and dynamics of Indian monsoon depressions. *Mon. Wea. Rev.*, **144,** 3391-3416, doi:10.1175/mwr-d-15-0138.1.

Murthy, V. S., and W. R. Boos, 2020: Quasigeostrophic controls on precipitating ascent in monsoon depressions. *J. Atmos. Sci.*, **77,** 1213-1232, doi:10.1175/jas-d-19-0202.1.

Pauluis, O., 2004: Boundary layer dynamics and cross-equatorial Hadley circulation. *J. Atmos. Sci.*, **61,** 1161-1173, doi:10.1175/1520-0469(2004)061<1161:Bldach>2.0.Co;2.

Privé, N. C., and R. A. Plumb, 2007a: Monsoon dynamics with interactive forcing. Part I: Axisymmetric studies. *J. Atmos. Sci.*, **64,** 1417-1430, doi:10.1175/jas3916.1.

——, 2007b: Monsoon dynamics with interactive forcing. Part II: Impact of eddies and asymmetric geometries. *J. Atmos. Sci.*, **64,** 1431-1442, doi:10.1175/jas3917.1.

Rodwell, M. J., and B. J. Hoskins, 2001: Subtropical anticyclones and summer monsoons. *J. Climate*, **14,** 3192-3211, doi:10.1175/1520-0442(2001)014<3192:Saasm>2.0.Co;2.